

Synthesis and Characterization of Titanium Dioxide Nanomaterials for Photocatalytic Hydrogen Production

Von der Naturwissenschaftlichen Fakultät der
Gottfried Wilhelm Leibniz Universität Hannover
zur Erlangung des Grades

Doktor der Naturwissenschaften

Dr. rer. nat.

genehmigte Dissertation

von

M.Sc. Tarek Abdel-Samad Abdel-Rahman Kandiel
geboren am 10.09.1978 in Gharbia, Ägypten

2010

Referent: Prof. Dr. Thomas Scheper

Korreferent: Prof. Dr. Jürgen Caro

Tag der Promotion: 20.07.2010

Erklärung zur Dissertation

Hiermit erkläre ich, dass ich die vorliegende Dissertation **„Synthesis and Characterization of Titanium Dioxide Nanomaterials for Photocatalytic Hydrogen Production“** als Mitarbeiter des Institutes für Technische Chemie der Gottfried Wilhelm Leibniz Universität Hannover selbständig verfasst und alle benutzten Hilfsmittel sowie evtl. zur Hilfeleistung herangezogene Institutionen vollständig angegeben habe.

Die Dissertation wurde nicht schon als Diplom- oder ähnliche Prüfungsarbeit verwendet.

Hannover, 17.05.2010

M.Sc. Tarek Abdel-Samad Abdel-Rahman Kandiel

Acknowledgements

I would like to express my deepest gratitude to Prof. Dr. Detlef Bahnemann for giving me the chance to work under his supervision in such an interesting area, for his valuable guidance, inspiring reviews, and stimulating discussions.

My sincere thanks go to Prof. Dr. Thomas Scheper for very kindly accepting me as a PhD student in the Institute of Technical Chemistry and for agreeing to act as the referee of my thesis.

My sincere thanks also go to Prof. Dr. Jürgen Caro for his very kind agreement to be the co-referee of my PhD thesis.

I thank the Egyptian Ministry of Higher Education for providing me a doctoral scholarship and the Chemistry Department, Faculty of Science, Sohag University, Egypt for granting me a leave of absence.

I owe special thanks to Dr. Ralf Dillert for numerous scientific discussions and his help in this research area.

I thank PD Dr. Armin Feldhoff for TEM measurements and collaboration and Dr. Lars Robben for XRD measurements, Rietveld analysis, and collaboration.

I also kindly thank Mr. Frank Steinbach for introducing me to the SEM measurement technique and Dipl.-Chem. Monir Sharifi for the nitrogen adsorption isotherm measurements.

I would like to express my sincere appreciation to all members of Prof. Bahnemann's group for their assistance in lab related issues and for the very good atmosphere of work. Thanks are also due to the technical support staff of the Institute of Technical Chemistry.

Grateful thanks are due to my friends and my family, too numerous to name individually, who have all contributed to the unique experience that this PhD investigation has been.

Abstract

The photocatalytic molecular hydrogen (H_2) production from aqueous methanol solutions over Pt-loaded commercial (Evonik Aeroxide TiO_2 P25 and Sachtleben Hombikat UV100) and home made (TiO_2 P25HT) titanium dioxide nanomaterials has been studied. The photonic efficiencies were calculated by dividing the H_2 production rate by the photon flux. The effect of the employed light intensity on the photocatalytic H_2 production rate was investigated. The products of the photocatalytic methanol oxidation were quantitatively analyzed employing different test conditions, i.e., different illumination times, pH values, and methanol concentrations. The balance between the amount of evolved H_2 and the amount of methanol photooxidation products has been tested.

Besides Pt, TiO_2 was also modified with Pt-polypyrrole nanocomposites through the in situ simultaneous reduction of Pt(IV) and the oxidative polymerization of pyrrole monomers at ambient temperature. The modified powders were characterized using X-ray photoelectron spectroscopy, dark-field scanning transmission electron microscopy, infrared spectroscopy, and by the determination of the BET surface area by nitrogen adsorption. The photocatalytic H_2 production over these newly modified TiO_2 nanomaterials has been investigated and compared with that of TiO_2 modified with Pt islands prepared via a photochemical deposition method.

TiO_2 rutile nanorods either decorated with anatase nanoparticles or pure have been prepared via a facile single-step hydrothermal method using commercially available aqueous solutions of titanium(IV) bis(ammoniumlactate) dihydroxide at natural pH (~ 8.0) without any additives. The obtained powders have been characterized by X-ray diffraction, field-emission scanning electron microscopy, high-resolution transmission electron microscopy, UV-Vis diffuse reflectance spectroscopy, and by nitrogen adsorption. These newly prepared rutile nanomaterials showed negligibly small photocatalytic H_2 production activity. In contrast, they exhibit high photocatalytic activities towards the decomposition of gaseous acetaldehyde under UV(A) illumination.

In addition to rutile nanomaterials, high quality brookite TiO_2 nanorods have been obtained by the thermal hydrolysis of commercially available aqueous solutions of titanium(IV) bis(ammoniumlactate) dihydroxide in the presence of high concentrations of urea (≥ 6.0 M) as in situ OH^- source. Biphasial anatase/brookite mixtures were obtained at lower urea concentrations. The ratios between anatase and brookite can readily be tailored by the control of the urea concentration. The obtained powders have been characterized by X-ray diffraction, Raman spectroscopy, field-emission scanning electron microscopy, high-

resolution transmission electron microscopy, UV-Vis diffuse reflectance spectroscopy, and by nitrogen adsorption. The photocatalytic activities of pure anatase nanoparticles, of anatase/brookite mixtures, and of pure brookite nanorods have been assessed by H₂ evolution from aqueous methanol solution as well as by the degradation of dichloroacetic acid in aqueous solution and by the decomposition of gaseous acetaldehyde under UV(A) illumination. The results indicate that the photocatalytic H₂ evolution activity of anatase/brookite mixtures and of pure brookite is higher than that of pure anatase nanoparticles despite of the lower surface area of the former. This behavior is explained by the fact that the conduction band edge of brookite phase TiO₂ is shifted more cathodically as compared with that of anatase as experimentally verified under dark and UV-Vis illumination conditions. On the contrary, in case of both the photocatalytic degradation of dichloroacetic acid in aqueous suspensions and the decomposition of gaseous acetaldehyde, anatase/brookite mixtures and pure brookite exhibit lower photocatalytic activity than pure anatase nanoparticles. This behavior correlates well with the BET surface area of the investigated powders.

The rates and the photonic efficiencies of the photocatalytic H₂ evolution from aqueous methanol solutions over the different Pt-loaded TiO₂ nanomaterials have been compared. From this comparison, specific routes for the preparation of photocatalytically highly active TiO₂ nanomaterials are suggested.

Keywords: Photocatalytic H₂ production, Methanol photooxidation, Anatase nanoparticles, Rutile nanorods, Brookite nanorods, Dichloroacetic acid, Acetaldehyde.

Kurzzusammenfassung

Untersucht wurde die photokatalytische Wasserstoffproduktion aus wässrigen Lösungen von Methanol an kommerziell erhältlichen (Evonik Aeroxide TiO₂ P25 und Sachtleben Hombikat UV 100) und selbst-synthetisierten (TiO₂ P25HT) Titandioxid-Nanomaterialien, die mit Pt beladen waren. Die Photoneneffizienzen wurden berechnet als Quotient aus H₂-Bildungsgeschwindigkeit und Photonenfluss. Der Einfluss der Lichtintensität auf die Bildungsgeschwindigkeit von H₂ wurde untersucht. Die Reaktionsprodukte der photokatalytischen Oxidation von Methanol unter verschiedenen Reaktionsbedingungen, wie Bestrahlungszeit, pH der Lösung und Methanolkonzentration, wurden quantitativ bestimmt. Das Verhältnis zwischen der gebildeten Menge an H₂ und den Mengen der Oxidationsprodukte des Methanols wurde ermittelt.

TiO₂ wurde außer mit Pt auch mit Pt-Polypyrrol-Nanokompositen modifiziert, die bei Umgebungstemperatur in situ durch Reduktion von Pt(IV) unter gleichzeitiger oxidativer Polymerisation von Pyrrol erhalten wurden. Die modifizierten TiO₂-Pulver wurden mit röntgeninduzierter Photoelektronenspektroskopie, Dunkelfeld-Raster Transmissions-elektronenmikroskopie, Infrarotspektroskopie und durch Bestimmung der BET-Oberfläche mittels Stickstoffadsorption charakterisiert. Die photokatalytische Wasserstofferzeugung an diesen hier neu synthetisierten TiO₂-Nanomaterialien wurde untersucht und mit jener verglichen, die an einem mit Pt modifizierten TiO₂ beobachtet wurde.

Reine und mit Anatas-Nanopartikeln beladene Rutil-TiO₂ Nanostäbchen wurden ausgehend von kommerziell erhältlichem Titan(IV)-bisammoniumlaktat-dihydroxid bei dem natürlichen pH der Lösung (~ pH 8.0) ohne weitere Zusätze durch eine einstufige Hydrothermalsynthese hergestellt. Die hergestellten Pulver wurden mittels Röntgenbeugung, Rasterelektronenmikroskopie, hochauflösender Transmissionselektronenmikroskopie, diffuser Reflektionspektroskopie im UV- und Vis-Bereich sowie durch Stickstoffadsorption charakterisiert. Diese erstmals synthetisierten Rutil-Nanomaterialien wiesen vernachlässigbar geringe Aktivitäten für die photokatalytische Wasserstofferzeugung auf, zeigten jedoch unter Belichten mit UV(A)-Licht hohe photokatalytische Aktivitäten für die Zersetzung von Acetaldehyd in der Gasphase.

Durch thermische Hydrolyse von Titan(IV)-bisammoniumlaktat-dihydroxid war außer den Rutil-Nanomaterialien auch sehr reines Brookit TiO₂ zugänglich, wenn die Reaktion unter Zusatz hoher Konzentrationen an Harnstoff (≥ 6.0 M) als in situ Hydroxidquelle erfolgte. Bei geringeren Harnstoffkonzentrationen wurden Anatas-Brookit-Mischungen erhalten. Das

Anatas-Brookit-Verhältnis konnte einfach durch Veränderung der Harnstoffkonzentration eingestellt werden. Die synthetisierten Pulver wurden durch Röntgenbeugung, Ramanspektroskopie, Rasterelektronenmikroskopie, hochauflösende Transmissions-elektronenmikroskopie, diffuse Reflektionspektroskopie im UV- und Vis-Bereich und durch Stickstoffadsorption charakterisiert. Die photokatalytischen Aktivitäten reiner Anatas-Nanoteilchen, von Anatas-Brookit-Mischungen und von reinen Brookit-Nanostäbchen wurden durch Untersuchungen zur Wasserstoffbildung aus wässrigen Methanollösungen und durch den oxidativen Abbau von Dichloressigsäure in Wasser sowie von Acetaldehyd in Luft bei Belichten mit UV(A)-Licht bestimmt. Die Ergebnisse zeigen, dass die Aktivitäten von Anatas-Brookit-Mischungen und von reinem Brookit für die photokatalytische Wasserstoffentwicklung trotz geringerer Oberflächen höher sind als die von reinen Anatas-Nanoteilchen. Dieses Verhalten wird damit erklärt, dass die Bandkante des Brookits gegenüber der des Anatas kathodisch verschoben ist, wie durch Untersuchungen im Dunkeln und unter Belichten mit UV-A-Licht experimentell bestätigt wurde. Im Gegensatz dazu zeigten Anatas-Brookit-Mischungen und reines Brookit eine geringere photokatalytische Aktivität für den Abbau von Dichloressigsäure in wässrigen Suspensionen und für die Zersetzung von Acetaldehyd in der Gasphase als die reinen Anatas-Nanoteilchen. Dieses Verhalten korreliert mit der BET-Oberfläche der untersuchten Pulver.

Die Reaktionsgeschwindigkeiten und die Photoneneffizienzen der photokatalytischen Wasserstoffbildung aus wässrigen Methanollösungen an verschiedenen Pt-beladenen TiO₂-Nanomaterialien wurden verglichen. Zielführende Wege für die Herstellung photokatalytisch hoch aktiver TiO₂-Nanomaterialien werden ausgehend von diesen Untersuchungen vorgeschlagen.

Stichworte: Photokatalytische Wasserstofferzeugung, Methanol-Oxidation, Anatas-Nanoteilchen, Rutil-Nanostäbchen, Brookit-Nanostäbchen, Dichloressigsäure, Acetaldehyd.

Contents

1. Introduction	1
1.1. Titanium dioxide (TiO ₂) photocatalysis	1
1.1.1. Historical development.....	1
1.1.2. Theoretical background	3
1.2. Molecular hydrogen (H ₂) Production	5
1.2.1. Photocatalytic H ₂ production from water	6
1.2.2. Photocatalytic H ₂ production from aqueous methanol solution	10
1.3. Titanium dioxide (TiO ₂) nanomaterials.....	13
1.3.1. TiO ₂ crystal phases	13
1.3.2. Hydrothermal synthesis of TiO ₂ nanomaterials.....	15
1.3.2.1. Hydrothermal synthesis as a materials synthesis technology.....	15
1.3.2.2. Examples of hydrothermally synthesized TiO ₂ nanomaterials.....	16
1.3.3. Modification of TiO ₂ nanomaterials.....	22
2. Materials and Experimental Methods.....	25
2.1. Materials	25
2.2. Synthesis of TiO ₂ nanomaterials	26
2.2.1. Synthesis of TiO ₂ anatase nanoparticles	26
2.2.2. Synthesis of TiO ₂ rutile nanorods	26
2.2.3. Synthesis of TiO ₂ anatase nanoparticles, anatase/brookite mixtures, and brookite nanorods	26
2.3. Modification of TiO ₂ nanomaterials.....	28
2.3.1. Modification of TiO ₂ with Pt nanoparticles via a photochemical deposition method	28
2.3.2. Modification of TiO ₂ with Pt-polypyrrole nanocomposites.....	28
2.3.3. Modification of TiO ₂ with Pt nanoparticles using colloidal Pt suspension.....	28
2.4. Characterization of TiO ₂ nanomaterials	29
2.4.1. X-ray diffraction.....	29
2.4.2. Field-emission scanning electron microscopy.....	29
2.4.3. High-resolution transmission electron microscopy.....	29

Contents	viii
2.4.4. Specific surface area measurements	30
2.4.5. Diffuse reflectance spectroscopy	30
2.4.6. Infrared and Raman spectroscopy	30
2.4.7. X-ray photoelectron spectroscopy	30
2.4.8. Flatband potential measurements	31
2.4.9. Quasi Fermi level measurements	31
2.5. Experimental setup for the evaluation of the photocatalytic activities of TiO ₂ nanomaterials	32
2.5.1. Photocatalytic H ₂ production	32
2.5.2. Photocatalytic degradation of dichloroacetic acid	33
2.5.3. Photocatalytic decomposition of acetaldehyde	34
2.6. Analysis of methanol photooxidation products	36
2.7. Ferrioxalate actinometry	37
3. Results	38
3.1. Synthesis, modification, and characterization of TiO ₂ nanomaterials	38
3.1.1. TiO ₂ anatase nanoparticles	38
3.1.2. TiO ₂ -polypyrrole nanocomposites	41
3.1.3. TiO ₂ rutile nanorods	43
3.1.4. TiO ₂ anatase nanoparticles, anatase/brookite mixtures, and brookite nanorods	48
3.2. Evaluation of the photocatalytic activities	53
3.2.1. Liquid phase reactions	53
3.2.1.1. Photocatalytic H ₂ evolution from aqueous methanol solution over:	53
(a) Pt-loaded TiO ₂ P25, TiO ₂ UV100, and TiO ₂ P25HT	53
(b) TiO ₂ P25 modified with Pt-polypyrrole nanocomposites	58
(c) Pt-loaded TiO ₂ anatase nanoparticles, anatase/brookite mixtures, and brookite nanorods	62
3.2.1.2. Photocatalytic degradation of dichloroacetic acid using TiO ₂ anatase nanoparticles, anatase/brookite mixtures, and brookite nanorods	66
3.2.2. Gas phase reactions	68
3.2.2.1. Photocatalytic decomposition of acetaldehyde using TiO ₂ rutile nanorods	68

3.2.2.2. Photocatalytic decomposition of acetaldehyde using TiO ₂ anatase nanoparticles, anatase/brookite mixtures, and brookite nanorods.....	69
4. Discussion.....	71
4.1. Proposed formation route of TiO ₂ nanomaterials.....	71
4.1.1. TiO ₂ anatase nanoparticles	71
4.1.2. TiO ₂ rutile nanorods	75
4.1.3. TiO ₂ anatase nanoparticles, anatase/brookite mixtures, and brookite nanorods	79
4.2. Evaluation of the photocatalytic activities.....	84
4.2.1. Liquid phase reactions	84
4.2.1.1. Photocatalytic H ₂ evolution from aqueous methanol solution over:	84
(a) Pt-loaded TiO ₂ P25, TiO ₂ UV100, and TiO ₂ P25HT.....	84
(b) TiO ₂ modified with Pt-polypyrrole nanocomposites	93
(c) Pt-loaded TiO ₂ anatase nanoparticles, anatase/brookite mixtures, and brookite nanorods	97
4.2.1.2. Comparison of the photocatalytic H ₂ evolution activities of the different investigated photocatalysts	105
4.2.1.3. Photocatalytic degradation of dichloroacetic acid using TiO ₂ anatase nanoparticles, anatase/brookite mixtures, and brookite nanorods.....	109
4.2.2. Gas phase reactions	111
4.2.2.1. Photocatalytic decomposition of acetaldehyde using TiO ₂ rutile nanorods	111
4.2.2.2. Photocatalytic decomposition of acetaldehyde using TiO ₂ anatase nanoparticles, anatase/brookite mixtures, and brookite nanorods.....	113
4.2.2.3. Comparison of the photocatalytic activity of gaseous acetaldehyde decomposition on the different investigated photocatalysts.....	115
5. Summary.....	117
6. References	121
7. Appendix	135
7.1. List of abbreviations and symbols	135
7.2. List of tables	138
7.3. List of figures	139
7.4. Publications	146
7.5. Presentations.....	146

Contents	x
7.5.1. Oral presentations	146
7.5.2. Poster presentations	147
7.6. Curriculum vitae	148

1. Introduction

1.1. Titanium dioxide (TiO₂) photocatalysis

1.1.1. Historical development

TiO₂ powders have been commonly used as pigments starting already in ancient times. They are inexpensive, chemically stable and harmless, and do not absorb any light in the visible region. Therefore, they exhibit a white color. However, the chemical inertness of TiO₂ holds only in the dark. Instead, it is active under UV light irradiation, inducing some chemical reactions. Such activity under sunlight has been known for along time from the flaking of paints and the degradation of fabrics incorporating TiO₂. [1] Scientific studies on such photoactivity of TiO₂ have been reported since the early part of the 20th century. For example, there was a report on the photobleaching of dyes by TiO₂ both *in vacuo* and in oxygen in 1938. [2] It was reported that UV absorption produces active oxygen species on the TiO₂ surface, causing the photobleaching of dyes. It was also known that TiO₂ itself does not change through the photoreaction, although the “photocatalyst” terminology was not used for TiO₂ in the report, but it was called a photosensitizer. In 1964, Kato and Masuo reported on the photocatalytic oxidation of tetralin(1,2,3,4-tetrahydronaphthalene) by a titania suspension. [3] In 1965, McLintock and Nowbray reported on the solid-gas phase photocatalytic oxidation of ethylene and propylene in the presence of adsorbed oxygen on titania. [4] However, it is equivocal when and who started utilizing first such a photochemical power of TiO₂ to induce chemical reactions actively. Photocatalysis over TiO₂ first attracted concentrated scientific research efforts in 1972 following the demonstration by Fujishima and Honda of the photoelectrolysis of water using a TiO₂ electrode under UV irradiation and in the presence of an anodic bias. [5] Numerous studies related to that of Fujishima and Honda have been reported since the 1970s. [6]

In the early 1980s, photocatalytic water splitting has been studied intensively employing powdered anatase TiO₂ suspensions, with Pt deposited on TiO₂ as a cathodic catalyst. Although there were several experiments for the simultaneous production of H₂ and O₂ in the powder systems, either such experiments could not be reproduced or the reaction efficiency was very low. [7-9]

In the middle of the 1980s, research shifted to the oxidation of pollutants using suspensions of TiO₂ in contaminated water, allowing a wide range of air and water purification products. This application has been greatly developed, leading to an extensive body of research that has

been the subject of a number of reviews including those by Mills et al., Hoffmann et al., and Linsebigler et al.[10-12]

In 1995 it was discovered that UV irradiation induces superhydrophilicity in TiO₂ through the formation of additional surface hydroxyl groups.[1] This effect allows water droplets to run freely across a TiO₂ coated surface, and is used in products such as Pilkington Activ™ self-cleaning glass and anti-fogging mirrors for cars.

In 2001 Asahi et al. [13] reported that substitution of nitrogen onto cation sites within anatase TiO₂ introduced new energy states above the valence band thus lowering the effective bandgap and extending the material's photocatalytic response into the visible range. Previously, researchers had attempted to use cation doping or oxygen substoichiometry to introduce mid gap energy states, but these materials suffered thermal instability and increased carrier recombination.

Nowadays, TiO₂ photocatalysis has become a real practical technology, particularly in the field of building materials. Some selected applications of photocatalysis are summarized in Table 1.1.

Table 1.1. Selected applications of photocatalysis.[14, 15]

Property	Category	Application
Self-cleaning	Materials for residential and office buildings	Exterior tiles, kitchen and bathroom components, interior furnishings, plastic surfaces, aluminum siding, building stone and curtains
	Indoor and outdoor lamps and related systems	Translucent paper for indoor lamp covers, coatings on fluorescent lamps and highway tunnel lamp cover glass
	Materials for roads	Tunnel wall, soundproofed wall, traffic signs and reflectors
	Others	Tent material, cloth for hospital garments and uniforms and spray coatings for cars
Air cleaning	Indoor air cleaners	Room air cleaner, photocatalyst-equipped air conditioners and interior air cleaner for factories
	Outdoor air purifiers	Concrete for highways, roadways and footpaths, tunnel walls, soundproof walls and building walls
Water purification	Drinking water	River water, ground water, lakes and water-storage tanks
Antitumor activity	Cancer therapy	Endoscopic-like instruments
Self-sterilizing	Hospital	Tiles to cover the floor and walls of operating rooms, silicone rubber for medical catheters and hospital garments and uniforms
	Others	Public rest rooms, bathrooms, and rat breeding rooms

Recently, growing environmental concern and an increasing energy demand are driving the search for new, sustainable sources of energy. In particular, solar molecular hydrogen (H_2) has attracted much attention because it can be regarded as a renewable and clean-burning energy source. Among the proposed technologies for its production, the photocatalytic conversion of biomass derived compounds is currently being discussed and investigated extensively. Titanium dioxide is believed to be the most promising presently known photocatalyst, because of its superior photoreactivity, its nontoxicity, its long-term stability, and its low price. Thus, in this thesis a simple route for the synthesis of TiO_2 nanomaterials with different morphologies and different phase compositions will be presented. These newly synthesized TiO_2 nanomaterials will be investigated as photocatalysts, particularly, for the photocatalytic H_2 production from aqueous methanol solution and as photocatalysts in general for the degradation of organic compounds in aqueous solution and in gas phase.

1.1.2. Theoretical background

A number of review papers have summarized the current knowledge about the mechanism of photocatalytic reactions both, from a theoretical and an experimental perspectives.[10-12, 14, 16-19] It is commonly accepted that the reaction progresses via a multi-step route starting with photon absorption, exciton formation, charge separation and charge transfer to the electrolyte species at the anodic and the cathodic sites. Other processes that may occur include charge recombination or trapping, reactant adsorption and desorption.

Titanium dioxide as a semiconductor can act as a sensitizer for light-induced redox processes due to its electronic structure, which is characterized by a filled valence band and an almost empty conduction band being an n-type semiconductor. Absorption of a photon with an energy exceeding the bandgap energy leads to the formation of an electron/hole pair (Eq. 1.1). In the absence of suitable scavengers, the stored energy is dissipated within a few nanoseconds by recombination (Eq. 1.2). If a suitable scavenger or surface defect state is available to trap the electron or hole, recombination can be prevented and subsequent redox reactions may occur. The valence band holes are powerful oxidants ($\sim +3.0V$ vs. NHE),[20] while the conduction band electrons are rather good reductants (0.0 to -0.5 V vs. NHE depending on the TiO_2 phases). Most organic photodegradation reactions (electron donor, D) utilize the oxidizing power of the holes either directly through the reaction with the photogenerated holes (Eq. 1.3) or indirectly through the reaction with the so called trapped holes ($\equiv Ti^{IV}OH^{*+}$) or with $\cdot OH$ radicals formed as highly reactive intermediates (Eqs. 1.4, 1.5,

and 1.6); however, to prevent a buildup of charge reducible species (electron acceptor, A) must also be present to react with the electrons (Eq. 1.7).



At the surface of bulk semiconductor electrodes only one species, either the hole or the electron, is available for reactions due to band bending. However, in very small semiconductor particles both species are present on the surface. Therefore, careful consideration of both, the oxidative and the reductive paths is required. Figure 1.1 shows a schematic presentation of the photocatalytic processes.[21, 22] It consists of a superposition of the energy bands of TiO₂ semiconductor (valence band VB, conduction band CB) and the geometrical image of a spherical particle. Absorption of a photon with an energy $h\nu$ greater or equal to the bandgap energy E_g generally leads to the formation of an electron/ hole pair in the semiconductor particle. These charge carriers subsequently either recombine and dissipate the input energy as heat, get trapped in metastable surface states, or react with electron donors and acceptors adsorbed on the surface or present within the electrical double layer.

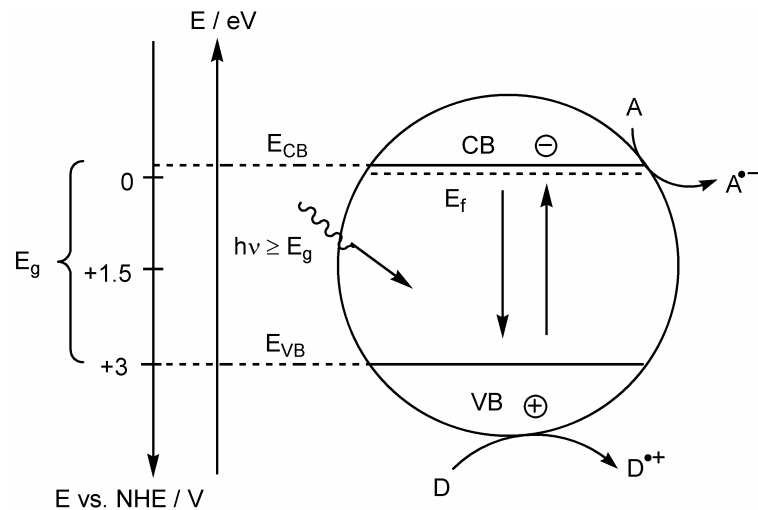


Figure 1.1. Principle mechanism of photocatalysis and superposition of the energy band diagram with the geometrical image of a spherical TiO₂ particle. Note: for simplicity, the indirect oxidation of electron donor (D) by trapped holes ($\equiv \text{Ti}^{\text{IV}}\text{OH}^{\bullet+}$) or by $\bullet\text{OH}$ radicals is represented by the hole oxidation step.

1.2. Molecular hydrogen (H₂) Production

Hydrogen is the most common element on earth, but it does not occur to a significant extent in its elemental form. It is mostly present in water, in biomass and in hydrocarbons. Hydrogen gas is currently produced from a variety of primary sources, such as natural gas, naphtha, heavy oil, methanol, biomass, wastes, coal, solar energy, wind energy, hydropower, and nuclear energy.[23] It is a clean energy fuel because the chemical energy stored in the H–H bond is released when it combines with oxygen, yielding only water as a reaction product. Accordingly, a future energy infrastructure based on H₂ is regarded as an ideal long-term solution to energy-related environmental problems. There is no doubt that hydrogen has the potential to provide a clean and affordable energy supply that can minimize our dependence on oil and therefore enhance the global economy and reduce environmental pollution.

It is generally understood that the renewable energy-based processes of H₂ production (solar photochemical and photobiological water decomposition, electrolysis of water coupled with photovoltaic cells or wind turbines, etc.) are unlikely to involve significant reductions in hydrogen gas costs over the next ten to twenty years. Industry generates some 48000 million kilograms of hydrogen globally each year from fossil fuel.[24] Almost half of this hydrogen is used for making ammonia, while refineries use the second largest volume of hydrogen for chemical processes such as removing sulfur from gasoline and converting heavy hydrocarbons into gasoline and diesel fuel. Food producers add a small percentage of hydrogen gas to some edible oils through a catalytic hydrogenation process. The demand for H₂ is expected to grow over the next ten years, for both traditional uses, such as making ammonia as well as for alternative application, e.g., for running fuel cells. At least in the near future, this “thirst” for hydrogen will be quenched primarily through the use of fossil fuels.

To synthesize hydrogen gas, industry employs steam methane reforming (SMR), which is the most widely used and most economical process for producing hydrogen.[24] Although SMR is a complex process involving many different catalytic steps, as long as natural gas (or CH₄) and hydrocarbon fuels remain at a low or even moderate price, SMR will continue to be the choice technology for the mass production of H₂.

Nonetheless, shedding the habit of fossil fuel entirely is the only way a wholesale shift to a hydrogen economy will work in the long-term. One approach to this goal is to apply steam-reforming methods to alternative renewable materials. Such materials might be derived from crops. Not only do these biomass-conversion schemes turn waste into a valuable product, but,

according to the current philosophy of many researchers there is another benefit: any carbon dioxide released in the processes could be converted into the required biomass by planting new crops. A biomass strategy of hydrogen gas generation could be a useful intermediate step between the current fossil fuel method and the dream of efficient direct water splitting employing solar energy.[24]

In view of the high energy demand and the complexity associated with all reforming processes, it is of interest to explore photocatalysis as an alternative technology for H₂ production from water and/or biomass derived compounds such as methanol.[25]

1.2.1. Photocatalytic H₂ production from water

Overall water splitting for the production of molecular hydrogen using a particulate photocatalyst has been examined since 1980.[7] From the viewpoint of large-scale hydrogen gas production, particulate photocatalyst systems are considered to be advantageous over more complex multilayer or tandem structure devices and have a wider range of potential applications, although a method for separating the simultaneously produced H₂ and O₂ remains to be developed.

Thermodynamically, the overall water splitting reaction is an uphill reaction with a large positive change in Gibbs free energy ($\Delta G^\circ = 237 \text{ kJ mol}^{-1}$). [26] Figure 1.2 shows a schematic illustration of the basic principle of overall water splitting on a heterogeneous photocatalyst. Under irradiation with an energy equivalent to or greater than the bandgap of the semiconductor photocatalyst, electrons from the valence band are excited into the conduction band, leaving holes behind in the valence band. These photogenerated electrons and holes cause reduction and oxidation reactions, respectively. To achieve overall water splitting, the bottom of the conduction band must be located at a more negative potential than the reduction potential of H⁺ to H₂ (0 V vs. NHE at pH 0), while the top of the valence band must be positioned more positively than the oxidation potential of H₂O to O₂ (1.23 V vs. NHE). Therefore, the minimum photon energy thermodynamically required to drive the reaction is 1.23 eV, corresponding to a wavelength of ca. 1000 nm, i.e., in the near infrared region. Accordingly, it would appear to be possible to utilize the entire spectral range of visible light for this process. However, there is an activation barrier in the charge-transfer process between photocatalysts and water molecules, necessitating photon energies greater than the bandgap of the photocatalyst to drive the overall water splitting reaction at reasonable reaction rates. In

addition, the backward reaction, that is, water formation from H_2 and O_2 , must be strictly inhibited, and the photocatalysts themselves must be stable in the reaction.

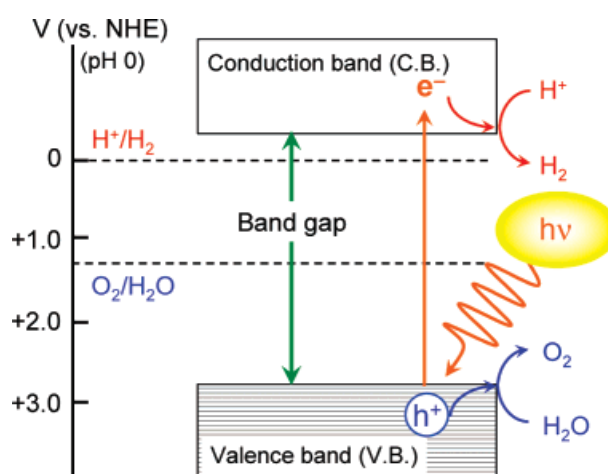


Figure 1.2. Basic principle of overall water splitting on a heterogeneous photocatalyst.[26]

Band levels of various semiconductor materials are shown in Figure 1.3. The band levels usually shift with a change in pH (-0.059 V/pH) for oxide materials. ZrO_2 , $KTaO_3$, $SrTiO_3$ and TiO_2 possess suitable band structures for water splitting. These materials are active for water splitting when they are suitably modified with co-catalysts.

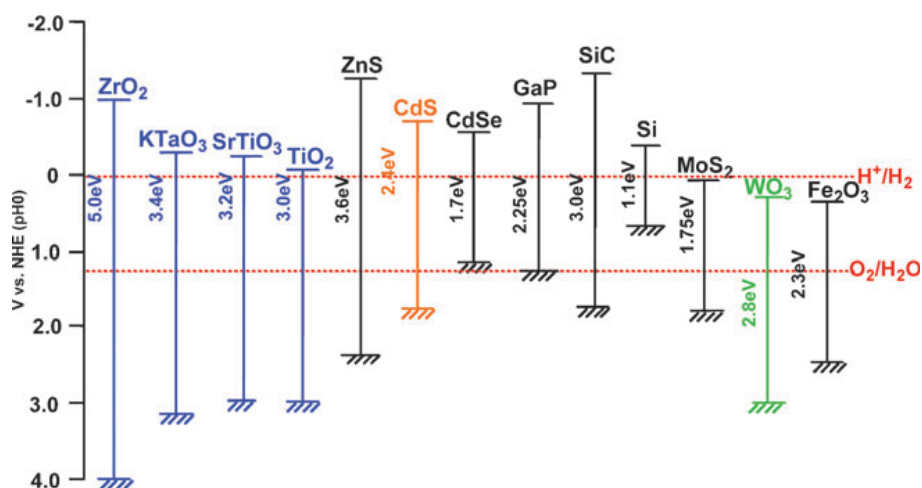
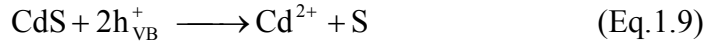
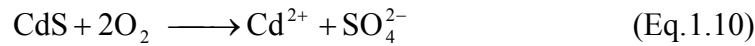


Figure 1.3. Relationship between band structure of a semiconductor and redox potentials of water splitting.[19]

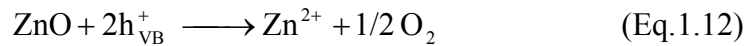
Although CdS seems to have a suitable band position and a bandgap with visible light response it is not active for water splitting into H₂ and O₂. [27] S²⁻ in CdS rather than H₂O is oxidized by photogenerated holes accompanied with the dissolution of the semiconductor and the formation of Cd²⁺ according to the equations: [19]



Usually, the overall process will be:



This reaction is called photocorrosion and presents a fundamental problem for the applicability of a metal sulfide photocatalyst for cyclic water splitting. ZnO is also photocorroded under bandgap excitation even though it is an oxide photocatalyst. [19]



As shown in Figure 1.4, the overall water splitting reaction on a semiconductor photocatalyst occurs in three steps, (1) the photocatalyst absorbs photons the energy of which is greater than the bandgap energy of the material generating photoexcited electron/hole pairs in the bulk, (2) the photoexcited carriers separate and migrate to the surface without recombination, and (3) adsorbed species are reduced and oxidized by the photogenerated electrons and holes to produce H₂ and O₂, respectively. The first two steps are strongly dependent on the structural and electronic properties of the photocatalyst. In general, high crystallinity should have a positive effect on the activity since the density of defects, which act as recombination centers between photogenerated carriers, decreases with increasing crystallinity. The third step, on the other hand, is promoted by the presence of a solid cocatalyst. The cocatalyst is typically a noble metal (e.g., Pt, Rh) or a metal oxide (e.g., NiO, RuO₂) and is loaded onto the photocatalyst surface as a dispersion of nanoparticles to produce active sites and to reduce the activation energy for gas evolution. It is thus important to design both the bulk and the surface properties of the material carefully so as to obtain high photocatalytic activity for this reaction. [26]

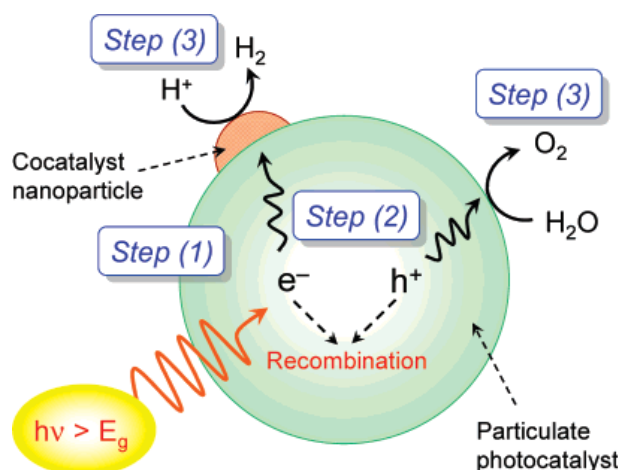


Figure 1.4. Processes involved in the overall photocatalytic water splitting on a heterogeneous photocatalyst.[26]

Although water splitting was first demonstrated using a TiO_2 photoelectrode with some external bias as shown in Figure 1.5, a powdered TiO_2 photocatalyst cannot split water without any modifications such as loading with co-catalysts. Sato and White [7] found that enhanced evolution of H_2 and O_2 took place on a TiO_2 catalyst to which a Pt cocatalyst had been added via photodecomposition of hexachloroplatinate in an aqueous acetic acid solution. In this study, ^{18}O -labeling experiments also confirmed the O_2 production from water. Without Pt, no H_2 was formed on anatase TiO_2 . However, as a drawback, the Pt islands on the surface of TiO_2 were found to also catalyze the reverse of the water splitting reaction, thus limiting the yields in particular at high H_2 partial pressure. Later it was discovered that O_2 production was less than stoichiometric or entirely absent in some cases.[8] This was attributed to the fact that photoinduced TiO_2 tends to strongly adsorb oxygen as O_2^- or as O_2^{2-} .

Following initial reports on the beneficial effect of a NaOH coating on the photocatalytic efficiency,[28] Arakawa's group reported in 1992 that the O_2 evolution activity of TiO_2 could be enhanced significantly by the addition of 0.1-2.2 M Na_2CO_3 to the aqueous catalyst dispersion.[29] Although there were several reports evincing the simultaneous production of H_2 and O_2 in powder systems, either such experiments could not be reproduced or the reaction efficiency was very low.[9, 30]

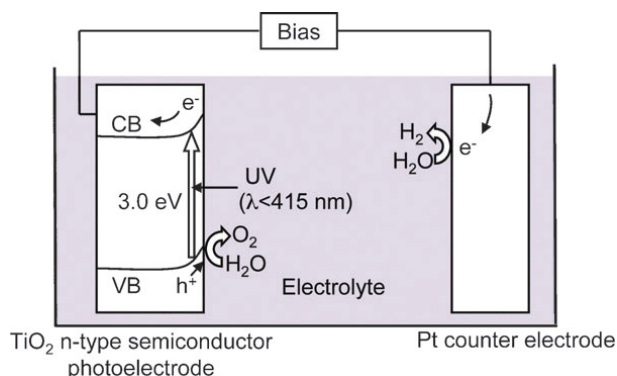
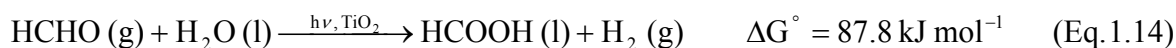


Figure 1.5. Photoelectrochemical water splitting using a rutile TiO_2 photoelectrode.[19]

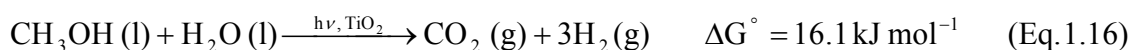
1.2.2. Photocatalytic H_2 production from aqueous methanol solution

One of the most important limitations of photocatalysis for water decomposition is that the process employing pure water is rather inefficient. This is related to the fact that the simultaneous reduction and oxidation of water is a complex multistep reaction involving four electrons. Using sacrificial molecules as electron donors can improve remarkably the H_2 production, [31] as holes are scavenged by these molecules and charge carrier recombination can greatly be reduced. Furthermore, as O_2 is not produced, the back reaction to produce water is suppressed, increasing the H_2 yield and avoiding a subsequent gas separation stage.

Methanol is frequently used as hole scavenger (i.e., as electron donor). The utilization of methanol will only be environmentally sensible provided that it is derived from biomass or from toxic residues that must be disposed of. Adding methanol as electron donor to react irreversibly with the photo-generated VB holes can enhance the photocatalytic electron/hole separation efficiency resulting in higher quantum efficiencies. Since electron donors are consumed in the photocatalytic reaction, their continuous addition is required to sustain H_2 production. Kawai et al. [32] proposed the following overall methanol decomposition reaction mechanism resulting in a lower energy that can be stored as compared with the cyclic splitting of water [33]:



With the overall reaction being



The first two reactions (Eqs. 1.13 and 1.14) have a positive Gibbs free energy, thus both reactions are thermodynamically unfavorable at room temperature. The photon energy will be used to raise the chemical potential of the reactants thus driving the reactions to the products side. The third reaction (Eq. 1.15) has a large negative Gibbs energy, thus it intrinsically provides a barrier for the undesired reverse consumption of the generated hydrogen gas.

Two possible mechanisms are proposed for the TiO₂ photooxidation of methanol: (1) the direct oxidation by photogenerated holes and (2) the indirect oxidation via interfacial $\cdot\text{OH}$ radicals that are products of trapping valence holes by surface $-\text{OH}$ groups or adsorbed water molecules.[34-37] It is still a challenge to distinguish between the two mechanisms in practice due to the lack of suitable probe techniques. Wang et al. [38] have reported recently that the methanol photooxidation pathway, direct or indirect, depends on the molecular species adsorbed at the TiO₂ surface. These authors studied the competitive adsorption process between water and methanol on TiO₂ through the in situ use of sum frequency generation, a nonlinear spectroscopic technique. Accordingly, they concluded that the indirect oxidation by $\cdot\text{OH}$ radicals is the mechanism when water is the dominant surface species with the critical molar ratio between water and methanol for the $\cdot\text{OH}$ radical mechanism being approx. 300. Such a high ratio apparently applies to the photooxidation of methanol by TiO₂ in aqueous systems. If the water content is lower than the critical one, the direct oxidation of methanol by photogenerated holes will be the predominant process at the TiO₂ surface.

Hydroxyl radicals $\cdot\text{OH}$ are known to react with methanol mainly through the abstraction of a hydrogen atom from a C–H bond. Sun and Bolton [39] have used the reaction of methanol with $\cdot\text{OH}$ to determine the quantum yield for the photochemical generation of $\cdot\text{OH}$ radicals in TiO₂ suspensions. The absolute $\cdot\text{OH}$ radical generation rate is based on R–H atom abstraction by $\cdot\text{OH}$ radicals from methanol (Eq. 1.17), followed by monitoring the formation rate of the first principal stable product, i.e., formaldehyde (Eq. 1.18).



In the presence of oxygen, formaldehyde is formed as the dominant stable product in a quantitative reaction (Eq. 1.18), whereas, in the absence of oxygen, formaldehyde is formed through the electron injection into the conduction band of TiO₂, a process called “current doubling”.[40, 41] HCHO can be further oxidized in an analogous manner producing HCOOH and finally CO₂.[42, 43] Asmus et al. [44] showed that the efficiency of the reaction of $\cdot\text{OH}$ radicals with methanol by R-H abstraction is 93 %. The remaining 7 % are accounted

for by methoxy radicals formed through the hydrogen abstraction reaction from the hydroxyl group (Eq. 1.19).



The concentration of the HCHO derivative, divided by a factor of 0.93, is thus the corresponding $\cdot\text{OH}$ radical concentration produced. Sun and Bolton [39] have used the same factor as that found in the homogeneous system (0.93) to calculate the $\cdot\text{OH}$ radical concentration in case of the heterogeneous TiO_2 system.

Bare TiO_2 does not able to catalyze the H_2 evolution even in the presence of methanol. In the presence of an electron donor, such as methanol, and in the absence of O_2 , the excess holes will be consumed and the photogenerated electrons will be trapped near the surface forming trivalent titanium (Ti^{3+}) instead of reducing H^+ (see Figure 1.6a). This phenomenon has been observed by Bahnemann et al. [45] in laser-flash photolysis experiments employing suspensions of colloidal TiO_2 . Moreover, the formation of highly coloured Ti^{3+} centers can even be used technically in a process called photochromism. Loading the TiO_2 surface with small Pt islands creates sinks for the electrons, thus facilitating the separation of e^-/h^+ pairs photogenerated in TiO_2 and promoting the formation of H_2 gas (see Figure 1.6b).[9, 37, 46]

The photocatalytic activity of hydrogen evolution from aqueous methanol solution over TiO_2 depends strongly on the presence of noble metal co-catalysts deposited on its surface and on the way this modification is generated. It also strongly depends on various physicochemical properties of TiO_2 , such as particle size, surface area, crystallinity, morphology, and phase composition. In particular, understanding the relationship between the crystallite-phase compositions and the photocatalytic activity of TiO_2 nanoparticles is of great significance but remains rather ambiguous. In this thesis, a simple hydrothermal route for the synthesis of TiO_2 exhibiting different phases and phase compositions will be presented. This type of research should result in a better understanding of the proper TiO_2 phase and the best phase compositions required to achieve the best yields for the photocatalytic H_2 production from aqueous methanol solution.

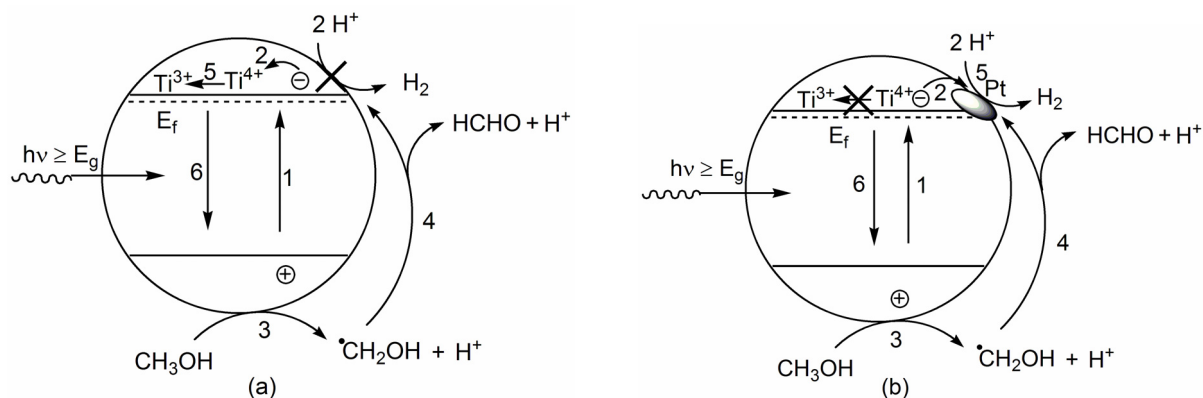


Figure 1.6. Processes involved in photocatalytic H_2 evolution from aqueous methanol solution on (a) bare TiO_2 and (b) on Pt-loaded TiO_2 . (1) photogeneration of charge carriers, e^- and h^+ ; (2) trapping of e^- by Ti^{4+} (a) or by Pt islands (b); (3) first oxidation step of CH_3OH ; (4) formation of HCHO through e^- injection into the conduction band of TiO_2 (current-doubling); (5) formation of Ti^{3+} (a) or reduction of H^+ (b); (6) recombination channel. Note: For simplicity, the formation of $\cdot\text{CH}_2\text{OH}$ radicals by trapped holes ($\equiv\text{Ti}^{\text{IV}}\text{OH}^{\oplus}$) or by $\cdot\text{OH}$ radicals is represented by the hole oxidation step.

1.3. Titanium dioxide (TiO_2) nanomaterials

1.3.1. TiO_2 crystal phases

In nature, TiO_2 exists mainly in three crystal phases: anatase (A), rutile (R), and brookite (B). Each phase displays different physical and chemical properties exhibiting different functionalities. Figure 1.7 shows the basic unit cell structures of the three phases.[47] The crystal parameters, the Ti–O interatomic distances, and the O–Ti–O bond angles for the three phases are summarized in Table 1.2. Rutile and anatase are both tetragonal, containing six and twelve atoms per unit cell, respectively. In both structures, each Ti atom is coordinated to six O atoms and each O atom is coordinated to three Ti atoms. In each case, the TiO_6 octahedron is slightly distorted, with two Ti–O bonds being slightly longer than the other four, and with some of the O–Ti–O bond angles deviating from 90° . The distortion is more pronounced in anatase than in rutile. The structure of rutile and anatase crystals has been described frequently in terms of chains of TiO_6 octahedra sharing common edges.[48] Two and four edges are shared in rutile and anatase, respectively. The third form of TiO_2 , brookite (shown in Figure 1.7c), has a more complicated structure. It has eight formula units in the orthorhombic cell. The interatomic distances and the O–Ti–O bond angles are similar to those of rutile and anatase. The essential difference is that there are six different Ti–O bonds ranging in lengths from 1.87 to 2.04 Å. Accordingly, there are twelve different O–Ti–O bond angles ranging from 77° to 105° . In contrast, there are only two kinds of Ti–O bonds and

O–Ti–O bond angles in rutile and anatase. One can also envision brookite as being formed by joining together the distorted TiO_6 octahedra sharing three edges.[49]

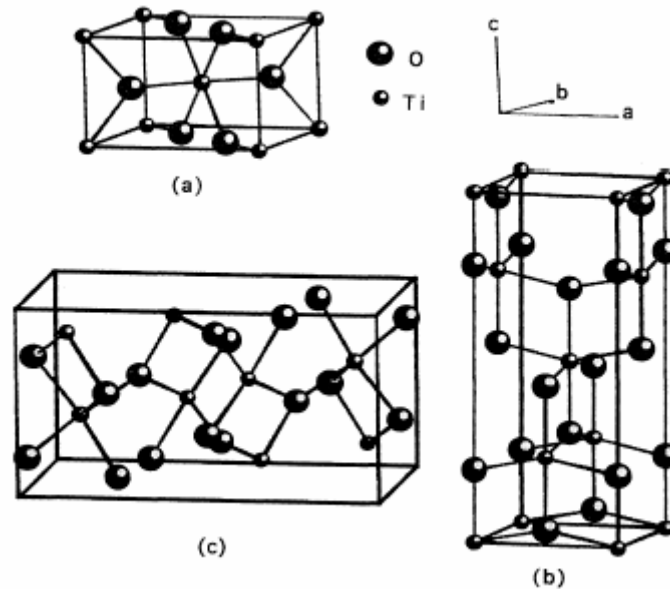


Figure 1.7. Crystal structures of TiO_2 (a) rutile, (b) anatase, and (c) brookite. [47]

Table 1.2. Crystal structure data of TiO_2 . [47]

Nanomaterials	Rutile	Anatase	Brookite
Crystal structure	tetragonal	tetragonal	orthorhombic
Lattice constants (\AA)	$a = 4.5936$ $c = 2.9587$	$a = 3.784$ $c = 9.515$	$a = 9.184$ $b = 5.447$ $c = 5.15$
Space group	$P4_2/mnm$	$I4_1/amd$	$Pbca$
Molecules/cell	2	4	8
Volume/molecule (\AA^3)	31.2160	34.061	32.172
Density (g/cm^3)	4.13	3.79	3.99
Ti–O bond length (\AA)	1.949(4) 1.980(2)	1.937(4) 1.965(2)	1.87~2.04
O–Ti–O bond angle	81.2° 90.0°	77.7° 92.6°	$77.0^\circ \sim 105^\circ$

As a bulk material, rutile is the thermodynamically stable phase; however, solution-phase preparation methods for TiO_2 generally favour the anatase structure. These observations are attributed to two main effects: surface energy and solution chemistry. At very small particle dimensions (nanoscale), it was reported that the transformation sequence among the three TiO_2 phases is size and pH dependent, because the energies of the three phases are

sufficiently close to one another that they can be reversed by small differences in surface energy.[50, 51] If particle sizes of the three nanocrystalline phases are equal, anatase is thermodynamically most stable at diameters below 11 nm, brookite is most stable for crystal sizes between 11 and 35 nm, and rutile is most stable at sizes exceeding 35 nm. However, rutile is stabilized relative to anatase in very acidic solutions, whereas in very alkaline solutions anatase is stabilized relative to rutile and brookite.[52, 53] Even the shape transformation of the TiO₂ nanocrystals was found to be controlled by the surface chemistry as confirmed by theoretical and experimental investigations.[54, 55]

1.3.2. Hydrothermal synthesis of TiO₂ nanomaterials

1.3.2.1. Hydrothermal synthesis as a materials synthesis technology

Hydrothermal research was initiated in the middle of the 19th century by geologists and was aimed at laboratory simulations of natural hydrothermal phenomena. In the 20th century, hydrothermal synthesis was clearly identified as an important technology for material synthesis, predominantly in the fields of hydrometallurgy and single crystal growth.[56] However, the severe (supercritical) reaction conditions required particularly for growing single crystals have discouraged extensive research and commercialization for many materials. In recent years, commercial interest in hydrothermal synthesis has been revived in part because a steadily increasing large family of materials, primarily ceramic powders, has emerged that can be prepared under comparatively mild conditions ($T < 350\text{ }^{\circ}\text{C}$, $P < 100\text{ MPa}$).[57]

Hydrothermal synthesis is a process that utilizes single or heterogeneous phase reactions in aqueous media at elevated temperature ($T > 25\text{ }^{\circ}\text{C}$) and pressure ($P > 100\text{ kPa}$) to crystallize ceramic materials directly from solution.[57] However, frequently researchers also use this term to describe processes conducted at ambient conditions. Syntheses are usually conducted at autogeneous pressure, which corresponds to the saturated vapor pressure of the solution at the specified temperature and composition of the hydrothermal solution. Upper limits of hydrothermal synthesis extend to over $1000\text{ }^{\circ}\text{C}$ and 500 MPa pressure.[57] However, mild conditions are preferred for commercial processes where temperatures are lower than $350\text{ }^{\circ}\text{C}$ and pressures below approximately 50 MPa . The transition from mild to severe conditions is determined mostly by corrosion and strength limits of the construction materials that comprise the hydrothermal reaction vessels. Intensive research has led to a better understanding of hydrothermal chemistry, which has significantly reduced the reaction time, temperature, and

pressure for the hydrothermal crystallization of materials ($T < 200\text{ }^{\circ}\text{C}$, $P < 1.5\text{ MPa}$). This breakthrough has made hydrothermal syntheses more economically viable since processes can be engineered using cost-effective and proven pressure reactor technology and methodologies already established within the chemical process industry.

Hydrothermal synthesis offers many advantages over conventional and non-conventional ceramic synthetic methods. All forms of ceramics can be prepared with hydrothermal synthesis, namely powders, fibers, and single crystals, monolithic ceramic bodies, and coatings on metals, polymers, and ceramics. From the standpoint of ceramic powder production, there are far fewer time- and energy-consuming processing steps required since high temperature calcination, mixing, and milling steps are either not necessary or minimized. Moreover, the ability to precipitate already crystallized powders directly from solution regulates the rate and uniformity of nucleation, growth, and aging, which results in an improved control of size and morphology of crystallites and significantly reduced aggregation levels that are not possible with many other synthesis processes. The elimination/reduction of aggregates combined with narrow particle size distributions in the starting powders leads to optimized and reproducible properties of ceramics because of better microstructure control. Precise control of powder morphology can also be significant. For instance, powders with crystallites having well-developed shapes corresponding to particular crystallographic directions, such as whiskers, plates, or cubes, can be oriented to form materials with single crystal-like properties, such as polymer-ceramic composites or textured ceramic-ceramic composites with anisotropic properties. Another important advantage of the hydrothermal synthesis is that the purity of hydrothermally synthesized powders significantly exceeds the purity of the starting materials. It is because the hydrothermal crystallization is a self-purifying process during which the growing crystals/crystallites tend to reject impurities present in the growth environment. The impurities are subsequently removed from the system together with the crystallizing solution, which does not take place during other synthesis routes such as high temperature calcination.

1.3.2.2. Examples of hydrothermally synthesized TiO₂ nanomaterials

Many research groups have used hydrothermal methods to prepare TiO₂ nanomaterials. For example, anatase TiO₂ nanoparticles were prepared by the hydrothermal reaction of titanium alkoxide in an acidic ethanol-water solution.[58] Briefly, titanium(IV) isopropoxide was added dropwise to a concentrated aqueous solution of ethanol at pH 0.7 (nitric acid) and

reacted at 240 °C for 4 h. The TiO₂ nanoparticles synthesized in this acidic ethanol-water environment consisted mainly of an anatase phase primary structure without any aggregation. The sizes of the particles were controlled within the range of 7-25 nm by adjusting the concentration of the Ti precursor and the composition of the solvent system. Rutile titanium dioxide nanoparticles have also been synthesized directly by a hydrothermal method.[59] The formation of 20 nm rutile particles from titanium isopropoxide at pH 0.5 (nitric acid) has been achieved by vigorous stirring of the solution during the hydrothermal treatment.

Besides TiO₂ nanoparticles, the hydrothermal synthesis of anatase TiO₂ nanorods has been reported. Nian and Teng [60] have found that the hydrothermal treatment of titanate nanotube suspensions under an acidic environment resulted in the formation of single-crystalline anatase nanorods with a specific crystal-elongation direction. The nanotube suspensions were prepared by treatment of TiO₂ in NaOH, followed by mixing with HNO₃ to different pH values. The crystal size of the anatase nanoparticles obtained from the hydrothermal treatment increased with the pH of the suspensions, and nanorods with an aspect ratio up to 6 were obtained at a pH slightly below 7. A mechanism for the tube-to-rod transformation has been proposed on the basis of the crystalline structures of the tubes and rods. The local shrinkage of the tube walls to form anatase crystallites and the subsequent oriented attachment of the crystallites have been suggested to be the key steps involved in the nanorod formation. Rutile TiO₂ nanorods have also been synthesized employing a hydrothermal method. Zhang et al. [61] obtained TiO₂ nanorods by treating a dilute TiCl₄ solution at 333-423 K for 12 h in the presence of acid or inorganic salts. The morphology of the resulting nanorods can be tuned employing different surfactants or by changing the solvent composition. The formation of a film of assembled rutile TiO₂ nanorods deposited on FTO conducting glass was reported by Liu and Aydil.[62] These TiO₂ nanorods were prepared at 80-220 °C for 1-24 h by hydrothermal treatment of a TiCl₄ aqueous solution in the presence of HCl.

TiO₂ nanowires have also been successfully obtained through a hydrothermal method.[63] Typically, TiO₂ nanowires are obtained by treating TiO₂ white powders in an aqueous 10-15 M NaOH solution at 150-200 °C for 24-72 h without stirring in an autoclave. TiO₂ nanowires can also be prepared from layered titanate particles using the hydrothermal method as reported by Wei et al.[64] In their study, layer-structured Na₂Ti₃O₇ was dispersed into a 0.05-0.1 M HCl solution and kept at 140-170 °C for 3-7 days in an autoclave. TiO₂ nanowires were obtained after the product was washed with H₂O and finally dried.

The hydrothermal method has been widely used to prepare TiO₂ nanotubes since it was introduced by Kasuga et al. in 1998.[65] Briefly, TiO₂ powders are suspended in an aqueous

10 M NaOH solution and held at 110 °C for 20 h in an autoclave. The TiO₂ nanotubes are obtained after the products are washed with a dilute HCl aqueous solution and distilled water. The authors proposed the following formation process of TiO₂ nanotubes.[66] Upon treatment of the raw TiO₂ material in the aqueous NaOH solution, some of the Ti–O–Ti bonds are broken and Ti–O–Na as well as Ti–OH bonds are formed. New Ti–O–Ti bonds are subsequently formed after the Ti–O–Na and the Ti–OH bonds reacted with acid and water when the material was treated with an aqueous HCl solution and distilled water. The Ti–OH bond is capable of forming a sheet. Through the dehydration of the Ti–OH bonds by the aqueous HCl solution, Ti–O–Ti bonds or Ti–O–H–O–Ti hydrogen bonds are generated while the bond distance from one Ti to the next Ti on the surface of the substrate decreases. This results in the folding of the sheets and the connection of their ends leading to the formation of a tube like structure. According to this mechanism, the TiO₂ nanotubes are formed during the stage of the acid treatment following the alkaline treatment.

Hydrothermal preparation of anatase TiO₂ single crystals exhibiting a large percentage of reactive facets has recently been reported by Yang et al.[67] Aqueous solutions of titanium tetrafluoride (varying in concentration between 2.67 and 5.33 mM) and hydrofluoric acid (10 wt%) were used as the precursor and the crystallographic controlling agent, respectively, to prepare anatase TiO₂ single crystals. The reaction was carried out in a Teflon-lined autoclave at 180 °C for 2 to 20 h.

Recently, brookite TiO₂ with different morphologies such as nanoparticles, nanoflowers, and nanotubes has also been synthesized employing the hydrothermal methods. Zheng et al. [68] have reported on the synthesis of pure brookite through the hydrothermal treatment of aqueous titanium(IV) salt solutions. Two kinds of starting materials, namely titanium sulfate and titanium tetrachloride, were used in these hydrothermal reactions. The effect of the preparation conditions on the polymorphous form and on the morphology of the titanium dioxide powders has been studied. The results showed that the formation of brookite, anatase, and rutile powders under hydrothermal conditions can be controlled by using specific precursors and pH conditions. Aqueous solutions of titanium sulfate favor the formation of anatase whereas the gel obtained from titanium sulfate solution precipitated by NaOH leads to the formation of brookite. Titanium tetrachloride solutions can lead to all three polymorphs of titanium dioxide depending on the respective pH conditions. High basicity favors the formation of the brookite phase. Pure brookite TiO₂ nanoflowers consisting of single crystalline nanorods were synthesized using a facile one-step hydrothermal process.[69] Briefly, 7.8 ml titanium(IV) butoxide were directly hydrolyzed in a solution of 1.10 g sodium

chloride and 68 ml aqueous ammonia. After stirring for a short time the resulting suspension was transferred to a Teflon-lined autoclave and heated to 180 °C for 24 h. Brookite TiO₂ nanotubes with crystalline multilayer walls have also been synthesized via a simple hydrothermal route.[70] In a typical synthetic procedure, 2.5 g of an anatase TiO₂ powder were dispersed into 20 ml of 10 M NaOH solution and then transferred into a 75 ml Teflon container, which was then kept in an oil bath at 120 °C for 20 h. The white product was washed with dilute HCl, centrifuged several times until the pH values of the final products ranged from 5 to 12, and then was used as a precursor for the next reaction. 50 ml of this precursor were subsequently transferred into a 75 ml Teflon-lined autoclave and kept in an oven at 200 °C for 1 day. The white product was washed with deionized water, filtered, and then dried at 100 °C for 3 h.

It is a common feature of most publications concerning the hydrothermal synthesis of titanium dioxide nanomaterials that TiCl₄, titanium alkoxides, or even titanium dioxide itself can be regarded as suitable precursors. However, the hydrolysis of TiCl₄ and of the titanium alkoxides will inevitably take place in water, even in moist air. Therefore, ice-cooled water baths are often used to ensure a control of the experimental conditions. On the other hand, the use of titanium dioxide as precursor requires extremely high basic reaction conditions. Hence, it is challenging to develop a simple single step method for the preparation of TiO₂ nanomaterials employing aqueous titanium precursors. Recently, Kakihana et al. [71-75] have described the synthesis of TiO₂ nanomaterials employing water soluble titanium complexes; however, the precursor complexes have been self prepared. Nanocrystalline brookite TiO₂ has been obtained by the hydrothermal treatment of a water soluble hexaammonium hexaglycolatodioxotetraperoxotetratitanate(IV) tetrahydrate complex at 200 °C for 24 h at pH 10.[71] Brookite titanium dioxide nanoparticles have also been prepared by microwave-assisted hydrothermal method at 200 °C (heating time 5 min) for 0-60 minutes starting from a peroxy glycolate complex in basic solution.[72] The same materials has also been directly synthesized by the hydrothermal treatment of a titanium glycolate complex at a pH of about 10 in the presence of excess NH₃ aqueous solution or in the presence of ethylenediamine.[74] Single phase rutile has been synthesized by the simple hydrothermal treatment of an aqueous titanium glycolate complex solution at 200 °C for 24 h at pH 3. The resulting powder was composed of 50×150 nm rod-like nanoparticles. The aspect ratio of the prepared particles could be controlled by adding glycolic or lactic acid to the reaction solution.[73] Rutile TiO₂ nanowhiskers have been obtained by controlling the concentration of the glycolic acid additive in the starting aqueous solution of the titanium complex.[75]

In fact, the hydrothermal synthesis of titanium dioxide nanomaterials using commercially available water soluble titanium complexes has rarely been reported. Thus, one of the goals of this thesis is to develop a novel single step method for the preparation of TiO₂ nanomaterials employing commercially available water soluble titanium complexes. Titanium(IV) bis(ammoniumlactato) dihydroxide (TALH) has attracted our attention as a water soluble precursor since this material is commercially available, stable in a wide range of pHs (2-9) at ambient temperature in air, and rather inexpensive (in comparison with TiCl₄ or titanium alkoxides). Table 1.3 summarizes the titanium dioxide coatings and composites previously prepared employing the TALH complex as the titanium source.

Table 1.3. Summary of titanium dioxide coatings and composites products prepared employing the titanium(IV) bis(ammoniumlactato) dihydroxide complex as a titanium source.

Method	Product	Reference
Hydrolysis and condensation	Anatase TiO ₂ coated silica gel	Hanprasopwattana et al. [76]
	TiO ₂ coated silicon, glass, and plastic substrates	Baskaran et al. [77]
	Anatase TiO ₂ nanoparticles on carbon nanotubes	Lee et al. [78]
	Anatase TiO ₂ nanoparticles coating on barium ferrite	Lee et al. [79]
Layer-by-layer self-assembly	Hollow TiO ₂ spheres	Caruso et al. [80]
	Gold-titania core-shell nanoparticles	Mayya et al. [81]
	TiO ₂ thin film	Shi et al. [82]
	TiO ₂ thin film containing anatase and brookite phases	Katagiri et al. [83]
Sol gel	Ag-doped mesoporous TiO ₂	Li et al. [84]
Hydrothermal	Uniformly sized anatase nanoparticles	Möckel et al. [85]

The comparatively high stability of titanium(IV) bis(ammoniumlactate) dihydroxide (TALH), as compared with titanium alkoxides, towards hydrolytic attack follows from its specific structure. TALH is a chelate compound [77] in which all six-coordinate positions of Ti are occupied. Bonding between the ammonium cation and the remainder of TALH should be similar to that in ammonium lactate which is a weak acid/weak base salt. The ionized structure of TALH is given in Figure 1.8a. Based on conductivity data, Möckel et al. [85] found that TALH is partly dissociated into complex anion and the NH_4^+ cation, while a substantial fraction is not ionized. These authors assumed that the structure of this fraction is similar to the model shown in Figure 1.8b.

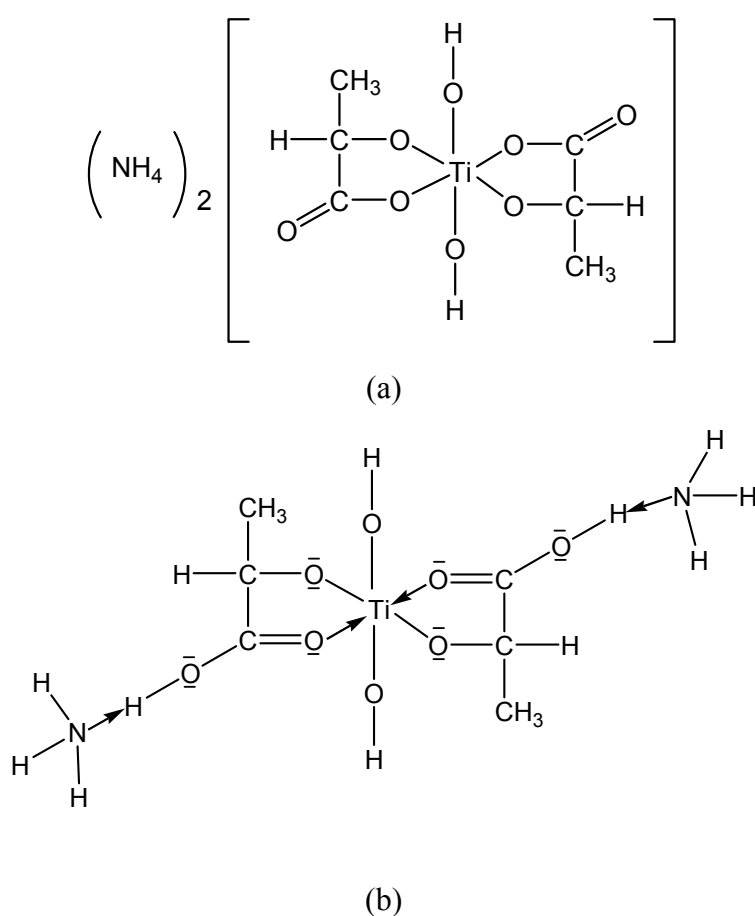


Figure 1.8. (a) Assumed molecular structure of the ionized form of TALH, (b) assumed molecular structure of the non-ionized form of TALH [85]. Arrows indicate donated electron pairs.

1.3.3. Modification of TiO₂ nanomaterials

Modification of TiO₂ with noble metals, e.g., Pt, Au, Pd, Rh, Ni, Cu, and Ag has been reported to be a very effective method for the enhancement of its photocatalytic activity.[16] Among these noble metals, Pt modified TiO₂ has usually shown the best photocatalytic activity, particularly, for hydrogen production from aqueous methanol solution.[86, 87] Since, as concluded from the work functions of TiO₂ (4.6-4.7 eV) and Pt (5.36-5.63 eV),[88] the Fermi level of the Pt metal is more positive than that of TiO₂, the photo-excited electrons can readily be transferred from the TiO₂ conduction band to the Pt particles deposited on its surface, while photo-generated valence band holes remain on the TiO₂. The electron transfer to the metal islands will greatly reduce the probability of electron-hole recombination, resulting in a more efficient electron/hole separation and thus enhanced photocatalytic activities. Figure 1.9 shows the proposed reactions scheme.

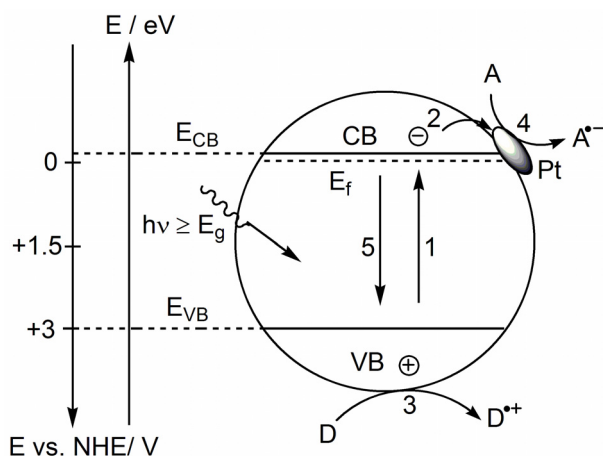


Figure 1.9. Principle mechanism of photocatalytic process occurring at Pt-loaded spherical TiO₂ particles. (1) photogeneration of charge carriers, e⁻ and h⁺; (2) trapping of e⁻ at Pt islands (b); (3) first oxidation step of electron donor; (4) reduction of electron acceptor; (5) recombination channel. Note: for simplicity, the first oxidation step by trapped holes ($\equiv\text{Ti}^{\text{IV}}\text{OH}^{\oplus}$) or by $\cdot\text{OH}$ radicals is represented by the hole oxidation step.

Anpo and Takeuchi [89] employed the electron spin resonance technique to investigate the electron transfer from TiO₂ to Pt particles. They observed that the Ti³⁺ signals increased with irradiation time and that the loading with Pt reduced the amount of Ti³⁺. This observation indicates the occurrence of electron transfer from TiO₂ to the Pt particles. As electrons accumulate on the noble metal particles, their Fermi level will shift closer to the conduction band of TiO₂, resulting in a more negative positions of the energy levels. This is beneficial for hydrogen production. Furthermore, smaller metal particles deposited on the TiO₂ surface

exhibit a more negative Fermi level shift.[90] Accumulated electrons on the metal particles can then be transferred to protons adsorbed at their surface resulting in the formation of adsorbed hydrogen atom that subsequently combine to form molecular hydrogen. Therefore, noble metals with suitable work functions can promote the electron transfer, thus leading to higher photocatalytic activity. It should be noted, however, that although the loading of the TiO₂ surface with noble metal islands can reduce the electron/hole recombination to some extent, molecular hydrogen production in pure water-splitting system will still be difficult to achieve, because of (i) the recombination of electron/hole pairs cannot be completely eliminated and (ii) the backward reaction of H₂ and O₂ to form H₂O is thermodynamically favorable and can also be catalyzed at noble metal surfaces.

Besides the modification of TiO₂ with Pt nanoparticles, reports have also shown that TiO₂ surfaces modified with electron conducting polymers such as nafion and polypyrrole exhibit enhanced photocatalytic activity.[91-97] Photoelectrochemical studies report the use of polypyrrole coatings to inhibit the photocorrosion of narrow bandgap semiconductors such as n-GaP and CdS.[98] It was proposed that polypyrrole has the ability to channel the photogenerated holes from the surface of the semiconductor to the polymer/solution interface. Consequently, the role of the polymer is to transport the photogenerated holes to the polymer/electrolyte interface at a rate that is considerably faster than the self-oxidation of the semiconductor.[99] The proposed role of the polypyrrole polymer is shown in Figure 1.10.

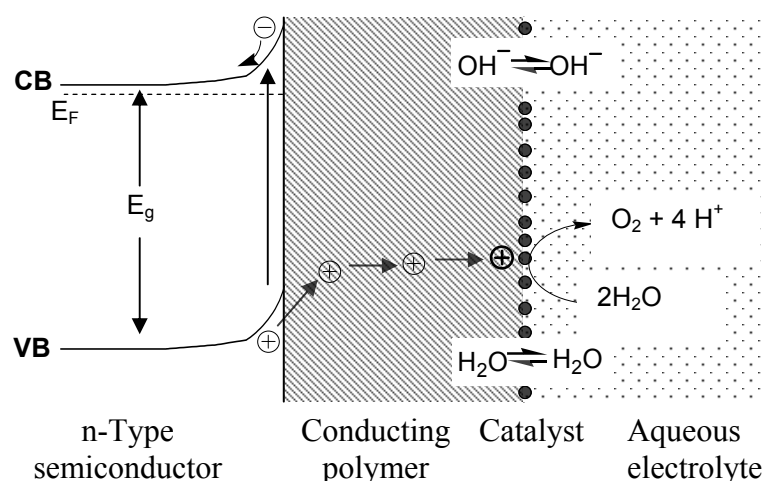


Figure 1.10. Conceptual model for the suppression of the photodegradation of a n-type semiconductor and the promotion of the water oxidation reaction.[98]

Modification of TiO₂ with Pt nanoparticles is usually performed by a photochemical deposition method or by an impregnation method, whereas modification of TiO₂ with polypyrrole is achieved by an oxidative polymerization reaction using ferric chloride in case of suspended nanoparticles or by electrochemical polymerization when electrodes are employed. In this thesis, a simple method for the in situ simultaneous modification of TiO₂ with Pt–polypyrrole nanocomposites will be presented. The proposed method is efficient and depends on the reduction of Pt(IV) to Pt(0) accompanied by the oxidative polymerization of pyrrole monomers at ambient temperature.

2. Materials and Experimental Methods

2.1. Materials

Titanium dioxide Aeroxide P25 (Evonik, Germany), titanium dioxide Hombikat UV100 (Sachtleben, Germany), titanium(IV) bis(ammoniumlactate) dihydroxide (TALH, 50 % aqueous solution, Sigma-Aldrich), hexachloroplatinic acid hexahydrate (Alfa Aesar), urea (Aldrich), and methyl viologen dichloride hydrate (Sigma-Aldrich) were used as received. Pyrrole (Aldrich) was distilled under vacuum prior to use. It was used immediately or refrigerated and stored under Ar in the dark. Formaldehyde solution (Aldrich), p-hydroxyphenylacetic Acid (Fluka), horseradish peroxidase (Fluka), and all other reagents (Sigma-Aldrich) were of analytical grade and used as received. All aqueous solutions were prepared with deionized water from a SARTORIUS ARIUM 611 apparatus (resistivity =18.2 MΩ cm). Suppliers and denotation of the commercial titanium dioxide powders and precursors are summarized in Table 2.1.

Table 2.1. Suppliers and denotation of the commercial titanium dioxide powders and precursors.

Product	Supplier	Denotation
Titanium dioxide Aeroxide P25	Evonik, Germany	TiO ₂ P25
Titanium dioxide Hombikat UV100	Sachtleben, Germany	TiO ₂ UV100
Titanium(IV) bis(ammoniumlactate) dihydroxide	Sigma-Aldrich, Germany	TALH
Rutile nanoparticles	Cristal Global Chemicals, UK	R25 and R34

2.2. Synthesis of TiO₂ nanomaterials

2.2.1. Synthesis of TiO₂ anatase nanoparticles

TiO₂ anatase nanoparticles were prepared by the hydrothermal treatment of TiO₂ P25 in alkaline solution. In a typical synthesis process, 1.0 g TiO₂ and 100 ml sodium hydroxide aqueous solution (10 M) were mixed and magnetically stirred for 2 h. The resulting suspension was poured into a Teflon-lined stainless steel autoclave (Berghof, DAB-3) and then heated in an electric furnace held at 120 °C for 24 h. The autoclave was allowed to naturally cool down to room temperature. The resulting white precipitate was vacuum filtrated and washed with HCl solution (0.1 M) and deionized water until neutralization. The obtained precipitate was redispersed in HCl solution (0.5 M HCl) and stirred overnight followed by filtration and thorough washing with deionized water. The isolated powder was dried at 70 °C in an oven and post-heated in air atmosphere at 400 °C for 2 h (denoted as TiO₂ P25HT).

2.2.2. Synthesis of TiO₂ rutile nanorods

Rutile TiO₂ nanorods were prepared by thermal hydrolysis of titanium(IV) bis(ammoniumlactate) dihydroxide (TALH). The thermal hydrolysis experiments were carried out in a 200 ml Teflon cup enclosed in a stainless steel autoclave (Berghof, DAB-3). In a typical experiment, 10 ml of titanium(IV) bis(ammoniumlactate) dihydroxide aqueous solution and 40 ml deionized water were mixed. The resulting solution was transferred into the Teflon cup. Afterwards, the Teflon cup was sealed in the autoclave and placed into an electric furnace held at 200 °C for different reaction times, namely, 12, 24, 48, 72 and 96 h. Then the autoclave was cooled naturally in air. The resulting powders were separated by centrifugation, sonicated and washed several times with water until a clear supernatant solution was obtained, and then dried overnight at 60 °C in an oven. The dried powders obtained after 24, 48, 72, and 96 h of thermal hydrolysis are denoted as AR24, AR48, R72, and R96, respectively. The yield is found to be not less than 90 % of the expected yield from the complete thermal hydrolysis of the available TALH complex.

2.2.3. Synthesis of TiO₂ anatase nanoparticles, anatase/brookite mixtures, and brookite nanorods

Anatase nanoparticles, anatase/brookite mixtures, and brookite nanorods were prepared by the thermal hydrolysis of titanium(IV) bis(ammoniumlactate) dihydroxide aqueous solution

(TALH) in the presence of urea. The urea concentrations were varied from 0.1 M up to 7.0 M. The thermal hydrolysis experiments were carried out in a 250 ml Teflon cup enclosed in a stainless steel autoclave (Berghof, DAB-3). 10 ml of the TALH aqueous precursor and the prepared aqueous solution containing the desired amount of urea were mixed followed by the addition of deionized water to reach a final volume of 100 ml. The resulting solution was transferred into the Teflon cup. Afterwards, the Teflon cup was sealed in the autoclave and placed into an electric furnace held at 160 °C for required times, namely, 6, 12, 24, 48, and 72 h. Then the autoclave was cooled in air. The resulting powders were separated by centrifugation, washed three times with water, and dried overnight at 60 °C in an oven. The yield is found to be not less than 97% of the expected yield from the complete thermal hydrolysis of the available TALH complex.

The dried powders obtained employing different urea concentrations and after different reaction times are denoted as Ac,t, ABc,t, and Bc,t, where A, B, c, and t denote anatase, brookite, urea concentration, and reaction time, respectively. The denotation of the newly synthesized powders are listed in Table 2.2. A few experiments have also been performed at 120 and 200 °C for mechanistic studies.

Table 2.2. Denotation of anatase nanoparticles, anatase/brookite mixtures, and brookite nanorods obtained by thermal hydrolysis of TALH complex employing different urea concentrations and different reaction times.

Urea concentration (M)	Reaction time (h)	Denotation
0.1	24	A _{0.1,24}
0.5	24	AB _{0.5,24}
1.0	24	AB _{1.0,24}
1.5	24	AB _{1.5,24}
2.0	24	AB _{2.0,24}
3.0	24	AB _{3.0,24}
4.0	24	AB _{4.0,24}
5.0	24	AB _{5.0,24}
6.0	24	B _{6.0,24}
7.0	24	B _{7.0,24}
1.0	6	AB _{1.0,6}
1.0	12	AB _{1.0,12}
1.0	48	AB _{1.0,48}
1.0	72	AB _{1.0,72}

2.3. Modification of TiO₂ nanomaterials

2.3.1. Modification of TiO₂ with Pt nanoparticles via a photochemical deposition method

Pt-loaded TiO₂ nanomaterials were prepared by a photochemical deposition method.[100, 101] To prepare 0.5 wt% Pt-loaded TiO₂, 0.5 g of TiO₂ powder were suspended by stirring in 200 ml aqueous methanol solution (1.0 vol.%) containing the desired amount of hexachloroplatinic acid (257 μ l, 0.05 M). The resulting suspension was irradiated under UV(A) light by a Philips Hg lamp (2.0 mW cm⁻²) for 15 h. The powder was separated by centrifugation, washed with water, and dried under vacuum.

2.3.2. Modification of TiO₂ with Pt-polypyrrole nanocomposites

TiO₂ nanoparticles were modified by Pt-polypyrrole nanocomposites employing the in situ simultaneous reduction of Pt(IV) to Pt(0) accompanied by the oxidative polymerization of pyrrole monomers at ambient temperature.[102] In a typical experiment, 100 ml of deionized water was purged with argon in a conical flask for 30 min to remove dissolved O₂. Under constant stirring, the hexachloroplatinic acid solution containing the desired amount of Pt (0.5-10.2 mg) was added, followed by the addition of the required amount of pyrrole monomers (3.75-37.50 μ mol). Subsequently, 0.5 g TiO₂ was immediately added to the mixture. The resulting suspension was magnetically stirred covered for 24 hours at ambient temperature. The modified powder was separated by centrifugation, washed with water, and dried under vacuum.

2.3.3. Modification of TiO₂ with Pt nanoparticles using colloidal Pt suspension

Colloidal Pt nanoparticles (particle diameters ca. 3 nm according to the reported method [45]) have been prepared by reduction of 1000 ml 3.0 \times 10⁻⁴ M hexachloroplatinic acid solution with 1.7 \times 10⁻³ M sodium citrate at 100 °C for 1 h under reflux.[45] Excess ions in the resulting colloidal suspension were removed with an ion exchange resin (Amberlite MBI) until a specific conductivity of ca. 3 μ S cm⁻¹ was reached. 0.5 wt% Pt-loaded TiO₂ was prepared by suspending 0.25 g TiO₂ powder in 80 ml deionized water by sonication, followed by the addition of the desired amount of as-prepared colloidal Pt suspension (21.4 ml) under continuous magnetic stirring. The stirring was kept overnight to insure the homogenous dispersion of the Pt nanoparticles. After evaporation under vacuum at room temperature, a grayish powder was obtained. The obtained powder was dried at 60 °C in an oven overnight.

2.4. Characterization of TiO₂ nanomaterials

2.4.1. X-ray diffraction

X-ray diffraction (XRD) data for the Rietveld phase analysis of TiO₂ have been recorded on a Phillips PW1800 diffractometer using a reflection geometry with variable divergence slits, Cu-K $\alpha_{1,2}$ radiation and a secondary monochromator. Three thousand data points were collected with a step width of 0.02° and 2 seconds measurement time per step in the 2 θ range from 5 or 20 to 80°. The phase analysis by the Rietveld method was carried out by using the TOPAS 2.0 (Bruker AXS) software. During the refinements general parameters such as scale factors, one background parameter, and the zero point error were optimized. Profile shape calculations were carried out on the basis of standard instrumental parameters using the fundamental parameter approach implemented in the program, varying also the average crystal size (integral breadth) of the reflections. Lattice parameters and crystallite size of all phases were refined. Structural data for the known phases were taken from the PDF-2 database with PDF numbers: anatase [21-1272], rutile [21-1276], and brookite.[29-1360]

2.4.2. Field-emission scanning electron microscopy

Field-emission scanning electron microscopy (FE-SEM) measurements were carried out on a JEOL JSM-6700F field-emission instrument using a secondary electron detector (SE) at an accelerating voltage of 2.0 kV.

2.4.3. High-resolution transmission electron microscopy

High-resolution transmission electron microscopy (HR-TEM) was performed at 200 kV on a field-emission instrument of the type JEM-2100F (JEOL Ltd., Tokyo, Japan) with an ultra-high resolution pole piece (CS = 0.5 mm, CS = 1.2 mm), which provides a point-resolution better than 0.19 nm. Sample preparation was made by dispersing powder in ethanol and dropping ca. 10 μ l of the suspension onto a copper-supported perforated carbon film of the type Multi A (Quantifoil Micro Tools GmbH, Jena, Germany), on which it was dried. Observation of powder particles was made in specimen areas, which were locally not supported by the carbon film.

2.4.4. Specific surface area measurements

Single-point standard BET surface area measurements were carried out employing a Micromeritics AutoMate 23 instrument. The gas mixture used for the adsorption determinations was 30 % N₂ and 70 % He. The TiO₂ samples were previously heated to 150 °C for approximately 60 min in order to clean the surface of adsorbed organic compounds and water. The nitrogen adsorption and desorption isotherms at 77 K were measured using a Quantachrome Autosorb 3B after the samples were vacuum-dried at 200 °C overnight. The sorption data were analyzed using the Barrett-Joyner-Halenda model with Halsey equation to determine the pore diameters.

2.4.5. Diffuse reflectance spectroscopy

Diffuse reflectance powders spectra of the TiO₂ nanomaterials were recorded on a Varian Cary 100 Scan UV-Vis spectrophotometer equipped with a labsphere diffuse reflectance accessory. Labsphere USRS-99-010 was employed as a reflectance standard. Reflectance was converted by the instrument software to F(R) values according to the Kubelka-Munk theory. The bandgap was obtained from a plot of the modified Kubelka-Munk function $[F(R) \cdot E]^{1/2}$ versus energy of the exciting light (E) assuming that TiO₂ is an indirect crystalline semiconductor.[103, 104]

2.4.6. Infrared and Raman spectroscopy

Infrared spectra (IR) were recorded with a Bruker FT-IR spectrophotometer using KBr pellets, whereas Raman spectroscopy was carried out with a Bruker Optics IFS66v/s FTIR spectrometer equipped with FRA-106 Raman attachment. For each spectrum, 32 scans of the undiluted sample were measured in backscattering geometry.

2.4.7. X-ray photoelectron spectroscopy

X-ray photoelectron spectroscopy (XPS) measurements were carried out employing an Al/Mg twin anode X-ray spectrometer (Leybold-Heraeus) equipped with a hemispherical analyzer. Al K_α radiation and normal emission geometry were used for all measurements. The binding energies of all peaks were referenced to the O 1s line (529.80 eV)[105] originating from TiO₂.

2.4.8. Flatband potential measurements

The flatband potentials have been measured by impedance spectroscopy using Mott-Schottky plots. TiO₂ nanomaterial paste for the fabrication of electrodes for impedance measurements was obtained by mixing 1 ml of water and 100 mg of TiO₂ nanomaterial powder homogeneously by sonication. An appropriate amount of the TiO₂ suspension was spread on a conductive fluorine-tin oxide (FTO) glass with a glass rod, using adhesive tapes as spacers followed by drying in air at 100 °C for 2 h. The electrical contact was formed on the uncoated area of the substrate using silver paint and copper wire. This contact area was later covered with nonconducting epoxy resin to isolate it from the electrolyte solution. A glass rod was placed over the copper wire for better handling. The electrochemical setup for impedance measurements consisted of three electrodes: the working electrode (TiO₂ film), a platinum wire used as counter electrode, and an Ag/AgCl, NaCl (3.0 M) electrode as reference (+0.21 vs. NHE). The experiments were performed in aqueous 0.1 M KCl solutions at pH 7. The potential was systematically varied between +1.00 and -1.00 V with the frequency range being modulated between 10 Hz to 1000 Hz by an IVIUMSTAT electrochemical interface and impedance analyzer.

2.4.9. Quasi Fermi level measurements

The quasi-Fermi energy was measured according to the method of Roy et al. [106] using methyl viologen dichloride (MV²⁺, E_{red} = -0.44 V) as pH independent redox system.[106-108] In a typical experiment, 30 mg of the photocatalyst and 6 mg of methyl viologen dichloride were suspended in a 100 ml flask in 50 ml of 0.1 M KNO₃. A platinum flag and Ag/AgCl served as working and reference electrodes, respectively, and a pH meter for recording the proton concentration. HNO₃ (0.1 M) and NaOH (0.1 M) were used to adjust the pH value. The suspension was magnetically stirred and purged with nitrogen gas throughout the experiment. Initially, the pH of the suspension was adjusted to around pH 1. Then, the suspension was irradiated by an Osram XBO 450 W Xenon lamp in a Müller LAX 1000 lamp housing. Stable photovoltages between the working and reference electrodes were recorded about 30 min after changing the pH value by a VOLTCRAFT digital multimeter. A schematic drawing representing the experimental set-up is shown in Figure 2.1.

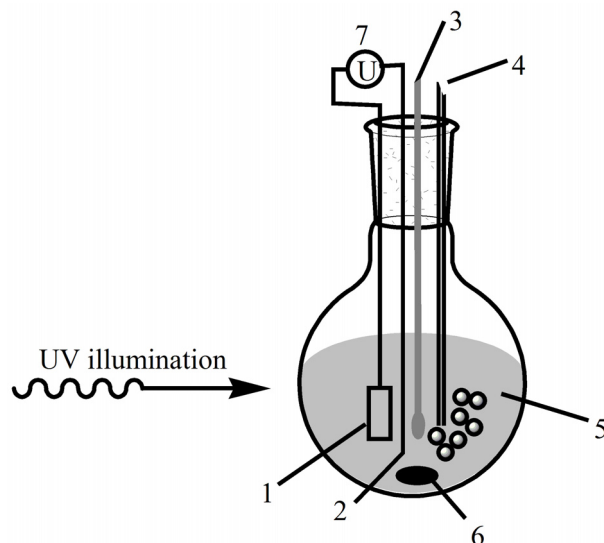


Figure 2.1. Schematic presentation of the experimental setup employed for the quasi-Fermi level potential determination: 1- working electrode (Pt), 2- reference electrode (Ag/AgCl), 3- pH meter electrode, 4- N₂ gas sparger, 5- catalyst suspension, 6- magnetic stirring bar, 7- multimeter.

2.5. Experimental setup for the evaluation of the photocatalytic activities of TiO₂ nanomaterials

2.5.1. Photocatalytic H₂ production

The photocatalytic molecular hydrogen production tests were performed in a double jacket Duran glass reactor (110 cm³) with three outlets (see Figure 2.2). Two outlets were equipped with stopcocks for gas purging the headspace above the liquid phase. The reactant was introduced into the reaction vessel through the third outlet. In addition, this outlet was used to withdraw the evolved gases via a silicone rubber septum (Macherey-Nagel, Germany). The temperature of the reactor was maintained by continuously running cooling water through the jacket of the reactor. This volume of water was also utilized as an infrared filter.

In a typical run, 0.0375 g of the modified TiO₂ photocatalysts were suspended in 75 ml of an aqueous methanol solution (0.03 M, 2.25 mmol methanol) by sonication. The suspension was transferred to the photoreactor and bubbled with Ar for 30 min to remove any dissolved O₂. The reactor was sealed with a silicone rubber septum and repeatedly flushed with Ar for another 30 min until no O₂ and N₂ were detected by gas chromatography in the headspace above the solution. Subsequently, the stopcocks were closed and the photoreactor was connected to the cooling system. The photoreactor was irradiated from the outside using a Osram XBO 1000 W Xenon lamp in a Müller LAX 1000 lamp housing. The evolved gas was sampled at a constant rate through the silicone rubber septum by using a locking-type syringe.

The sampled gas was quantitatively analyzed using a gas chromatograph (Shimadzu 8A, TCD detector). The GC was equipped with a molecular sieve 5 A packed column for hydrogen analysis. Ar was used as the carrier gas. A Porapak Q packed column was used to analyse the carbon dioxide content with He as the carrier gas.

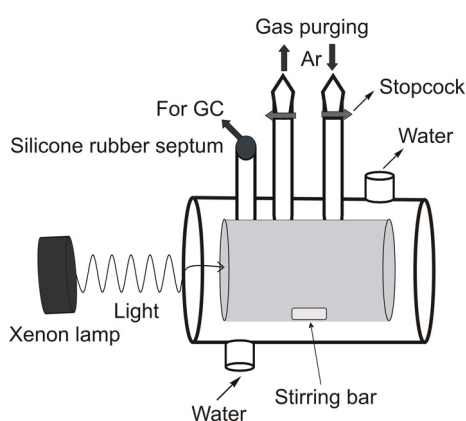


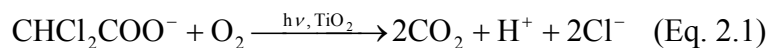
Figure 2.2. Schematic presentation of the water cooled reactor used to assess the photocatalytic production of H_2 .

2.5.2. Photocatalytic degradation of dichloroacetic acid

The photocatalytic DCA degradation was measured in a 60 ml double jacket quartz glass reactor using a pH-stat technique (see Figure 2.3). In a typical run, 0.03 g of the photocatalyst was suspended in 60 ml of aqueous 0.01 M KNO_3 by sonication before the addition of 0.06 mmol DCA into the slurry. The pH was then adjusted to pH 3 by addition of 0.1 M HNO_3 or NaOH as needed. The temperature of the suspension was maintained at 25 °C. The suspension was vigorously stirred without illumination for 30 minutes to attain adsorption equilibrium of the DCA molecules on the photocatalyst surface and continuously purged with air to ensure a constant O_2 concentration throughout the experiment. After this adsorption period, UV(A) illumination was provided by a high-pressure Xe-lamp (OSRAM HBO 450 W). A UV(A)-Vis illumination was achieved employing a cut-off filter (WG 320) which eliminates UV-radiation below $\lambda = 320$ nm. The intensity of UV(A) illumination was 60 mW cm^{-2} at the entrance window of the photoreactor as measured by a UV light meter (ultraviolet radiometer LTLutron UVA-365).

The photocatalytic degradation of dichloroacetic acid, DCA, as model pollutant was performed at pH 3. The pK_a of DCA is 1.29, [49] and it thus exists in its anionic form in aqueous solutions at $pH > 2$. The photocatalytic oxidation of one DCA anion results in the

formation of one proton, two CO₂ molecules, and two Cl⁻ ions according to equation 2.1. The pH of the suspension was maintained constant during the photocatalytic experiments using a pH-stat technique as described by Bahnemann et al.[109, 110]



The rate of the photodegradation of DCA was followed by measuring the amount of OH⁻ added to keep the pH constant thus measuring the amount of H⁺ formed which is equivalent to the amount of DCA degraded. The mineralization of DCA was confirmed by total organic carbon (TOC) measurements at the end of the experimental runs.

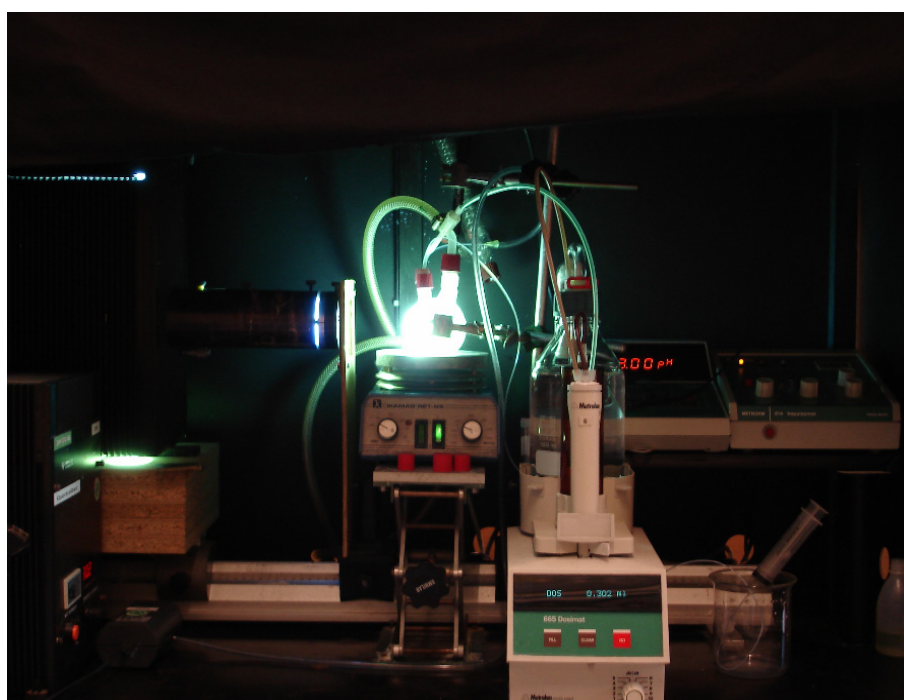


Figure 2.3. Real image for the experimental setup used for the photocatalytic degradation of dichloroacetic acid (DCA).

2.5.3. Photocatalytic decomposition of acetaldehyde

Photocatalytic decomposition of gaseous acetaldehyde was carried out in an experimental setup consisting of a gas supply, the photoreactor, and gas chromatograph for acetaldehyde analysis (GC 955 Syntech Spectras) (see Figure 2.4). To obtain the starting concentration of acetaldehyde of 1 ppm at a relative humidity of 50 %, a gaseous mixture of dry air (500 ml min⁻¹), wet air (500 ml min⁻¹, relative humidity 100 %), and acetaldehyde (6 ml min⁻¹) was prepared. This gas stream was continuously flowed through the photoreactor, and the photocatalytic oxidation of acetaldehyde was obtained over TiO₂ films with a geometrical area of about 30 cm² illuminated with UV(A) light at an intensity of 1.0 mW cm⁻² using a

Philips Hg lamp and a mean wavelength of $\lambda = 350$ nm. This TiO_2 films were prepared by mixing 1.0 ml of water and 100 mg of TiO_2 powder thoroughly by sonication. The TiO_2 suspension was spread on a glass with a glass rod, using adhesive tapes as spacers, and was then allowed to dry in air at 100°C for 2 h.

In some cases, the photocatalytic oxidation of acetaldehyde was obtained over 0.5 g TiO_2 powder. It was spread and pressed in a geometrical area of 6.25 cm^2 and a depth of 2 mm employing a Plexi-Glass sample holder. UV(A) light with an intensity of 1.0 mW cm^{-2} and mean a wavelength of $\lambda = 350$ nm was used for illumination.

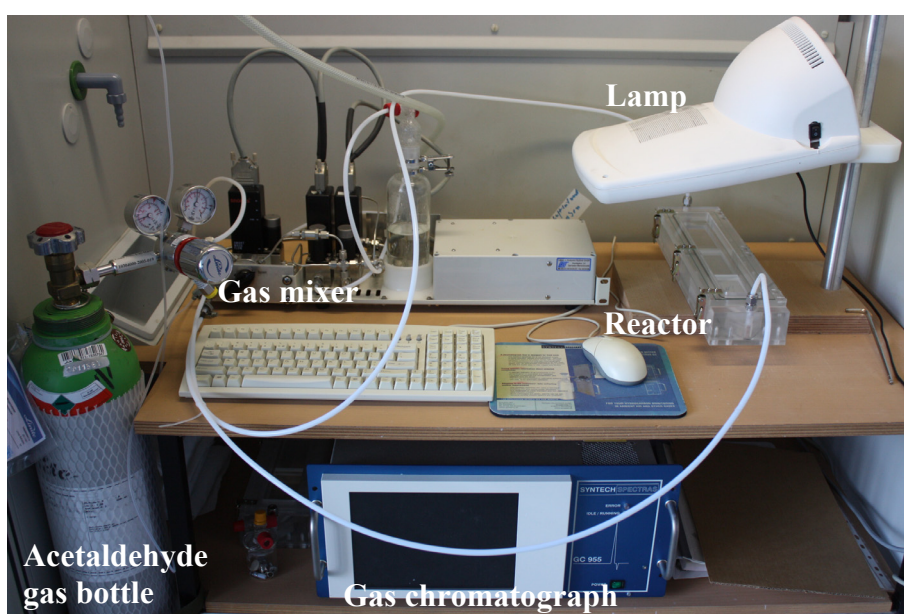
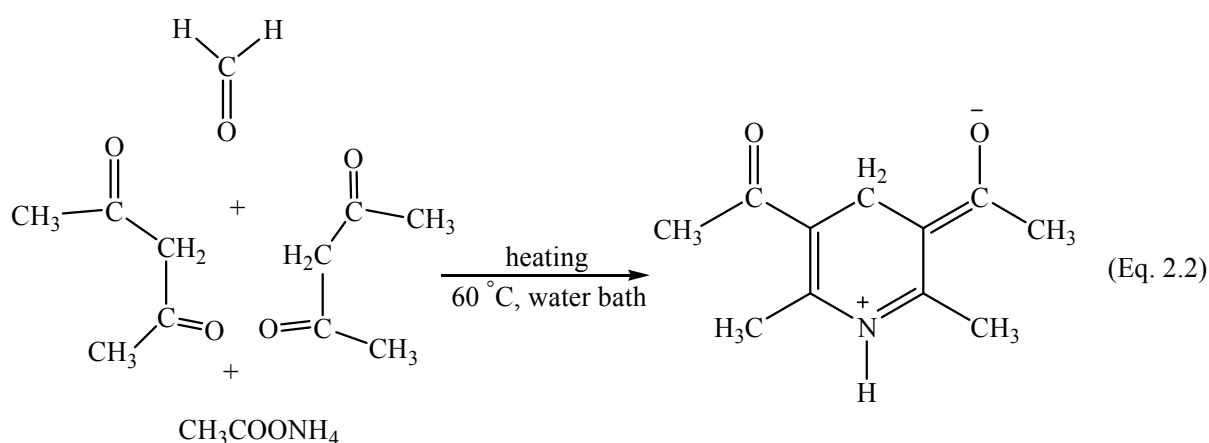


Figure 2.4. Real image for the experimental setup used for the photocatalytic decomposition of acetaldehyde.

2.6. Analysis of methanol photooxidation products

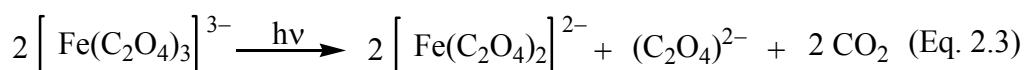
The amount of formaldehyde formed by the photooxidation of methanol was determined by the Nash method, based on the Hantzsch reaction.[111] Formaldehyde reacts with acetylacetone in the presence of a nitrogen donor such as ammonium acetate to produce a yellow colour owing to the formation of diacetyldihydrolutidine (see equation 2.2). Under optimum conditions as previously reported [111], the molar absorptivity of diacetyldihydrolutidine at 412 nm was found to be $8430 \text{ mol}^{-1} \text{ l cm}^{-1}$ in good agreement with the previously reported value $8000 \text{ mol}^{-1} \text{ l cm}^{-1}$. Spectrophotometric measurements were carried out using a Varian Cary 100 UV-Vis spectrophotometer. The concentration of formic acid was determined using a high performance DIONEX ICS-1000 ion chromatograph equipped with a $2 \times 50 \text{ mm}$ Ion Pac AS9-HC column and a conductivity detector. The mobile phase was an alkaline solution of $0.008 \text{ M Na}_2\text{CO}_3$ and 0.0015 M NaHCO_3 . A Shimadzu GCMS-QP2010 gas chromatograph equipped with a Stabilwax-DA column (Restek Germany) was used to determine the concentration of 1,2-ethanediol. The carrier gas was He. Hydrogen peroxide and/or organic peroxides were detected by a spectrofluorophotometric method using a Shimadzu spectrofluorophotometer RF-540 connected to a Data Recorder Dr-3. In presence of horseradish peroxidase, H_2O_2 or $-\text{OOH}$ reacts with p-hydroxyphenylacetic acid to yield a detectable fluorescent product ($\lambda_{\text{ex}} = 315 \text{ nm}$, $\lambda_{\text{em}} = 406 \text{ nm}$).[112]



2.7. Ferrioxalate actinometry

The photon flux has been determined using a chemical ferrioxalate actinometer.[113, 114] Briefly, freshly prepared 25 ml iron(III) sulphate aqueous solution (11.25 mmol) and 40 ml potassium oxalate aqueous solution (33.75 mmol) have been mixed in the reactor used for the photocatalytic H₂ production test (see Figure 2.2) in the dark. Afterwards, 10 ml H₂SO₄ aqueous solution (0.375 M) has been added to the reactor. The final volume of the solution have been adjusted to 75 ml, the same as that used for the photocatalytic H₂ production tests. Under these conditions, the green colour of the ferrioxalate complex is formed.

The reactor has been irradiated from the outside using an Osram XBO 1000 W Xenon lamp in a Müller LAX 1000 lamp housing. An UG1 bandpass filter restricting the incident light to the wavelengths between 300 and 400 nm has been employed during the photon flux measurements. The ferrioxalate complex absorbs all photons of the incident light in this range and is reduced to iron(II) complex according to the following equation (Eq. 2.3):[115]



The rate of iron(II) ions formation has been calculated by determining the amount of iron(II) ions after different illumination times using a spectrophotometric method employing 1,10-phenanthroline reagent.[114] The photon flux has been calculated by dividing the rate of iron(II) ion formation by the quantum yield of the iron(II) ion formation at the applied conditions (quantum yield = 1.15 [115]).

3. Results

3.1. Synthesis, modification, and characterization of TiO₂ nanomaterials

3.1.1. TiO₂ anatase nanoparticles

TiO₂ anatase nanoparticles have been synthesized by the hydrothermal treatment of commercially available TiO₂ P25 in highly alkaline solution (10 M NaOH) as described in the experimental section (section 2.2.1). The XRD diffraction patterns of the as-synthesized powder as well as that of the starting material (TiO₂ P25) are shown in Figure 3.1a and b, respectively. A comparison of both XRD diffraction patterns clearly indicates that there is a phase transformation from the anatase and the rutile phases to the titanate (H₂Ti₄O₉·H₂O) structure following the hydrothermal treatment. Calcination of the latter at 400 °C for 2 h leads to the formation of the pure anatase phase as confirmed by the XRD measurement (cf. Figure 3.1c).[116] The BET surface area of the resulting anatase nanoparticles was determined using nitrogen absorption-desorption. The surface area values and the Rietveld analysis of the XRD patterns are given in Table 3.1. Interestingly, the BET surface area of the anatase nanoparticles (TiO₂ P25HT) is found to be 3.46 times larger than that of the starting material TiO₂ P25.

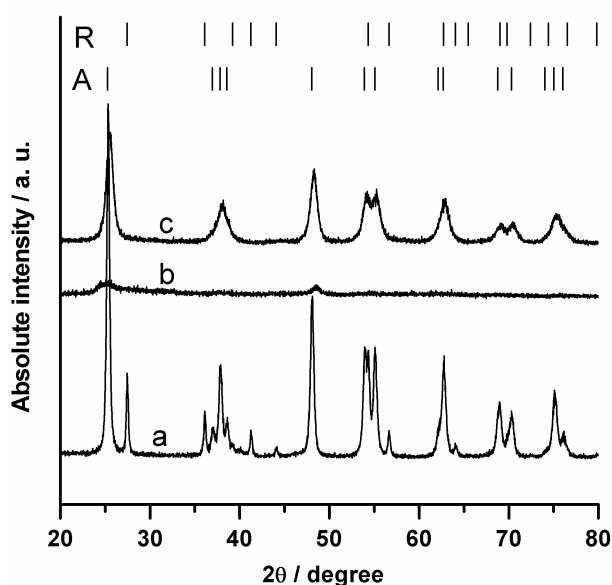
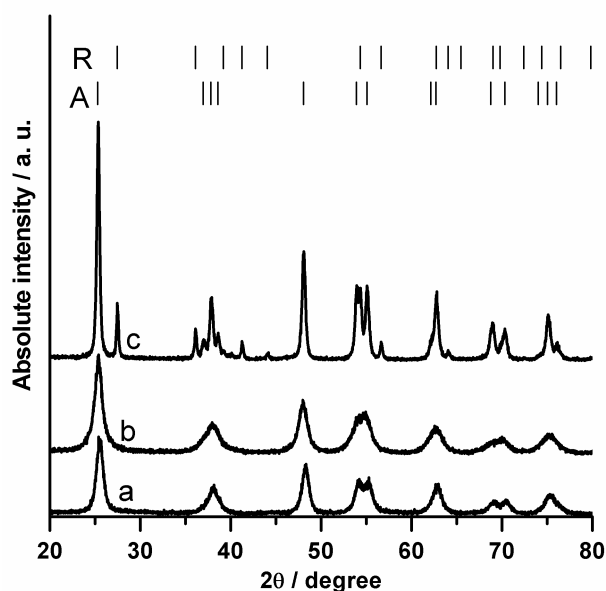


Figure 3.1. XRD diffraction patterns of (a) TiO₂ P25, (b) TiO₂ P25 after hydrothermal treatment without calcination (titanate), and (c) TiO₂ P25 after hydrothermal treatment and calcination at 400 °C for 2 h (TiO₂ P25HT). Labels A and R indicate Bragg positions for anatase and rutile, respectively.

Table 3.1. Quantitative phase composition, crystallite sizes, and BET surface area of bare and Pt-loaded TiO₂ nanomaterials.

Photocatalysts	Anatase (%)	Anatase crystallite size (nm)	Rutile (%)	Rutile crystallite size (nm)	BET surface area (m ² g ⁻¹)
TiO ₂ P25	82	31	18	49	52
Pt-loaded TiO ₂ P25	81	31	19	49	46
TiO ₂ P25HT	100	12	-	-	180
Pt-loaded TiO ₂ P25HT	100	12	-	-	169
TiO ₂ UV100	100	9	-	-	301
Pt-loaded TiO ₂ UV100	100	9	-	-	293

The anatase nanoparticles (TiO₂ P25HT) were modified with Pt via a photochemical deposition method (cf. section 2.3.1). Figure 3.2a shows the X-ray diffraction pattern of 0.5 wt% Pt-loaded TiO₂ P25HT. The obtained pattern was compared with those of 0.5 wt% Pt-loaded TiO₂ P25 and TiO₂ UV100, respectively. Clearly, all the diffraction peaks of TiO₂ P25HT and of TiO₂ UV100 can be indexed to the anatase phase (cf. Figure 3.2a and b, respectively), whereas the rutile phase only exists in case of TiO₂ P25 (cf. Figure 3.2c). No diffraction peaks are detected for Pt particles indicating that they are highly dispersed and very small particles.

**Figure 3.2.** XRD diffraction patterns of 0.5 wt% Pt-loaded TiO₂ nanomaterials, (a) TiO₂ P25HT, (b) TiO₂ UV100, and (c) TiO₂ P25. Labels A and R indicate Bragg positions for anatase and rutile, respectively.

The diffraction patterns were analyzed by the Rietveld method considering the whole pattern and not only single peaks. The quantitative phase composition and the crystallite sizes of nanocrystalline TiO_2 powders as evident from the Rietveld analysis of the XRD data are given in Table 3.1. The BET surface areas of the TiO_2 nanomaterials loaded with Pt or bare were determined using nitrogen absorption-desorption and are also given in Table 3.1. The results indicate that the BET surface area of TiO_2 P25HT, of TiO_2 P25, and of TiO_2 UV100 decreases following the Pt loading indicating that the Pt nanoparticles are deposited on the surface blocking some of the active sites for N_2 adsorption.

The morphologies of TiO_2 P25 before and after the hydrothermal treatment were investigated by field-emission scanning electron microscopy (FE-SEM). The obtained micrographs are shown in Figure 3.3. It is obvious from micrograph shown in Figure 3.3a that TiO_2 P25 has an average particle size of about 25 nm in good agreement with the crystallite size obtained from the XRD data analysis. The micrograph shown in Figure 3.3b also demonstrates that the hydrothermal treatment of TiO_2 P25 leads to the transformation from the spherical to a fiber like morphology. The subsequent calcination of this fiber like titanate material yields anatase nanoparticles exhibiting a rod like morphology. It seems that the fiber like particles are completely destroyed after the calcination step yielding small rod particles as confirmed by high-resolution transmission electron microscopy (HRTEM) (Figure 3.4). The particle size of TiO_2 P25HT is found to be about 10 nm in good agreement with the crystallite size obtained from the XRD data analysis. The interesting point is that the hydrothermal treatment of TiO_2 P25 and the post heat treatment yields anatase nanoparticles with an average particle size that is about two times smaller than that of the starting material (TiO_2 P25). Moreover, the surface area of TiO_2 P25HT is 3.46 times larger than that of TiO_2 P25 (see Table 3.1).

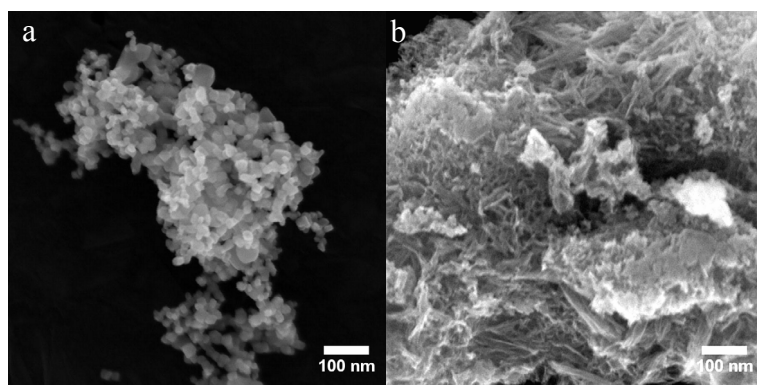


Figure 3.3. FE-SEM micrographs of TiO_2 P25 (a) before and (b) after hydrothermal treatment.

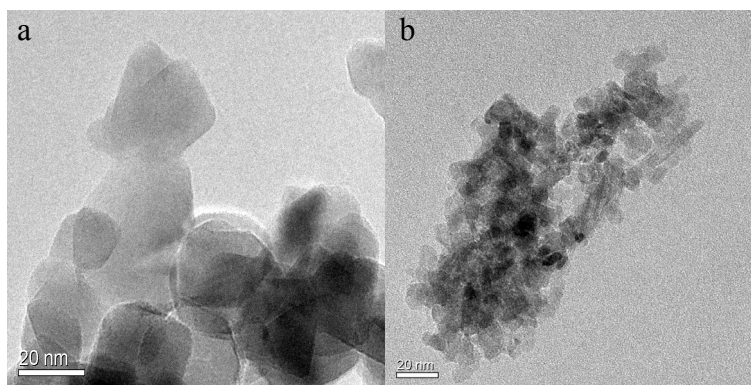


Figure 3.4. HR-TEM micrographs: (a) TiO₂ P25 and (b) TiO₂ P25HT.

3.1.2. TiO₂-polypyrrole nanocomposites

It is well known that precious metals nanoparticles, e.g., Pt as a co-catalyst, are essential for the photocatalytic H₂ evolution over TiO₂ from aqueous alcohol solution. Besides Pt, reports have also shown that TiO₂ surfaces modified with electron conducting polymers such as nafion and polypyrrole exhibit enhanced photocatalytic activity for the degradation of organic compounds [91, 92, 96, 97] as well as for the production of molecular hydrogen.[93] Therefore, the in situ simultaneous modification of TiO₂ with Pt-polypyrrole nanocomposites was investigated.

To optimize the ratio of Pt and polypyrrole, two series of TiO₂ P25 powders loaded with different Pt and polypyrrole ratios have been prepared. In the first series, the ratio of polypyrrole to TiO₂ was varied from 0.5 to 5.0 wt% and the loading with Pt was kept constant at 0.5 wt%. In the second series, the ratio of Pt to TiO₂ was varied from 0.1 to 2.0 wt% while the polypyrrole content was kept constant at 1.0 wt%. The as-prepared TiO₂ powders modified with Pt-polypyrrole nanocomposites were characterized using X-ray photoelectron spectroscopy (XPS), dark-field scanning transmission electron microscopy (DF-STEM), infrared spectroscopy (IR), and by the determination of the BET surface area. Figure 3.5 shows a typical XPS spectrum within the 0 to 1000 eV binding energy range, while the inset shows the XPS spectrum within the 66 to 88 eV binding energy range. The Pt 4f_{7/2} and 4f_{5/2} peaks are present at 71.4 and 74.5 eV, respectively, as shown from the inset indicating the formation of Pt(0).[117] The binding energies of the Pt 4f_{7/2} and 4f_{5/2} peaks are shifted to higher values as compared with neat Pt(0), indicating that there is a certain interaction between the Pt nanoparticles and polypyrrole.[118]

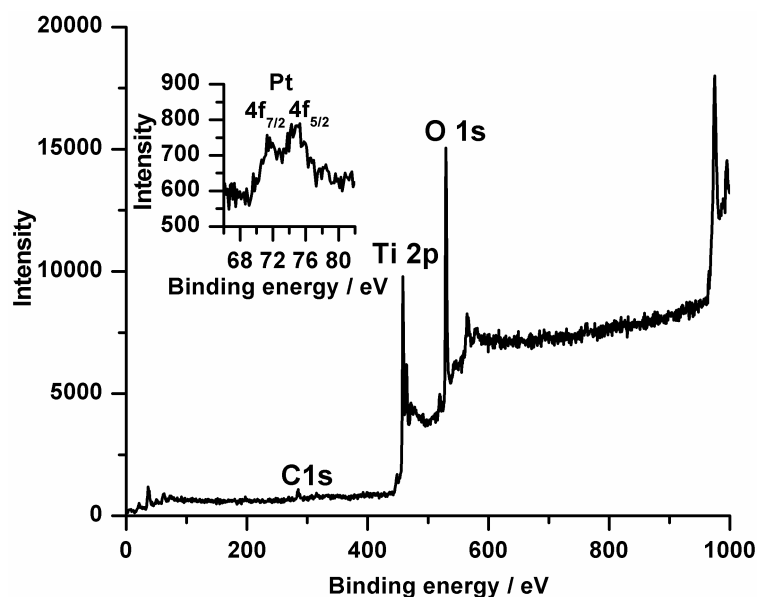


Figure 3.5. XPS spectra of TiO₂ modified with Pt-polypyrrole nanocomposites (1.0 wt% Pt and 1.0 wt% polypyrrole). The inset shows the Pt 4f peaks.

The DF-STEM measurement (Figure 3.6) indicates the formation of Pt islands with diameters of approximately 1.0 nm. In fact, the Pt nanoparticles were hardly detected indicating that the utilized method yields very small particles indeed. In order to identify the polypyrrole in the modified TiO₂, IR spectra of the powders were recorded (Figure 3.7). As shown in Figure 3.7a, TiO₂ modified with Pt-polypyrrole nanocomposites exhibits two peaks at 1152 and 1210 cm⁻¹. The characteristic bipolaron peak at 1210 cm⁻¹ indicates the formation of polypyrrole or at least of pyrrole oligomers in the oxidized state.[119, 120] However, the other characteristic bipolaron peak located at 925 cm⁻¹ is not observed most likely as a consequence of the strong background absorption of TiO₂ in this region. The IR spectra of the modified powders were compared with the IR spectra of pyrrole monomers, of Pt-loaded TiO₂ and of Pt-polypyrrole nanocomposites prepared in the absence of TiO₂ (b, c, and d in Figure 3.7). These spectra clearly indicate the formation of polypyrrole. The BET surface area of the TiO₂ modified Pt-polypyrrole composites (0.5 and 1.0 wt% Pt and polypyrrole, respectively) and Pt-loaded TiO₂ were calculated from nitrogen adsorption measurements to be 54 and 47 m² g⁻¹, respectively.

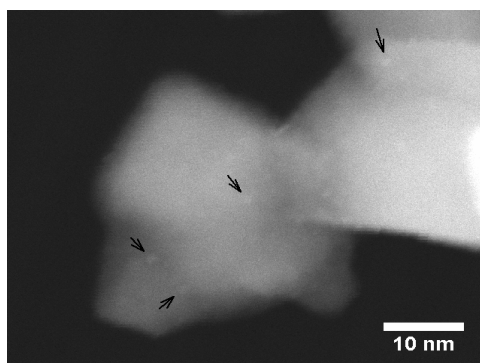


Figure 3.6. DF-STEM image of TiO₂ modified with 0.5 wt% Pt and 1.0 wt% polypyrrole nanocomposites. Pt is seen as bright points with diameter of about 1.0 nm (see arrows).

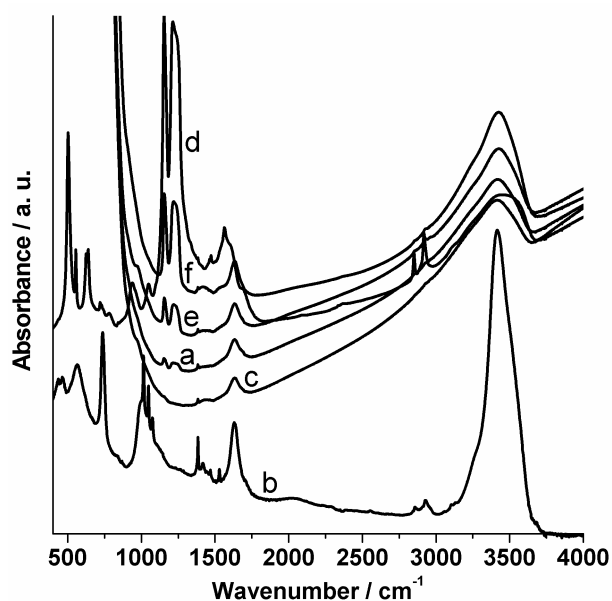


Figure 3.7. IR spectra of (a) TiO₂ modified with Pt-polypyrrole nanocomposites as prepared, (b) pyrrole monomers, (c) Pt-loaded TiO₂ prepared by a photochemical deposition method, (d) Pt-polypyrrole nanocomposites, (e) and (f) TiO₂ modified with Pt-polypyrrole nanocomposites following 20 and 100 h of illumination, respectively.

3.1.3. TiO₂ rutile nanorods

TiO₂ rutile nanorods either embedded in or decorated with anatase nanoparticles or in their pure form have been prepared by the thermal hydrolysis of aqueous solutions of the TALH complex at 200 °C for different reaction times (see section 2.2.2). Figure 3.8 shows the XRD patterns of the isolated powders obtained after 24, 48, 72, and 96 h of the thermal hydrolysis. Clearly, all the diffraction patterns can be indexed to the anatase and the rutile phases, respectively. With increasing reaction time, the peaks assigned to the anatase phase completely disappear and pure rutile is found after 72 h and 96 h of hydrothermal treatment (see Figure 3.8c and d). The quantitative phase composition and the crystallite sizes of the

nanocrystalline TiO₂ powders as evident from the Rietveld analysis of the XRD data are given in Table 3.2. The BET surface area, the pH measured at the end of the synthesis, and the yield are also summarized in Table 3.2. The yield has been calculated relative to the expected yield upon complete thermal hydrolysis of the TALH complex regardless of the possible losses resulting from the washing process.

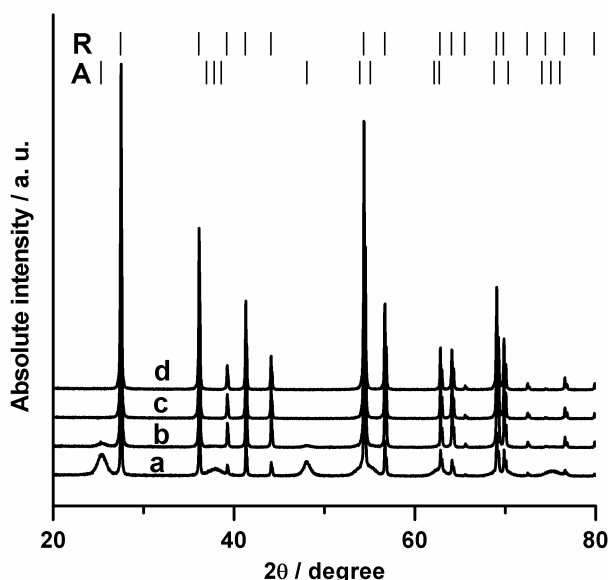


Figure 3.8. XRD patterns of as-synthesized nanocrystalline TiO₂ powders obtained by thermal hydrolysis of aqueous solutions of the TALH precursor at 200 °C for (a) 24 h, (b) 48 h, (c) 72 h, and (h) 96 h. Labels R and A indicate Bragg positions for rutile and anatase, respectively.

Table 3.2. Quantitative phase composition, crystallite sizes, BET surface area, and yield of nanocrystalline TiO₂ prepared by thermal hydrolysis of the TALH precursor at 200 °C and the pH at the end of the experimental run.

Reaction time (h)	Anatase (%)	Anatase crystallite size (nm)	Rutile (%)	Rutile crystallite size (nm)	BET surface area (m ² g ⁻¹)	Yield (%)	Final pH
24	53	10	47	118	92	100 ^a	5.0
48	9	11	91	147	16	90	5.3
72	0	0	100	147	6	96	5.5
96	0	0	100	152	6	96	6.0

^ayield calculated depending on the isolated powder without further washing cycles

The morphology of the isolated powders has been investigated by field-emission scanning electron microscopy (FE-SEM). The micrographs of the TiO₂ powders obtained by thermal hydrolysis of aqueous solutions of TALH at 200 °C for 24 h (RA24) and for 48 h (RA48) indicate the formation of rod-like particles either embedded in or decorated with small nanoparticles as shown in Figure 3.9a and b, respectively. Upon further increase of the reaction time to 72 and 96 h only the rod-like particles are obtained as shown in Figure 3.9c and d (denoted as R72 and R96, respectively). At this point, it should be emphasized that the small nanoparticles adhere strongly to the surface of the rod-like nanoparticles as they can not even be removed by sonication and several washing cycles. Depending on the crystallite size obtained from XRD analysis and the particle morphology observed in the SEM micrographs it can be concluded that the small nanoparticles should be anatase whereas the nanorods should be rutile. However, by definition, the crystallite size calculated from XRD analysis does not necessarily match the particle size as seen by SEM.

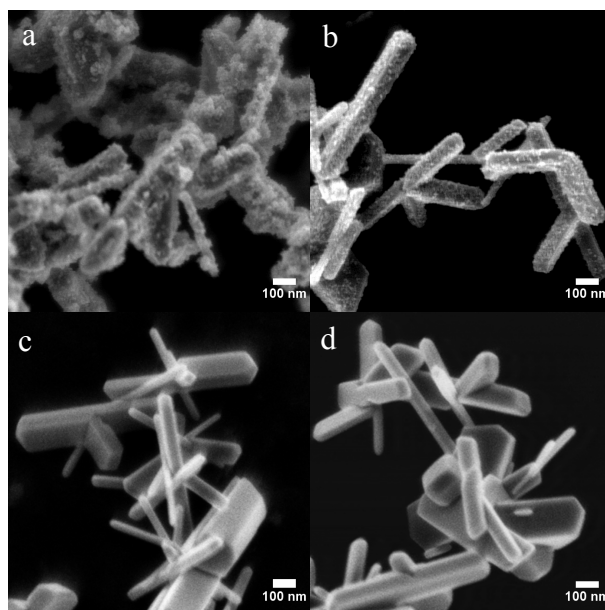


Figure 3.9. FE-SEM micrographs of as-synthesized nanocrystalline TiO₂ powders obtained by thermal hydrolysis of aqueous solutions of the TALH precursor at 200 °C for (a) 24 h, (b) 48 h, (c) 72 h, and (d) 96 h.

The high resolution TEM micrographs of the powder obtained after 48 h of hydrothermal treatment are shown in Figure 3.10. It is obvious from Figure 3.10b that the surfaces of the rutile nanorods are decorated by smaller equiaxial particles of 3-5 nm in diameter. In Figure 3.8c some of the smaller particles appear by bright contrast due to strong diffraction of electrons into the 15 mrad opening of the dark-field aperture. Thus, the crystalline nature of the smaller TiO_2 nanoparticles is proved. The rutile nanorods are elongated along their c-axis and show microfacets of the (1-11), (1-12), and (001) type at their tips as illustrated by the lines in the high-resolution micrograph shown in Figure 3.11b and the inset in Figure 3.11a. The high-resolution TEM micrograph given in Figure 3.11c shows the rutile lattice along the [001] zone axis. The corresponding Fourier transform (Figure 3.11d) confirms the orientation of the rutile rod. Hence, the rutile particles have grown into rods along the c-axis [001] direction and exhibit primarily (110) type facets. A schematic sketch of the rutile rod shape is given in Figure 3.11e. The SEM and TEM micrographs show that the diameter of the rutile rods varies from 50 to 100 nm and the length from 500 to 700 nm (Figures 3.9 and 3.10). Rutile nanorods of the same shape and with microfacets at their tips have been previously observed in some commercial TiO_2 powders;[121] however, with a much smaller size. A particular different situation is, on the other hand, given here by the decoration of the surface of the rutile nanorods by very small equiaxial TiO_2 nanoparticles.

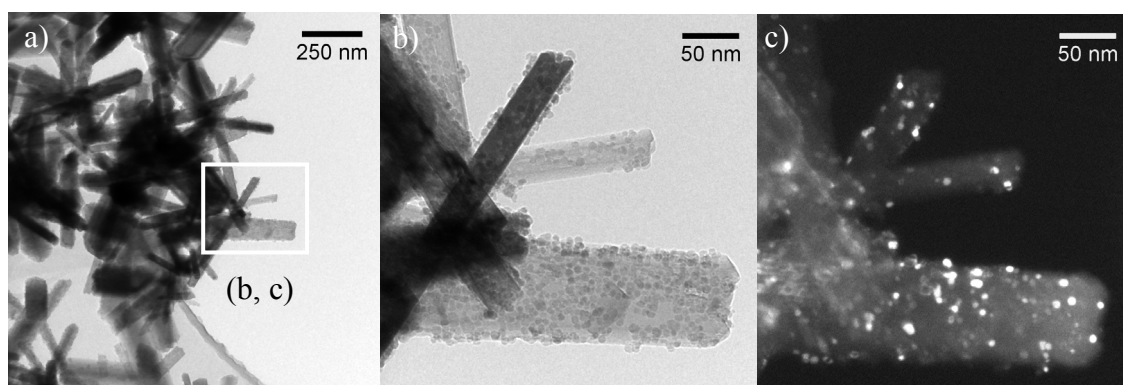


Figure 3.10. High-resolution transmission electron micrographs of as-synthesized nanocrystalline TiO_2 powder obtained by thermal hydrolysis of aqueous solutions of the TALH precursor for 48 h (a) TEM bright-field low magnification, (b) TEM bright-field high magnification, and (c) TEM dark-field.

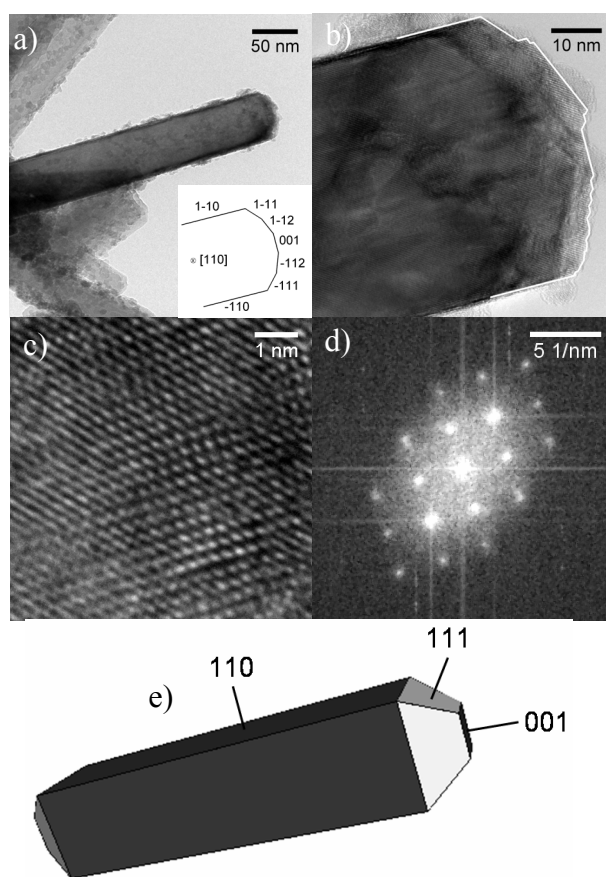


Figure 3.11. Shape analysis of as-synthesized nanocrystalline TiO_2 powder obtained by thermal hydrolysis of aqueous solutions of the TALH precursor for 48 h (a) TEM bright-field micrograph, (b, c) high-resolution TEM micrographs, (d) Fourier transform of c, and (e) sketch of the shape.

The optical properties of the newly prepared rutile TiO_2 powders either decorated with anatase nanoparticles or pure were determined using UV-Vis diffuse reflectance spectroscopy as shown in Figure 3.12A. It is clear from the onset of the absorbance (the Kubelka-Munk function $F(R)$ is equivalent to absorbance) in Figure 3.12A that the presence of anatase nanoparticles does not affect the optical properties of the rutile nanorods. Since TiO_2 has an indirect electronic transition at the onset of the absorption, the bandgap energy was determined by plotting the modified Kubelka-Munk function $[F(R)E]^{1/2}$ vs. the energy of the exciting light E as shown in Figure 3.12B.[103] The intercept of the linear fit with the x-axis yields a bandgap energy of 3.0 eV for all materials in good agreement with the value usually quoted for rutile TiO_2 .[122]

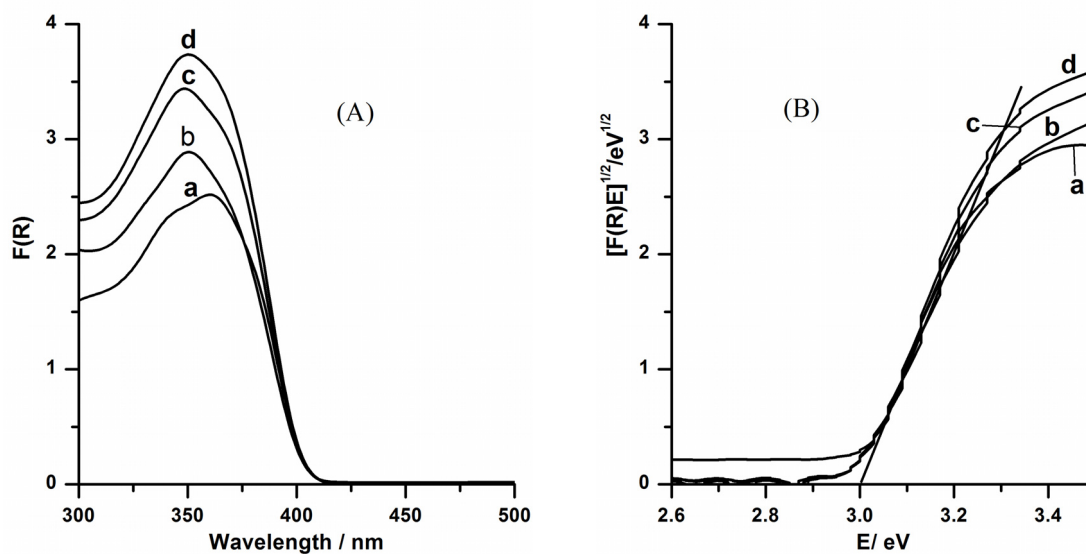


Figure 3.12. (A) Diffuse reflectance spectra of as-synthesized nanocrystalline TiO_2 powders obtained by thermal hydrolysis of aqueous solutions of the TALH precursor at 200°C for (a) 24 h, (b) 48 h, (c) 72 h, and (d) 96 h. (B) Plot of the modified Kubelka-Munk function versus the energy of light absorbed.

3.1.4. TiO_2 anatase nanoparticles, anatase/brookite mixtures, and brookite nanorods

In the previous section, it was shown that the thermal hydrolysis of aqueous solutions of the TALH complex at 200°C without any additives yields rutile nanorods either decorated with anatase nanoparticles or, at longer reaction times, completely free of anatase. The composition as well as the crystal structure of the TiO_2 nanoparticles prepared from TALH can be entirely changed by the presence of urea, as will be shown here. Interestingly, in this part of the study, it was found that the thermal hydrolysis of the TALH complex at 160°C for 24 h in the presence of 0.1 M urea yields pure anatase nanoparticles; whereas with increasing concentration of urea up to 5.0 M, biphasial anatase/brookite mixtures are formed. At higher urea concentration (≥ 6.0 M), high quality brookite is obtained as proven by XRD measurements (cf. Figure 3.13). The existence of brookite in the resultant powders is readily discernible from its (121) diffraction located at 30.81° (2θ) in the XRD pattern, where no overlapping of this peak with any peak from anatase or rutile occurs. To claim phase pure brookite, however, attention should be paid to the reflections in which overlapping with anatase reflections can occur. This is especially important for the (101) reflection of anatase and the (120) reflection of brookite. The diffraction data were analysed by the Rietveld method considering the whole pattern and not only single peaks. Thus, a higher sensitivity for low phase contents is possible even when peak broadening due to small crystallite sizes occurs. The Rietveld analysis proves that no anatase is present in the powders synthesized via

this new procedure employing 6.0 and 7.0 M urea, respectively, in the synthesis step. The quantitative phase composition and crystallite sizes of the nanocrystalline TiO_2 powders as evident from the Rietveld analysis of the XRD data are given in Table 3.3.

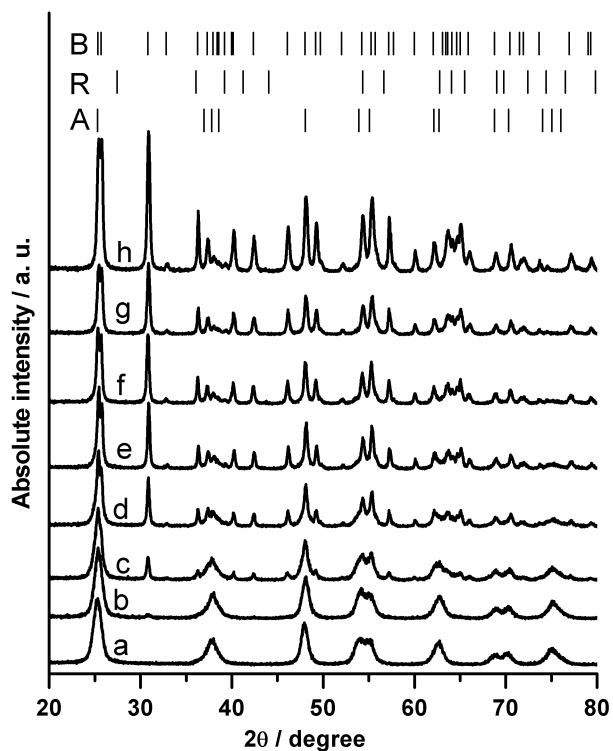


Figure 3.13. XRD patterns of as-synthesized nanocrystalline TiO_2 powders obtained by thermal hydrolysis of aqueous solutions of the TALH precursor at 160°C for 24 h in the presence of different concentrations of urea, (a) 0.1 M, (b) 0.5 M, (c) 1.0 M, (d) 1.5 M, (e) 2.0 M (f) 3.0 M, (g) 4.0 M, and (h) 6.0 M. Labels B, R, and A indicate Bragg positions for brookite, rutile, and anatase, respectively.

Table 3.3. Quantitative phase composition and crystallite sizes of nanocrystalline TiO₂ prepared by thermal hydrolysis of the TALH precursor at 160 °C for 24 h in the presence of different concentrations of urea.

Denotation	Urea (M)	Anatase (%)	Anatase crystallite size (nm)	Brookite (%)	Brookite crystallite size (nm)
A _{0.1,24}	0.1	100	11	0	-
AB _{0.5,24}	0.5	89	12	11	15
AB _{1.0,24}	1.0	72	11	28	40
AB _{1.5,24}	1.5	45	11	55	46
AB _{2.0,24}	2.0	23	12	77	49
AB _{3.0,24}	3.0	14	11	86	46
AB _{4.0,24}	4.0	7	11	93	36
AB _{5.0,24}	5.0	5	12	95	32
B _{6.0,24}	6.0	0	-	100	36
B _{7.0,24}	7.0	0	-	100	35

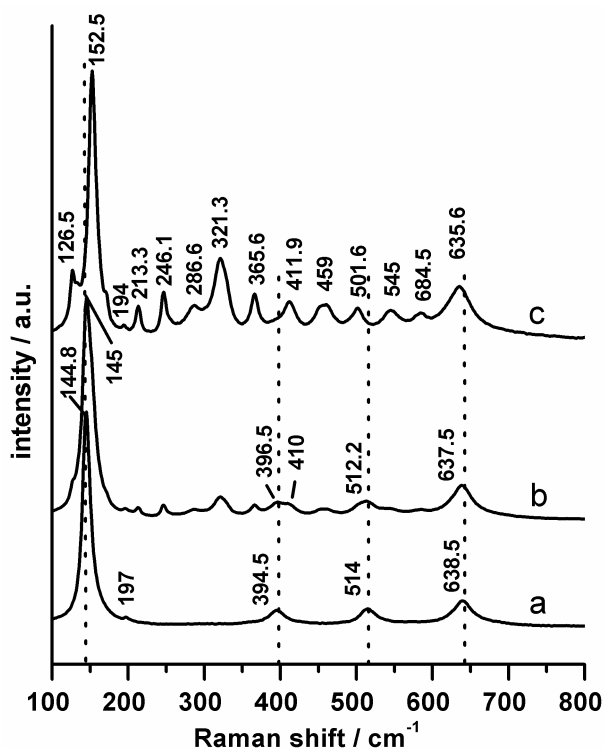


Figure 3.14. Raman spectra of as-synthesized nanocrystalline TiO₂ powders obtained by thermal hydrolysis of aqueous solutions of the TALH precursor at 160 °C for 24 h in the presence of different concentrations of urea, (a) 0.1 M, (b) 1.5 M, and (c) 6.0 M.

In agreement with the XRD results, the Raman spectra of the powders obtained at urea concentrations higher than 5.0 M show a rich scenario of signals, as commonly encountered for both, natural and artificial brookite (cf. Figure 3.14c), whereas the powder synthesized employing 0.1 M urea exhibits the characteristic peaks of anatase (cf. Figure 3.14a).[74, 123-125] The Raman spectrum of the powder synthesized employing 1.5 M urea (cf. Figure 3.14b), which consists of 45 % anatase and 55 % brookite, indicates that there is a shift in the peak positions whenever peaks of anatase and brookite are expected to appear close to one another, as a result of the overlap between the anatase and the brookite signals, whereas the other peaks that are only related to brookite appear almost at the same position.

To obtain information about the particles morphology, some selected powders were investigated by field-emission scanning electron microscopy (FE-SEM). The micrographs of the anatase TiO_2 powder obtained by thermal hydrolysis of the TALH precursor at 160°C for 24 h in the presence of 0.1 M of urea indicate that the pure anatase powder consists of aggregates from fine TiO_2 nanoparticles in the size range of 10 nm (as shown in Figure 3.15a) in good agreement with the particle size predicted from the XRD analysis. Figures 3.15b and c show the micrographs of two different biphasial anatase/brookite mixtures, (72 % anatase and 28% brookite) and (23 % anatase and 77 % brookite), respectively. Both micrographs indicate the formation of small nanoparticles in the size range of 10 nm and rod-like nanoparticles with diameters in the range of 25 nm. Figure 3.15d shows the micrograph of pure brookite obtained by the thermal hydrolysis of the TALH precursor at 160°C for 24 h in the presence of 6.0 M of urea, evincing that TiO_2 nanorods with diameters up to 25 nm and lengths up to 150 nm are formed. From the XRD crystallite size data and the SEM micrographs it could be concluded that the small nanoparticles crystallize in the anatase phase while the nanorods consist of brookite, however, by definition, the crystallite size derived from the XRD analysis does not necessarily match the particle size observed by SEM. The high resolution TEM micrograph shown in Figure 3.16 confirms this conclusion. Based upon spacing and angles of the lattice fringes, the rod-like particle with a diameter ca. 25 nm can be identified to be of brookite structure.[49] The nanorod is imaged along the $[-2-1]_{\text{B}}$ zone axis, and it is faceted by $(210)_{\text{B}} : 0.35\text{ nm}$, $(111)_{\text{B}} : 0.35\text{ nm}$, and $(-110)_{\text{B}} : 0.45\text{ nm}$. Also a small facet of $(012)_{\text{B}}$ occurs just above the tip. Based on the analysis of fast Fourier transforms of the image area, all these facets are drawn as contour lines into the experimental micrograph according to the indexing given in the inset. The longitudinal growth direction appears to be along $[001]_{\text{B}}$, which is the c-axis, and which is tilted by ca. 25° out of the image plane.

Adherent to the tip of the brookite nanorod there is a smaller particle, which is identified as anatase imaged along $[1-11]_A$. The anatase particle exhibits $(0-11)_A$ and $(10-1)_A$ planes, which share an angle of 98° and show spacings of 0.35 nm.

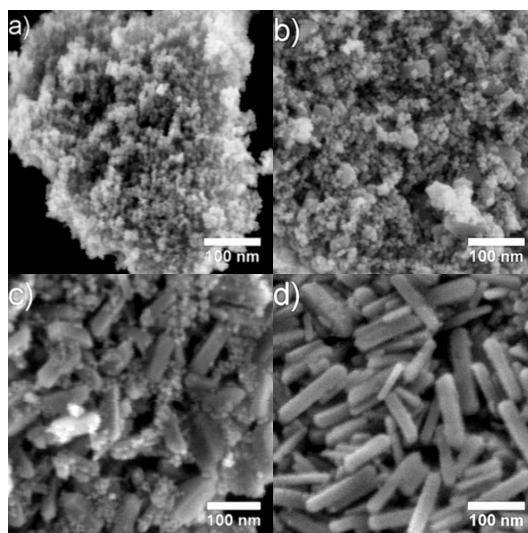


Figure 3.15. FE-SEM micrographs of as-synthesized nanocrystalline TiO_2 powders obtained by thermal hydrolysis of aqueous solutions of the TALH precursor at 160°C for 24 h in the presence of different concentrations of urea, (a) 0.1 M, (b) 1.0 M, (c) 2.0 M, and (d) 6.0 M.

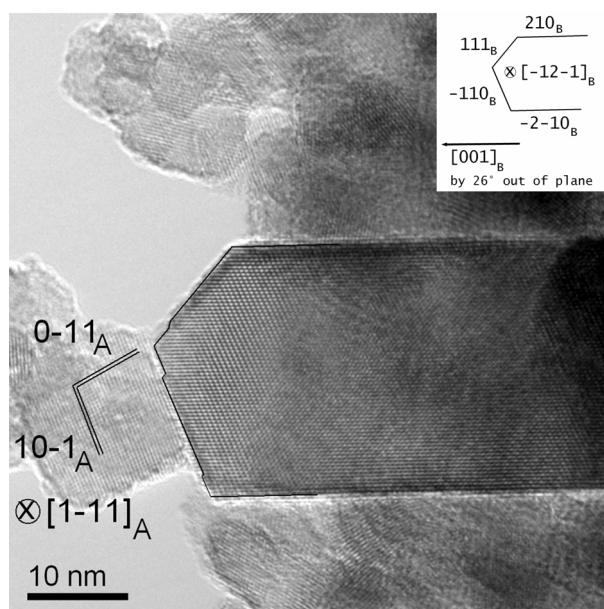


Figure 3.16. High-resolution transmission electron micrograph of as-synthesized nanocrystalline TiO_2 powder obtained by thermal hydrolysis of aqueous solutions of the TALH precursor at 160°C for 24 h in the presence of 1.0 M urea. The rod-like particle of ca. 25 nm in diameter is brookite imaged along the $[-12-1]_B$ zone axis (see inset). The smaller particle of ca. 15 nm in size is anatase imaged along $[1-11]_A$. The labels A and B refer to anatase and brookite, respectively.

3.2. Evaluation of the photocatalytic activities

3.2.1. Liquid phase reactions

3.2.1.1. Photocatalytic H₂ evolution from aqueous methanol solution over:

(a) Pt-loaded TiO₂ P25, TiO₂ UV100, and TiO₂ P25HT

The photocatalytic activities of H₂ evolution from aqueous methanol solution (0.03 M, 2.25 mmol methanol) over 0.5 wt% Pt-loaded TiO₂ nanomaterials, namely, TiO₂ P25 and TiO₂ UV100 which are commercially available, and TiO₂ P25HT, which has been prepared by the hydrothermal treatment of TiO₂ P25 (see section 2.2.1), have been investigated. The time courses of the photocatalytic H₂ evolution over these nanomaterials upon UV-Vis illumination are shown in Figure 3.17. It is obvious from Figure 3.17 that TiO₂ UV100 exhibits higher activity than TiO₂ P25 and even than TiO₂ P25HT. It is also obvious that bare TiO₂ nanomaterials without Pt loading do not exhibit photocatalytic H₂ evolution activity. No H₂ was evolved under dark condition as well as under illumination in the absence of the photocatalyst.

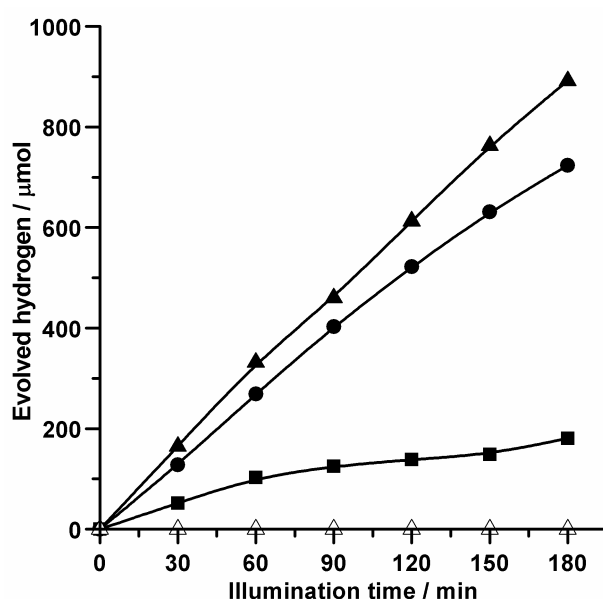


Figure 3.17. Time course of the photocatalytic H₂ evolution over different 0.5 wt% Pt-loaded TiO₂ nanomaterials (■) TiO₂ P25, (●) TiO₂ P25HT, and (▲) TiO₂ UV100 and over bare TiO₂ nanomaterials without Pt loadings (△) TiO₂ UV100 (shown as example). Conditions: 0.5 g l⁻¹ photocatalysts, 0.5 wt% Pt, 75 ml Ar-saturated aqueous methanol solution (0.03 M, 2.25 mmol methanol), UV(A)-Vis illumination (60 mW cm⁻²), temperature (25 °C), natural pH (pH ≈ 6.5).

The rate of the photocatalytic H₂ evolution from aqueous methanol solution is found to strongly depend on the methanol concentration initially present in the suspension (cf. Figure 3.18). It increases with increasing methanol concentration and then levels off to reach a plateau. Thus, a low methanol concentration (0.03 M, 2.25 mmol methanol) was employed during the photocatalytic experiment to avoid the high overpressure generated by the evolved H₂ at high methanol concentration allowing for longer reaction times since the reactor is sealed. These experimental conditions should also allow to investigate the possibility of water photooxidation in more detail. The photonic efficiency of the photocatalytic H₂ evolution was, however, calculated employing high methanol concentrations (4.93 M, 370 mmol methanol) in the plateau region in order to calculate the maximum efficiency. Figure 3.19 shows the time course of the photocatalytic H₂ evolution from 4.93 M aqueous methanol solution under UV(A) illumination. A bandpass filter restricting the incident light to wavelengths between 300 and 400 nm has been used during these measurements (cf. Figure 3.20). The photonic efficiencies of the different photocatalysts (ζ) were calculated by dividing the H₂ production rate by the photon flux, I_0 , which was determined under the same conditions using ferrioxalate actinometry.[113, 114]

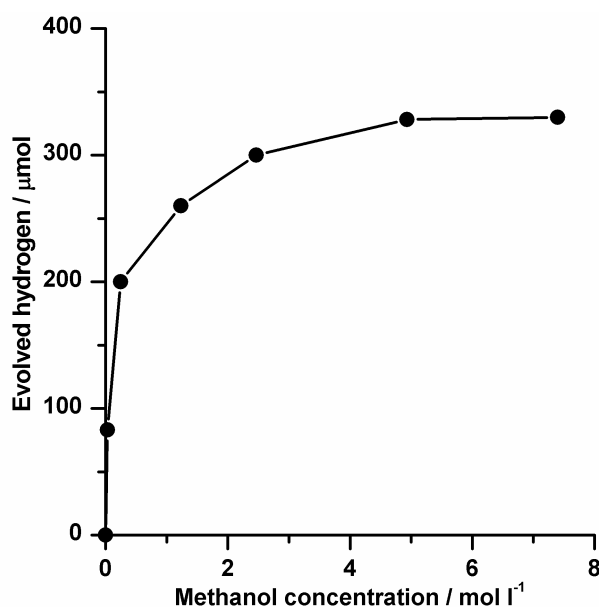


Figure 3.18. Effect of methanol concentration on the amount of H₂ evolved following 15 min of UV(A)-Vis illumination over Pt-loaded TiO₂ UV100. Conditions: 0.5 g l⁻¹ photocatalysts, 0.5 wt% Pt (photochemical deposition), 75 ml Ar-saturated aqueous methanol solutions, UV(A)-Vis illumination (60 mW cm⁻²), temperature (25 °C), natural pH (pH ≈ 6.5).

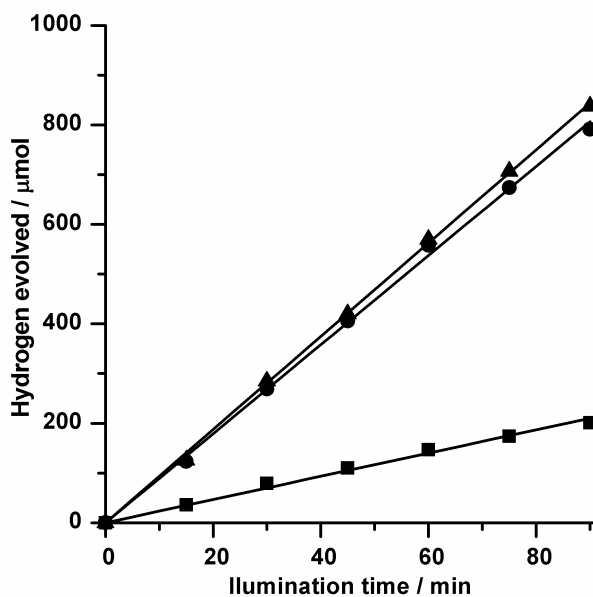


Figure 3.19. Time course of the photocatalytic H₂ evolution over different 0.5 wt% Pt-loaded TiO₂ nanomaterials (■) TiO₂ P25, (●) TiO₂ P25HT, and (▲) TiO₂ UV100. Conditions: 0.5 g l⁻¹ photocatalysts, 0.5 wt% Pt, 75 ml Ar-saturated aqueous methanol solution (4.93 M, 370 mmol methanol), UG1 black filter, UV(A) illumination (44.87 µeinstein min⁻¹), temperature (25 °C), natural pH (pH ≈ 6.5).

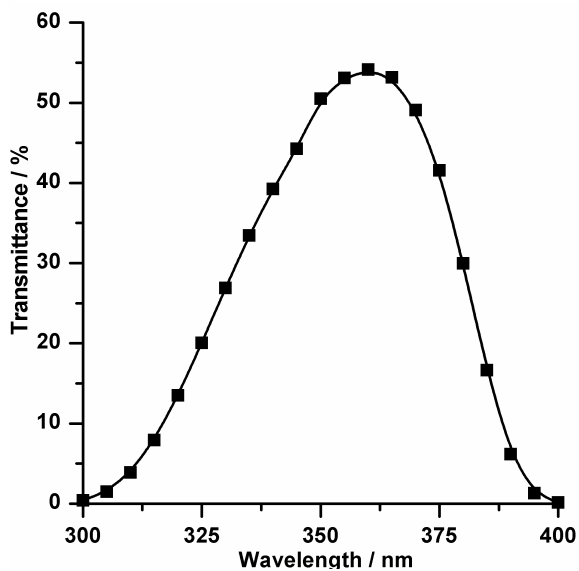


Figure 3.20. Transmittance spectrum of UG1 black filter.

In order to investigate the effect of the light intensity on the rates and on the photonic efficiencies of the photocatalytic H₂ evolution, the later were determined at different light intensities. The light intensity was adjusted employing neutral density filters. The photon flux was determined under the same conditions using ferrioxalate actinometry. The light intensities and the photon flux values are summarized in Table 3.4. Figures 3.21a and b show plots of the rates and the photonic efficiencies values obtained as a function of the applied light flux, respectively. As shown in Figure 3.21a, a non-linear relation between the rates of H₂ evolution and the employed light flux was observed. A non-linear relation between the light intensities and the photonic efficiencies is also observed (cf. Figure 3.21b). The most interesting observation is that TiO₂ UV100 and TiO₂ P25HT, which both of them consist of a pure phase anatase, exhibit the same behavior. They show a slight deviation from the linear dependence between the rates of the H₂ evolution and the light intensities at high light intensity values. While in case of TiO₂ P25, which is a mixture of rutile and anatase nanoparticles, the rate of photocatalytic H₂ evolution increases with increasing the light intensity then it reaches plateau and remains almost constant.

Table 3.4. Light intensities and photon flux values measured by UV-meter and ferrioxalate actinometry, respectively. Conditions: UG1 black filter, neutral density filters, 75 ml aqueous potassium ferrioxalate complex solution (0.15 M) in 0.05 M H₂SO₄.

Neutral density filter (optical density, OD)	UV(A) light intensity (mW cm ⁻²)	Wavelength range (nm)	Photon flux (μeinstein min ⁻¹)
-	25	300-400	44.87
OD 0.3	12	300-400	22.41
OD 0.6	6	300-400	10.65
OD 1.0	2.5	300-400	4.40

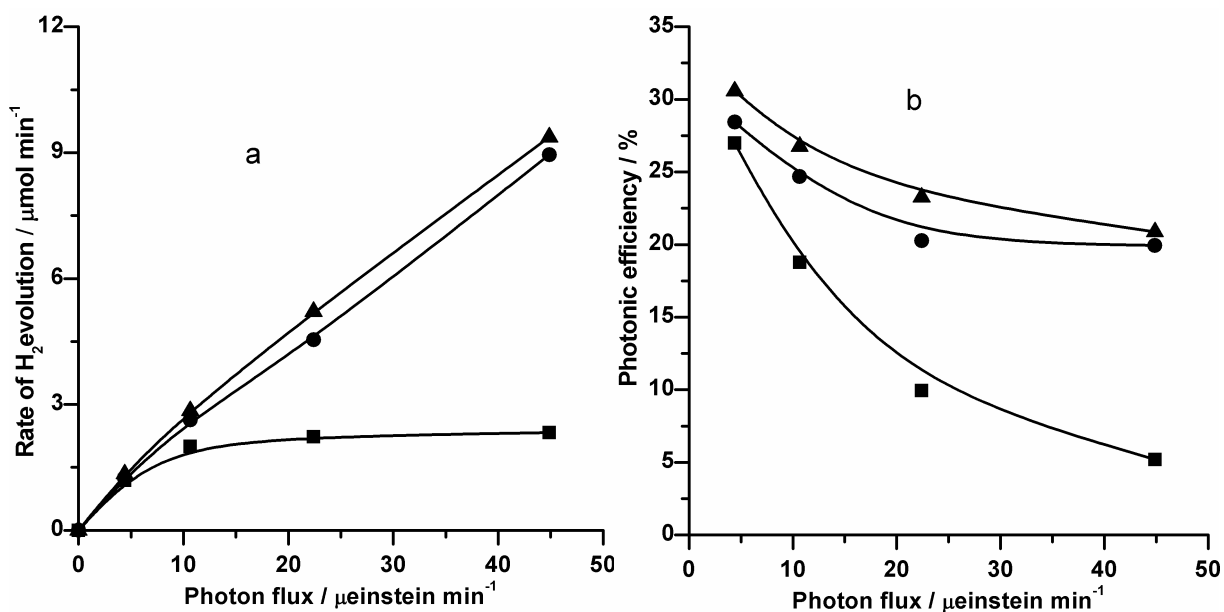


Figure 3.21. Effect of the light intensity on (a) the rate and on (b) the photonic efficiency of the photocatalytic H_2 evolution over different 0.5 wt% Pt-loaded TiO_2 nanomaterials (■) TiO_2 P25, (●) TiO_2 P25HT, and (▲) TiO_2 UV100. Conditions: 0.5 g l^{-1} photocatalysts, 0.5 wt% Pt, 75 ml Ar-saturated aqueous methanol solution (370 mmol methanol), UG1 black filter, UV(A) illumination (up to $\approx 45 \mu\text{einstein min}^{-1}$), temperature (25°C), natural pH (pH ≈ 6.5).

The balance between the amount of methanol photooxidation products and the amount of H_2 gas evolved has been tested. The products were qualitatively and quantitatively analyzed following different illumination times and working at different pH values employing different methanol concentrations. In all experimental runs, formaldehyde, formic acid and carbon dioxide were the only detected reaction products. The results of the analysis are listed in Table 3.5. The results indicate that after 3 h of UV-Vis illumination of aqueous methanol solutions (0.03 M, $2250 \mu\text{mol}$ methanol) at different pH values (3.0, 7.0, and 10) in the presence of Pt-loaded TiO_2 UV100, the amount of H_2 evolved is almost twice as high as the expected value calculated from the sum of the methanol photooxidation products (formaldehyde, formic acid, and carbon dioxide). To examine only the initial photooxidation of methanol, the experiments were repeated at shorter UV-Vis illumination times (15 min) working a gain at different pH values (3.0 and 7.0). Under these conditions, only formaldehyde was detected and its amount was found to be equimolar to the amount of H_2 evolved. The same results were obtained when the photooxidation products were measured at high methanol concentration (4.93 M , $3.7 \times 10^5 \mu\text{mol}$ methanol, see Table 3.5).

Table 3.5. Quantitative analysis of methanol photocatalytic oxidation products over 0.5 wt% Pt-loaded TiO₂ UV100 at different reaction times, pH values, and methanol concentrations.

Detected products (μmol)	Conditions: 2250 μmol methanol, 3 h UV(A)-Vis illumination,			Conditions: 2250 μmol methanol, 15 min UV(A)- Vis illumination,	
	<u>pH</u>			<u>pH</u>	
	3.0	7.0	10.0	3.0	7.0
Molecular hydrogen	899	1118	946	62	80
Formaldehyde	285	323	283	59	75
Formic acid	7.54	7.84	25	--	--
Carbon dioxide	56	82	58	--	--
Expected molecular hydrogen	468	585	507	59	75
Detected products (μmol)	Conditions: 3.7×10^5 μmol methanol, 15 min UV(A)-Vis illumination,				
	<u>pH</u>				
	3.0				7.0
Molecular hydrogen	260				290
Formaldehyde	286				323
Formic acid	--				--
Carbon dioxide	--				--
Expected molecular hydrogen	286				323

(b) TiO₂ P25 modified with Pt-polypyrrole nanocomposites

In this part of the work, the photocatalytic activity of TiO₂ nanoparticles loaded with both, Pt islands as well as a polypyrrole coating have been investigated. To examine the effect of the TiO₂ surface loading with polypyrrole and Pt on the photocatalytic H₂ evolution, a set of photocatalytic experiments were performed employing aqueous methanol solution (0.03 M, 2.25 mmol methanol) under UV(A)-Vis illumination. Figure 3.22a shows the time course of the H₂ evolution at different loadings of polypyrrole and at a constant Pt content of 0.5 wt%. The amount of H₂ increases almost linearly as a function of the irradiation time without notable deactivation at any of the employed polypyrrole ratios. Figure 3.22b shows the amount of H₂ that was evolved following 5 h of illumination as a function of the polypyrrole loading at a constant Pt content of 0.5 wt%, i.e., data extracted from Figure 3.22a. It is obvious that the amount of H₂ evolved increases with increasing polypyrrole loading up to 1.0 wt%. At higher loadings of polypyrrole the amount of the evolved gas decreases slightly and subsequently remains constant as the loading is further increased. Figure 3.23a shows the time

course of the H₂ evolution at different Pt loadings. Figure 3.23b demonstrates the effect of Pt loading on the amount of H₂ evolved following 5 h of illumination at the optimized loading with polypyrrole (1.0 wt%, data extracted from Figure 3.23a). As can be seen from Figure 3.23, the amount of H₂ evolved increases with increasing Pt loading until at 0.5 wt% a maximum efficiency is reached. At higher Pt concentrations (0.75 wt% and more) the amount of gas being generated begins to drop off.

In order to test the stability of the polymer under extensive illumination, the photocatalytic test was carried out in four consecutive runs each lasting 5.0 h using the same suspension (Figure 3.24). The first run was performed without the addition of methanol and only a small amount of H₂ (37 μmol) was detected following 5 h of illumination. The headspace was flushed with Ar and the second run was carried out employing 0.03 M aqueous methanol solution (2.25 mmol methanol). As shown in Figure 3.24 (second run), the H₂ evolution rate is identical to that observed with the freshly modified powder and it remains comparable for the duration of the run. This indicates that the polypyrrole polymer is stable under the employed experimental conditions. At the end of the second run, the headspace was again flushed with Ar and the test was repeated for a third and subsequently a fourth run.

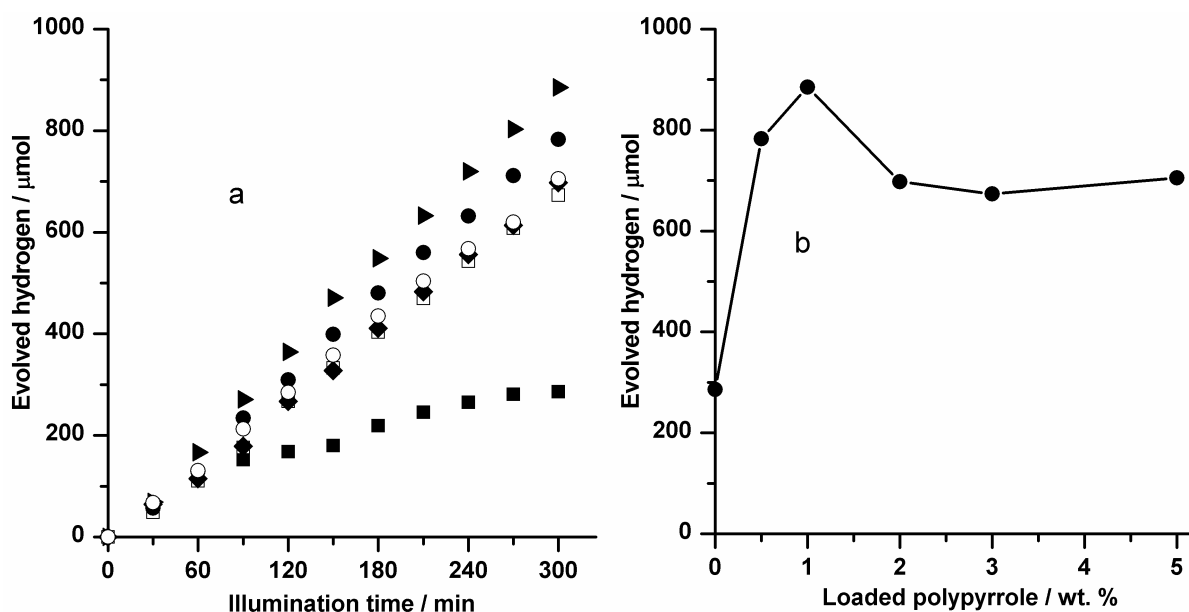


Figure 3.22. (a) Time course of the photocatalytic H₂ evolution as a function of the amount of polypyrrole loaded on TiO₂ P25 surface. (■) 0.0 (photodeposition method), (●) 0.5, (▲) 1.0, (◆) 2.0, (□) 3.0, (○) 5.0 wt% polypyrrole. (b) Effect of polypyrrole loading on the amount of H₂ evolved following 5 h of illumination. Conditions: 0.5 g l⁻¹ photocatalysts, 0.5 and 1.0 wt% Pt and polypyrrole, respectively, 75 ml Ar-saturated aqueous methanol solution (0.03 M, 2.25 mmol methanol), UV(A)-Vis illumination (60 mW cm⁻²), temperature (25 °C), natural pH (pH ≈ 6.5).

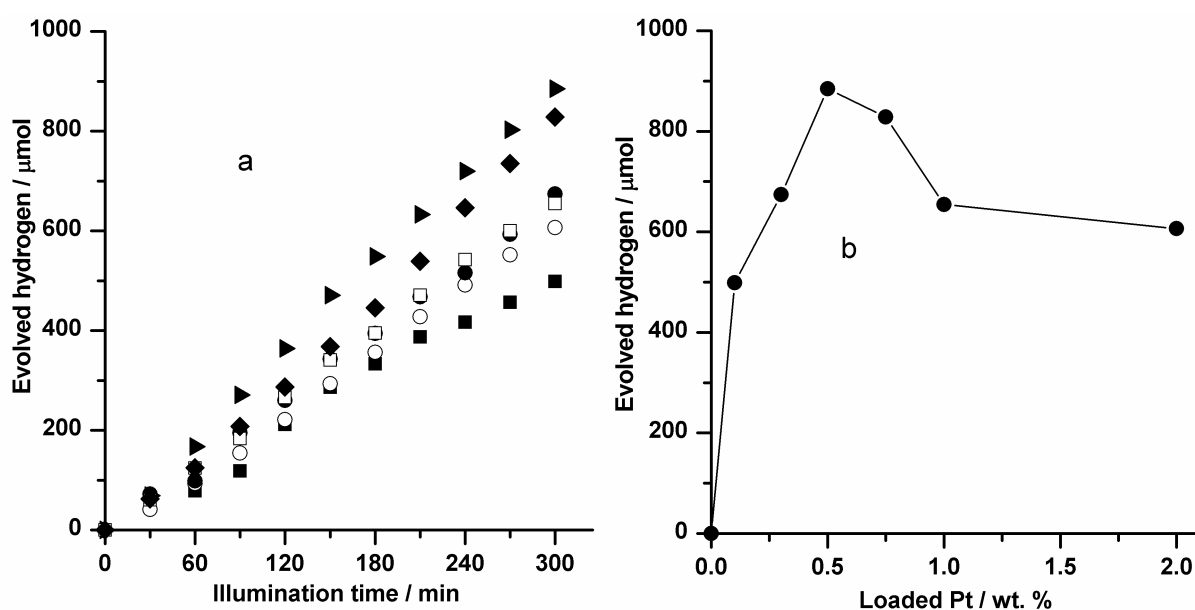


Figure 3.23. (a) Time course of the photocatalytic H₂ evolution as a function of the amount of Pt loaded on TiO₂ surface. (■) 0.1, (●) 0.3, (▶) 0.5, (◆) 0.75, (□) 1.0, (○) 2.0 wt% Pt. (b) Effect of Pt loading on the amount of H₂ evolved following 5 h of illumination. Conditions: 0.5 g l⁻¹ photocatalysts, 0.5 and 1.0 wt% Pt and polypyrrole, respectively, 75 ml Ar-saturated aqueous methanol solution (0.03 M, 2.25 mmol methanol), UV(A)-Vis illumination (60 mW cm⁻²), temperature (25 °C), natural pH (pH \approx 6.5).

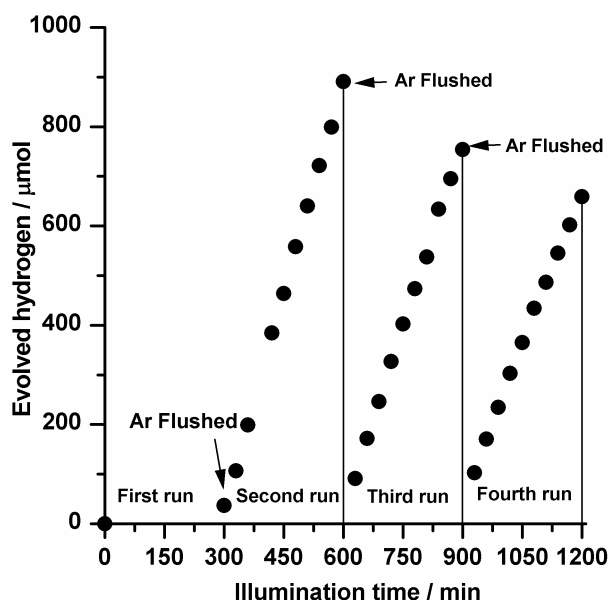


Figure 3.24. Effect of four consecutive runs on the photocatalytic H₂ production. Conditions: 0.5 g l⁻¹ photocatalysts, 0.5 and 1.0 wt% Pt and polypyrrole, respectively, 75 ml Ar-saturated aqueous methanol solution (0.03 M, 2.25 mmol methanol), UV(A)-Vis illumination (60 mW cm⁻²), temperature (25 °C), natural pH (pH \approx 6.5). First run without methanol addition.

Since the H₂ evolution rate strongly depends on the methanol concentration (see Figure 3.25), the decrease in the total amount of evolved H₂ gas observed in the experimental runs of Figure 3.24 can be explained by the consumption of some of the initially present methanol (after the first run 6.7 %, 5.5 % and 3.8 %, respectively, of the methanol initially present in the suspension were converted to formaldehyde, 1,2-ethanediol, and carbon dioxide, respectively). After the end of the fourth run, the IR spectrum of the photocatalyst powder was recorded following its separation from the water phase by centrifugation and drying *in vacuo*. As shown in Figure 3.7e, the powder exhibits the same peaks as the as-prepared TiO₂ powder modified with Pt-polypyrrole nanocomposites (Figure 3.7a). Moreover, no peaks were detected that could be attributed to the degradation products of polypyrrole. Also a long-term irradiation experiment employing the Pt-polypyrrole-TiO₂ photocatalyst (100 h) does not provide any indication for the degradation of the polypyrrole film as has been concluded from the IR spectrum given in Figure 3.7. The spectra shown in Figure 3.7e and f confirm the stability of the polypyrrole polymer under the present photocatalytic conditions. In fact, the bandgap irradiation of TiO₂ has been shown to even induce oxidative polymerization of pyrrole monomers.[95, 126]

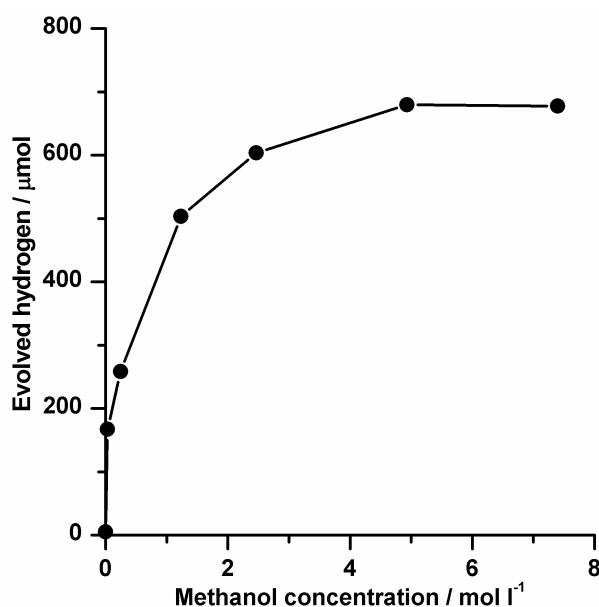


Figure 3.25. Effect of methanol concentration on the amount of H₂ evolved following 1 h of UV(A)-Vis illumination. Conditions: 0.5 g l⁻¹ photocatalysts, 0.5 and 1.0 wt% Pt and polypyrrole, respectively, 75 ml Ar-saturated aqueous methanol solutions, UV(A)-Vis illumination (60 mW cm⁻²), temperature (25 °C), natural pH (pH ≈ 6.5).

(c) Pt-loaded TiO₂ anatase nanoparticles, anatase/brookite mixtures, and brookite nanorods

The nanomaterials tested so far consist of either the pure anatase phase (TiO₂ UV100 and TiO₂ P25HT) or a mixture of the anatase and the rutile phases (TiO₂ P25). Following the successful syntheses of tailored anatase/brookite mixtures (cf. section 3.1.4), the photocatalytic activities of these tailored TiO₂ powders concerning the H₂ formation from aqueous methanol solutions have been tested. Figure 3.26 shows the time course of photocatalytic H₂ evolution over 0.5 wt% Pt-loaded anatase nanoparticles, anatase/brookite mixtures, and brookite nanorods from aqueous methanol solutions (0.03 M, 2.25 mmol methanol). Pt nanoparticles were loaded via the photochemical deposition method described above (cf. section 2.3.1). No H₂ was evolved in the absence of Pt islands as well as under dark condition and under illumination in the absence of the photocatalyst. It is obvious from Figure 3.26 that anatase/brookite mixtures and brookite nanorods exhibit photocatalytic activities higher than those of the pure anatase nanoparticles, which have been prepared employing the same experimental conditions (TiO₂A_{0.1,24}) as well as those of TiO₂ P25. Low methanol concentration (0.03 M, 2.25 mmol methanol) was employed during the photocatalytic experiment to avoid the high overpressure generated by evolved H₂ at high methanol concentration allowing longer reaction time since the reactor is sealed.

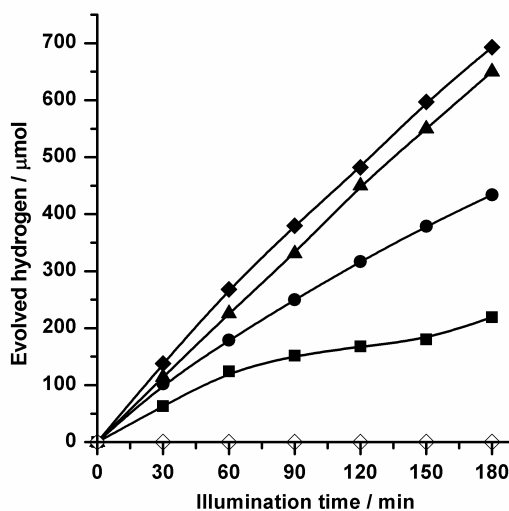


Figure 3.26. Time course of the photocatalytic H₂ evolution over 0.5 wt% Pt-loaded TiO₂ nanomaterials (■) TiO₂ P25, (●) TiO₂ anatase nanoparticles (TiO₂A_{0.1,24}), (◆) TiO₂ anatase/brookite mixture (TiO₂AB_{1.0,24}), and (▲) TiO₂ brookite nanorods (TiO₂B_{6.0,24}) and over bare TiO₂ nanomaterials without Pt loadings (◇) TiO₂ anatase/brookite mixture (TiO₂AB_{1.0,24}, shown as example). Conditions: 0.5 g l⁻¹ photocatalysts, 0.5 wt% Pt (photochemical deposition method), 75 ml Ar-saturated aqueous methanol solution (0.03 M, 2.25 mmol methanol), UV(A)-Vis illumination (60 mW cm⁻²), temperature (25 °C), natural pH (pH ≈ 6.5).

The rate of the photocatalytic H₂ evolution from aqueous methanol solution depends strongly on the methanol concentration initially present in the suspension. It increases with increasing the methanol concentration, and then it reaches a plateau (see for example Figure 3.25). Thus, the photonic efficiency of the photocatalytic H₂ evolution was calculated employing high methanol concentration (4.93 M, 370 mmol methanol) in the plateau region in order to calculate the maximum efficiency. The photonic efficiencies (ζ) of H₂ evolution have been calculated by dividing the rate of H₂ evolution from 4.93 M aqueous methanol solution by the photon flux ($\zeta = R / I_0$). The rate of H₂ evolution has been calculated from the slope of the time course of the H₂ production upon UV(A) illumination (as example sees Figure 3.27). The photon flux has been calculated by employing ferrioxalate actinometry [113, 114] performed under the same conditions as the rate of H₂ evolution measurements to eliminate any errors associated with the influence of light reflections and reactor geometry. The calculated rates and the photonic efficiency values as well as the BET surface areas of the investigated powders are given in Table 3.6. The anatase nanoparticles, anatase/brookite mixtures and brookite nanorods have also been loaded with Pt nanoparticles employing colloidal Pt suspension instead of Pt loading via the photochemical deposition method. These colloidal Pt suspensions have been prepared following the recipe given in section 2.3.3. They contained particles with an average diameter of 3.0 nm. These Pt suspensions have been used to avoid the probability of the change of the particle size of the Pt nanoparticles during the Pt loading to ensure that the difference in the photocatalytic activity can clearly be attributed to the properties of the tested TiO₂ powders. The photonic efficiencies (ζ) of H₂ production from 4.93 M aqueous methanol solution (370 mmol methanol) over anatase/brookite mixtures and brookite nanorods loaded with colloidal Pt have also been calculated by dividing the rate of H₂ evolution by the photon flux ($\zeta = R / I_0$). The rate of H₂ evolution has been calculated from the slope of the time course of the H₂ production upon UV(A) illumination (cf. Figure 3.28). The calculated rates and the photonic efficiency values as well as the BET surface areas of the investigated powders are given in Table 3.7. The results show that the photonic efficiency of the photocatalytic H₂ production increases as the content of the brookite phase in the investigated powders increases, followed by a slight decrease and subsequently a leveling off.

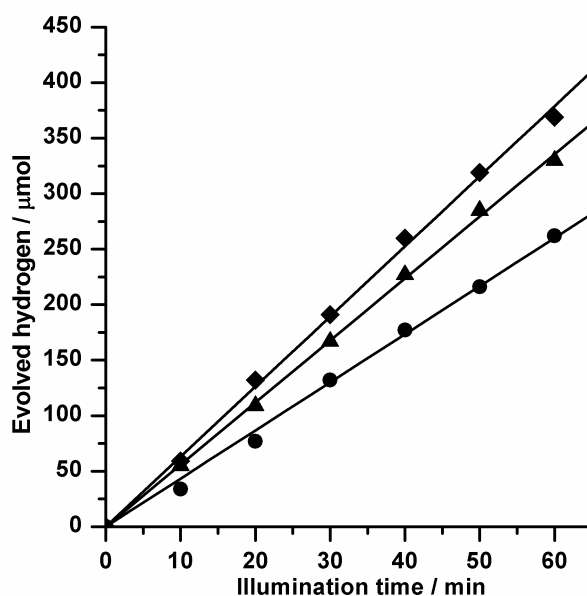


Figure 3.27. Time course of the photocatalytic H₂ evolution over Pt-loaded TiO₂ nanomaterials (●) TiO₂ anatase nanoparticles (TiO₂A_{0.1,24}), (◆) TiO₂ anatase/brookite mixture (TiO₂AB_{1.0,24}), and (▲) TiO₂ brookite nanorods (TiO₂B_{6.0,24}). Conditions: 0.5 g l⁻¹ photocatalysts, 0.5 wt% Pt (photochemical deposition method), 75 ml Ar-saturated aqueous methanol solution (4.93 M, 370 mmol methanol), UG1 black filter, UV(A) illumination (32.4 μeinstein min⁻¹), temperature (25 °C), natural pH (pH ≈ 6.5).

Table 3.6. Rates (R_{H₂}) and photonic efficiencies (ζ) of the photocatalytic H₂ evolution from aqueous methanol solutions (4.93 M, 370 mmol methanol) over Pt-loaded anatase nanoparticles, anatase/brookite mixtures, and brookite nanorods as well as the respective BET surface areas. Conditions: 0.5 wt% Pt (photochemical deposition method), photon flux I₀ = 1944 μeinstein h⁻¹.

Nanomaterials	Anatase (%)	Brookite (%)	R _{H₂} (μmol h ⁻¹)	ζ (%)	BET surface area (m ² g ⁻¹)
TiO ₂ A _{0.1,24}	100	-	260	13.4	154
TiO ₂ AB _{1.0,24}	72	28	378	19.4	114
TiO ₂ AB _{1.5,24}	45	55	336	17.2	85
TiO AB _{2.0,24}	23	77	335	17.2	68
TiO ₂ B _{6.0,24}	-	100	335	17.2	57

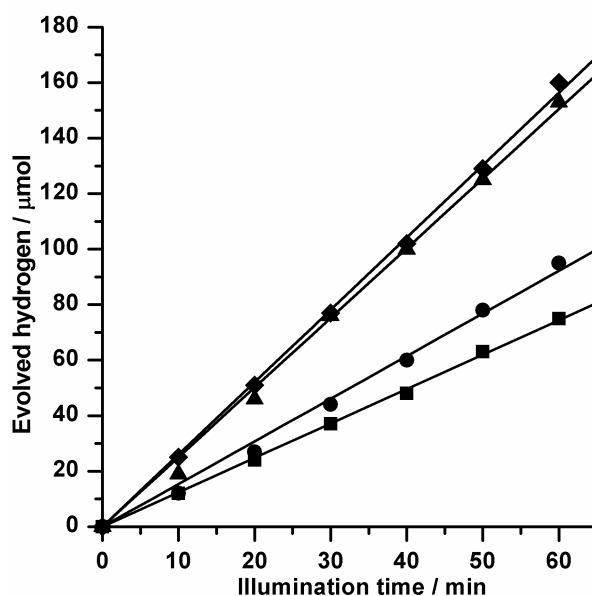


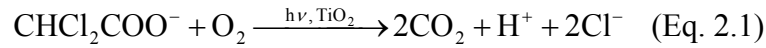
Figure 3.28. Time course of the photocatalytic H₂ evolution over Pt-loaded TiO₂ nanomaterials (●) TiO₂ anatase nanoparticles (TiO₂A_{0.1,24}), (◆) TiO₂ anatase/brookite mixture (TiO₂AB_{1.0,24}), (▲) TiO₂ brookite nanorods (TiO₂B_{6.0,24}), and (■) TiO₂ P25. Conditions: 0.5 g l⁻¹ photocatalysts, 0.5 wt% Pt (colloidal Pt suspensions), 75 ml Ar-saturated aqueous methanol solution (4.93 M, 370 mmol methanol), UG1 black filter, UV(A) illumination (21.66 μeinstein min⁻¹), temperature (25 °C), natural pH (pH ≈ 6.5).

Table 3.7. Rates (R_{H₂}) and photonic efficiencies (ζ) of the photocatalytic H₂ evolution from aqueous methanol solutions (4.93 M, 370 mmol methanol) over Pt-loaded anatase nanoparticles, anatase/brookite mixtures, and brookite nanorods as well as the respective BET surface areas. Conditions: 0.5 wt% Pt (colloidal Pt suspensions), photon flux I₀ = 1300 μeinstein h⁻¹.

Nanomaterials	Anatase (%)	Brookite (%)	R _{H₂} (μmol h ⁻¹)	ζ (%)	BET surface area (m ² g ⁻¹)
TiO ₂ A _{0.1,24}	100	-	91	7.0	154
TiO ₂ AB _{1.0,24}	72	28	168	12.9	114
TiO ₂ AB _{1.5,24}	45	55	150	11.5	85
TiO AB _{2.0,24}	23	77	150	11.5	68
TiO ₂ B _{6.0,24}	-	100	151	11.6	57

3.2.1.2. Photocatalytic degradation of dichloroacetic acid using TiO₂ anatase nanoparticles, anatase/brookite mixtures, and brookite nanorods

Since the photocatalytic properties of the anatase/brookite mixtures and of the brookite nanorods have hardly been studied before and little is thus known concerning their properties, the photocatalytic degradation of dichloroacetic acid, DCA, a well-known model pollutant has also been studied. The photocatalytic degradation tests were performed at pH 3. The pK_a of DCA is 1.29,[127] and it thus exists in its anionic form in aqueous solutions at pH > 2. The photocatalytic oxidation of one DCA anion results in the formation of one proton, two CO₂ molecules, and two Cl⁻ ions according to equation 2.1. The pH of the suspensions was maintained constant during the photocatalytic experiments using a pH-stat technique as described by Bahnemann et al.[109, 110]



The rate of the photodegradation of DCA was followed by measuring the amount of OH⁻ added to keep the pH constant thus measuring the amount of H⁺ formed which is equivalent to the amount of DCA degraded. The mineralization of DCA was confirmed by TOC measurements at the end of the experimental runs. In all runs, more than 90 % DCA removal was observed. The photonic efficiencies (ζ) of the photocatalytic degradation of DCA were calculated from the initial degradation rate of DCA and the incident photon flux according to equations 3.1 and 3.2, where the initial degradation rate is calculated from the slope of the individual concentration versus time profiles (see Figure 3.29). The incident photon flux per volumetric unit has been calculated to be 3.31×10^{-2} einstein l⁻¹ h⁻¹ based upon the UV-A light meter measurements and assuming an average illumination wavelength $\lambda = 350$ nm; the irradiated surface area was 3.14 cm², and the volume of the suspension was 0.06 l.

$$I_0 = \frac{I \cdot \lambda}{N_A \cdot h \cdot c} \quad (\text{Eq. 3.1})$$

$$\zeta(\%) = \frac{k \cdot c_0 \cdot V}{I_0 \cdot A} \cdot 100 \quad (\text{Eq. 3.2})$$

with I_0 being the photon flux, I the light intensity, N_A Avogadro's number, h the Planck constant, c the light velocity, k the initial rate constant, A the illuminated area, c_0 the initial DCA concentration, λ the average illumination wavelength, and V the reactor volume.

The calculated rates and photonic efficiency values as well as the respective BET surface areas of the investigated powders are given in Table 3.8. The results show that the photonic efficiencies of the photocatalytic DCA degradation decrease as the content of the brookite

phase in the investigated powders decreases exhibiting the same trend as the BET surface area, followed by a slight decrease and subsequently a leveling off. The photonic efficiencies of DCA degradation have been compared with those of TiO₂ P25. The results revealed that anatase nanoparticles exhibit higher photonic efficiency than TiO₂ P25 whereas anatase/brookite mixtures and pure brookite have lower photonic efficiencies than TiO₂ P25 (see Table 3.8).

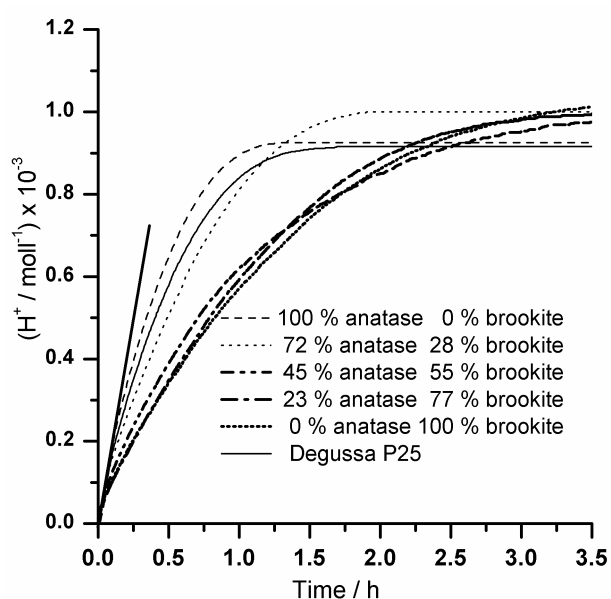


Figure 3.29. Time course of photocatalytic DCA degradation using anatase nanoparticles, anatase/brookite mixtures, and brookite nanorods as a photocatalysts. Conditions: 0.5 g l⁻¹ photocatalysts, 60 ml O₂-saturated aqueous solution (1 mM, 0.06 mmol DCA), a cut-off filter (WG 320) which eliminates UV-radiation below $\lambda = 320$ nm, UV(A)-Vis illumination (60 mW cm⁻²), temperature (25 °C), pH = 3.0.

Table 3.8. Initial rates (R_i) and photonic efficiencies (ζ) of photocatalytic DCA degradation on anatase nanoparticles, anatase/brookite mixtures, and brookite nanorods as well as the respective BET surface areas. Conditions: 0.5 g l⁻¹ catalysts, incident photon flux per volumetric unit = 3.31×10^{-2} einstein l⁻¹ h⁻¹.

Nanomaterials	Anatase (%)	Brookite (%)	$R_i \times 10^{-3}$ (mol l ⁻¹ h ⁻¹)	ζ (%)	BET surface area (m ² g ⁻¹)
TiO ₂ A _{0.1,24}	100	-	1.8	5.44	154
TiO ₂ AB _{1.0,24}	72	28	1.67	5.05	114
TiO ₂ AB _{1.5,24}	45	55	1.30	3.93	85
TiO ₂ AB _{2.0,24}	23	77	1.15	3.48	68
TiO ₂ B _{6.0,24}	-	100	1.14	3.45	57
TiO ₂ P25	82	-	1.60	4.80	52

3.2.2. Gas phase reactions

3.2.2.1. Photocatalytic decomposition of acetaldehyde using TiO₂ rutile nanorods

The photocatalytic activities of the rutile nanorods either embedded in or decorated with anatase nanoparticles as well as those free of anatase were evaluated by the decomposition of gaseous acetaldehyde. The photonic efficiency ζ , which is defined as the ratio of the degradation rate of acetaldehyde and the incident photon flux (calculated for the mean irradiation wavelength of 350 nm and the employed light intensity) related to the illuminated area, was calculated according to the following equations:

$$I_0 = \frac{I \cdot \lambda}{N_A \cdot h \cdot c} \quad (\text{Eq. 3.1})$$

$$\zeta(\%) = \frac{\Delta \dot{n}_{\text{acetaldehyde}}}{I_0 \cdot A} \cdot 100 \quad (\text{Eq. 3.3})$$

with I_0 = light flux; I = light intensity; N_A = Avogadro's number; h = Planck constant; c = light velocity; λ = wavelength; $\Delta \dot{n}_{\text{acetaldehyde}}$ is the difference between inlet and outlet flux of acetaldehyde; A is the illuminated area of the TiO₂ film.

With the illumination area being $A = 30 \text{ cm}^2$ the complete degradation of all incoming acetaldehyde with an initial concentration of 1 ppm, which corresponds to $\Delta \dot{n}_{\text{acetaldehyde}} = 6.76 \times 10^{-10} \text{ mol s}^{-1}$, results in a maximum achievable photonic efficiency ζ_{th} of 0.77 %. All efficiencies of the analyzed samples were calculated after 120 min illumination time to ensure steady-state behavior and to avoid adsorption/desorption effects.

The photonic efficiencies of the rutile nanorods either embedded in (RA24) or decorated with anatase nanoparticles (RA48) and those of the pure rutile nanorods (R72 and R96) are summarized in Table 3.9. For comparison, the photonic efficiencies of TiO₂ P25 and of commercial rutile TiO₂ nanoparticles powders are also presented. The rutile nanoparticles powders have particle size of 25 and 34 nm and BET surface area of 42 and 33 $\text{m}^2 \text{ g}^{-1}$, respectively, and denoted as R25 and R34, respectively.

Table 3.9. Rates ($\Delta\dot{n}_{\text{acetaldehyde}}$) and photonic efficiencies (ζ) of the photocatalytic decomposition of gaseous acetaldehyde on rutile nanorods decorated with anatase nanoparticles and on pure rutile nanorods as well as the respective BET surface areas. Conditions: 3.33 mg cm⁻² photocatalysts, TiO₂ films (30 cm²), initial acetaldehyde concentration (1.0 ppm), 50 % relative humidity, gas flow (1006 ml min⁻¹), UV(A) illumination ($I = 1.0 \text{ mW cm}^{-2}$, $I_0 = 2.93 \times 10^{-9} \text{ einstein s}^{-1} \text{ cm}^{-2}$), ambient temperature (25 °C).

Nanomaterials	Anatase (%)	Rutile (%)	$\Delta\dot{n}_{\text{acetaldehyde}} \times 10^{-10}$ (mol s ⁻¹)	ζ (%)	BET surface area (m ² g ⁻¹)
TiO ₂ RA24	53	47	4.70	0.535	92
TiO ₂ RA48	9	91	5.56	0.633	16
TiO ₂ R72	-	100	0.84	0.096	6
TiO ₂ R96	-	100	0.61	0.070	6
TiO ₂ P25	82	18	5.42	0.617	52
TiO ₂ R25	-	100	2.90	0.330	42
TiO ₂ R34	-	100	2.08	0.237	33

3.2.2.2. Photocatalytic decomposition of acetaldehyde using TiO₂ anatase nanoparticles, anatase/brookite mixtures, and brookite nanorods

The photocatalytic activities of anatase nanoparticles, of anatase/brookite mixtures, and of brookite nanorods were also evaluated by the decomposition of gaseous acetaldehyde. The photocatalytic oxidation of acetaldehyde was obtained over 0.5 g TiO₂ powder. It was spread in a geometrical area of 6.25 cm² and a depth of 2 mm employing a Plexi-Glass sample holder and then pressed to get smooth surface. UV(A) light with an intensity of 1.0 mW cm⁻² and a mean wavelength of $\lambda = 350 \text{ nm}$ has also been used.

The photonic efficiencies were calculated according to equations 3.1 and 3.3. With the illumination area being $A = 6.25 \text{ cm}^2$ the complete degradation of all incoming acetaldehyde with an initial concentration of 1 ppm, which corresponds to $\Delta\dot{n}_{\text{acetaldehyde}} = 6.76 \times 10^{-10} \text{ mol s}^{-1}$, results in a maximum achievable photonic efficiency ζ_{th} of 3.7 %. All efficiencies of the analyzed samples were calculated after 120 min illumination time to ensure steady-state behavior and to avoid adsorption/desorption effects. The photonic efficiencies of anatase nanoparticles, of anatase/brookite mixtures, and of brookite nanorods are summarized in Table 3.10. For comparison, the photonic efficiencies of TiO₂ P25, TiO₂ UV100 and TiO₂ P25HT have also been calculated and presented in Table 3.10.

Table 3.10. Rates ($\Delta\dot{n}_{\text{acetaldehyde}}$) and photonic efficiencies (ζ) of the photocatalytic decomposition of gaseous acetaldehyde on anatase nanoparticles, on anatase/brookite mixtures, and on brookite nanorods as well as the respective BET surface areas. Conditions: 0.08 g cm⁻² photocatalysts, TiO₂ pellets (6.25 cm²), initial acetaldehyde concentration (1.0 ppm), 50 % relative humidity, gas flow (1006 ml min⁻¹), UV(A) illumination ($I = 1.0$ mW cm⁻², $I_0 = 2.93 \times 10^{-9}$ einstein s⁻¹ cm⁻²), ambient temperature (25 °C).

Nanomaterials	Anatase (%)	Brookite (%)	$\Delta\dot{n}_{\text{acetaldehyde}} \times 10^{-10}$ (mol s ⁻¹)	ζ (%)	BET surface area (m ² g ⁻¹)
TiO ₂ A _{0.1,24}	100	-	2.98	1.63	154
TiO ₂ AB _{1.0,24}	72	28	3.05	1.67	114
TiO ₂ AB _{1.5,24}	45	55	2.71	1.48	85
TiO ₂ AB _{2.0,24}	23	77	2.63	1.44	68
TiO ₂ B _{6.0,24}	-	100	2.34	1.28	57
TiO ₂ P25	82	-	2.16	1.18	52
TiO ₂ UV100	100	-	2.58	1.41	301
TiO ₂ P25HT	100	-	2.43	1.33	180

4. Discussion

4.1. Proposed formation route of TiO₂ nanomaterials

4.1.1. TiO₂ anatase nanoparticles

Numerous studies on titanate structures followed the discovery that the hydrothermal treatment of TiO₂ materials in highly alkaline solution (10 M NaOH) yields titanate nanotubes.[65, 66] Recently, it was reported that the different post-treatments affect the structural features of the titanate structures and even lead to the formation of single-crystalline anatase nanoparticles with a specific crystal-growth direction and a large surface area.[60, 128] Utilizing this information, anatase nanoparticles with a large surface area (180 m² g⁻¹) were synthesized starting from TiO₂ P25, which has a rather small surface area (50 m² g⁻¹).

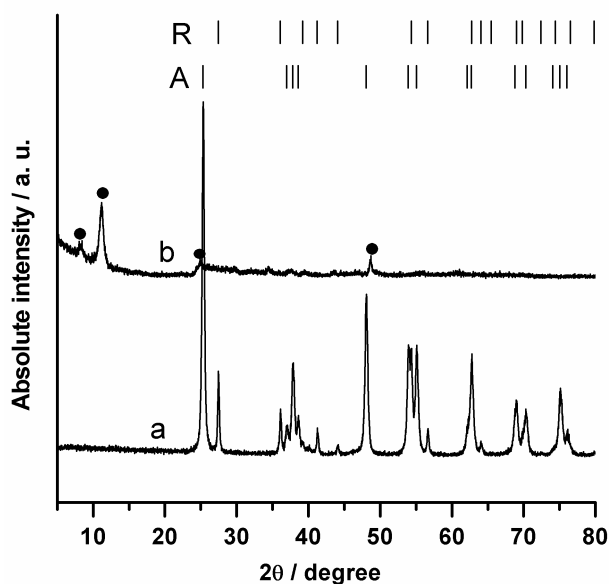


Figure 4.1. XRD diffraction patterns of (a) TiO₂ P25, (b) titanate structure obtained after washing with 0.1 M HCl and deionized water, respectively. Labels A and R indicate Bragg positions for anatase and rutile, respectively. Label ● indicates Bragg positions for titanate structure.

The hydrothermal treatment of TiO₂ P25 which is a mixture from anatase (82 %) and rutile (18 %) followed by washing with 0.1 M HCl solution and with deionized water, respectively, yields a titanate structure as proven by XRD analysis (cf. Figure 4.1 a and b). The diffraction peaks assigned to the anatase and the rutile phases completely disappeared after the hydrothermal treatment. Only a few peaks at $2\theta = 24^\circ$, 48° , 10° , respectively, which can be indexed to the titanate structure, were observed.[128] The post-treatment of this titanate structure in 0.5 M HCl overnight results in a phase-transition from Na-containing titanate and

protonic titanate to anatase TiO_2 as evincing from the XRD patterns in Figure 4.2a and b. As shown in Figure 4.2, after acid treatment of the titanate structure with 0.5 M HCl overnight, the peak at $2\theta = 24^\circ$ shifts to $2\theta = 25^\circ$, accompanied by a marked weakening of the peaks at $2\theta = 10^\circ$ and 48° , especially the former. The peak at $2\theta = 25^\circ$ should correspond to the (101) diffraction of anatase TiO_2 . Previous studies have also reported the transformation of protonic titanate to the anatase phase under acidic conditions.[129, 130] Calcination of the acid treated titanate powder at 400°C for 2 h exclusively yields anatase TiO_2 nanoparticles (cf. Figure 3.1 c).

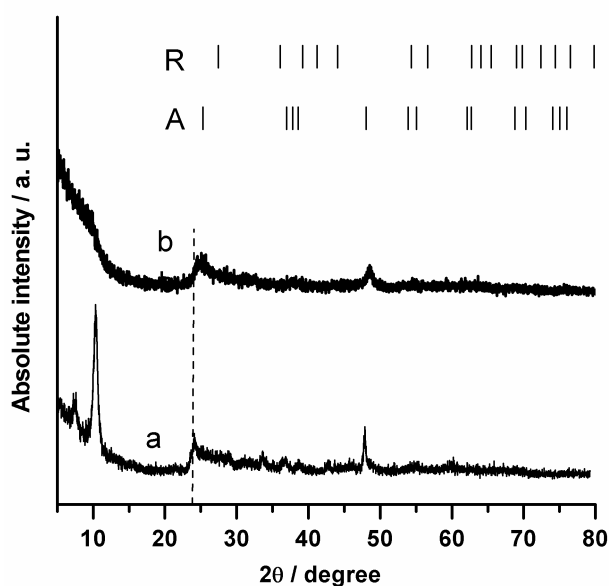


Figure 4.2. XRD diffraction patterns of (a) titanate structure obtained after washing with 0.1 M HCl and deionized water, respectively and (b) titanate structure obtained after washing with 0.1 M HCl and deionized water, respectively, and then followed by treatment in 0.5 M HCl overnight. Labels A and R indicate Bragg positions for anatase and rutile, respectively.

Based on these results and on the reported data, the formation and transformation of titanate nanotubes and/or nanofibers induced by the NaOH treatment and post-treatment washing has been summarized in the scheme shown in Figure 4.3. Upon NaOH treatment, some of the Ti–O–Ti bonds are broken, forming an intermediate containing Ti–O–Na and Ti–OH. These intermediates then proceed with rearrangements and swelling to form sheets of edge sharing TiO_6 octahedra with intercalated Na^+ and OH^- . Thus, the formed structure resembles $\text{Na}_2\text{Ti}_2\text{O}_5 \cdot \text{H}_2\text{O}$ (i.e., $\text{Na}_2\text{Ti}_2\text{O}_4(\text{OH})_2$). The projection along [001] of this sodium titanate exhibits layers of TiO_6 octahedra edge shared in a zigzag configuration (cf. Figure 4.3). In a previous study it was also pointed out that if the two longer Ti–O bonds in the TiO_6 octahedra were broken, the anatase TiO_2 would transform into the layered titanate.[131]

However, results published in the literature have shown that both anatase and rutile can be transformed into titanate nanostructures via the NaOH treatment.[128] The formed $\text{Na}_2\text{Ti}_2\text{O}_5 \cdot \text{H}_2\text{O}$ will undergo Na^+ exchange with H^+ during the post-treatment acid washing. This exchange will result in a variation of the surface charge, leading to a peeling-off of the individual layers of the titanate and to the subsequent scrolling of the layers into nanotubes or nanofibers.[131] The x value of the titanate structure, $\text{Na}_{2-x}\text{H}_x\text{Ti}_2\text{O}_5 \cdot \text{H}_2\text{O}$, increases with the acidity of the post-treatment. At highly acidic post-treatment, anatase rather than titanate appears, as proven by the XRD results (Figure 4.2a and b). This indicates that the tube and/or fiber walls proceed with dehydration, forming the anatase structure at some locations of the titanate structures. During this transformation, the titanate framework will shrink by the reduction of the interlayer distance. Because of the similar zigzag configuration, the (001) projection of the titanate layers will shrink to the (101) faces of anatase TiO_2 , leading to a defective structure in the titanate structures. With a gradual increase in this transformation by increasing the post-treatment acidity, the titanate structures eventually rupture to form small anatase crystallites. Thus, the post calcinations will lead exclusively to anatase nanoparticles with high surface area and probably with a specific crystal-growth direction.

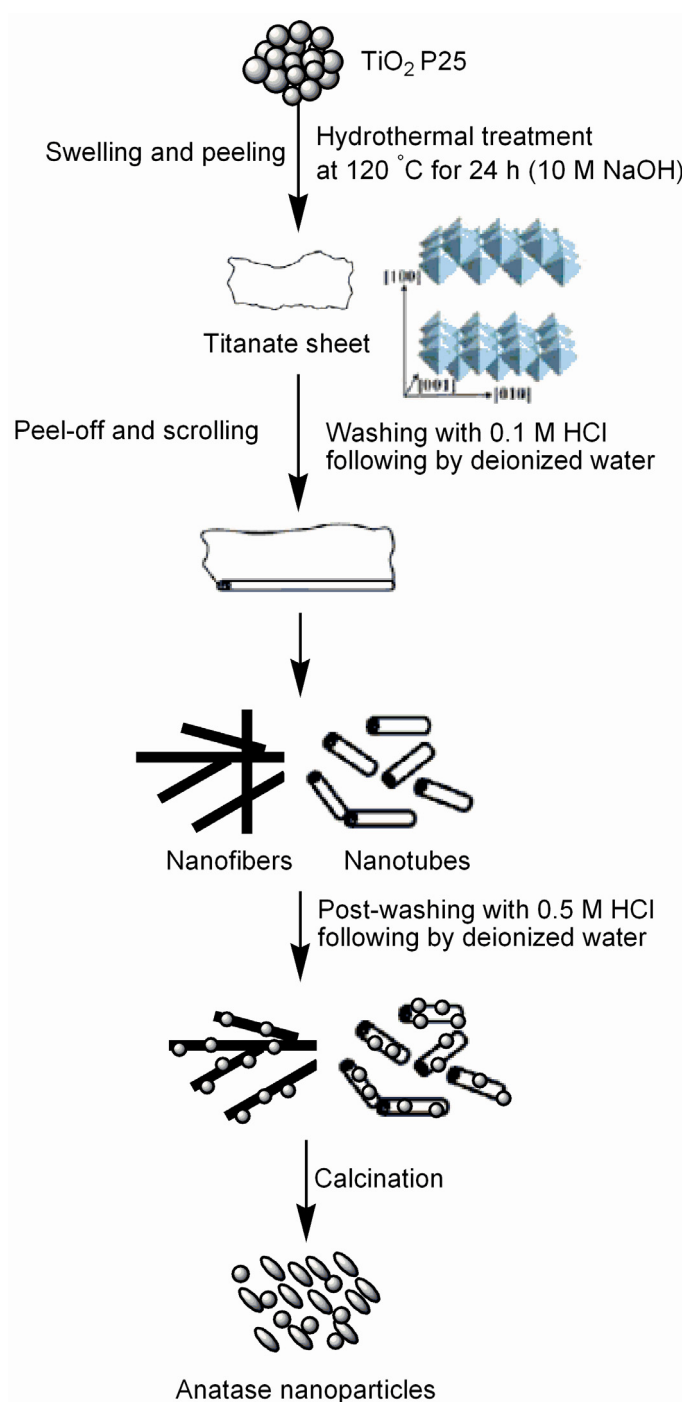


Figure 4.3. Schematic model for the preparation of anatase nanoparticles by transformation of titanate structures induced by the NaOH treatment and the post-treatment washing.

4.1.2. TiO₂ rutile nanorods

The observed formation of rutile nanorods decorated with anatase nanoparticles and of pure rutile nanorods by hydrothermal treatment of aqueous solutions of the TALH complex at 200 °C for different reaction times (24, 48, 72, and 96 h) is in disagreement with published results. Möckel et al. [85] observed the formation of anatase TiO₂ nanoparticles during the thermal hydrolysis of the TALH complex at slightly different conditions, i.e., employing sealed glass ampoules or a titanium autoclave. They noted that characteristic rutile needles are formed besides these anatase nanoparticles only when the thermal hydrolysis experiment was performed at temperatures around 400 °C in a titanium autoclave. An effect of the reaction time on the crystal size of the anatase nanoparticles was only observed at the beginning of the reaction at temperatures below 300 °C. To obtain further insight into the underlying mechanism, one thermal hydrolysis experiment was carried out employing sealed glass ampoules at 160 °C for 48 h; however, it yielded a biphasial anatase/rutile mixture as seen in Figure 4.4.

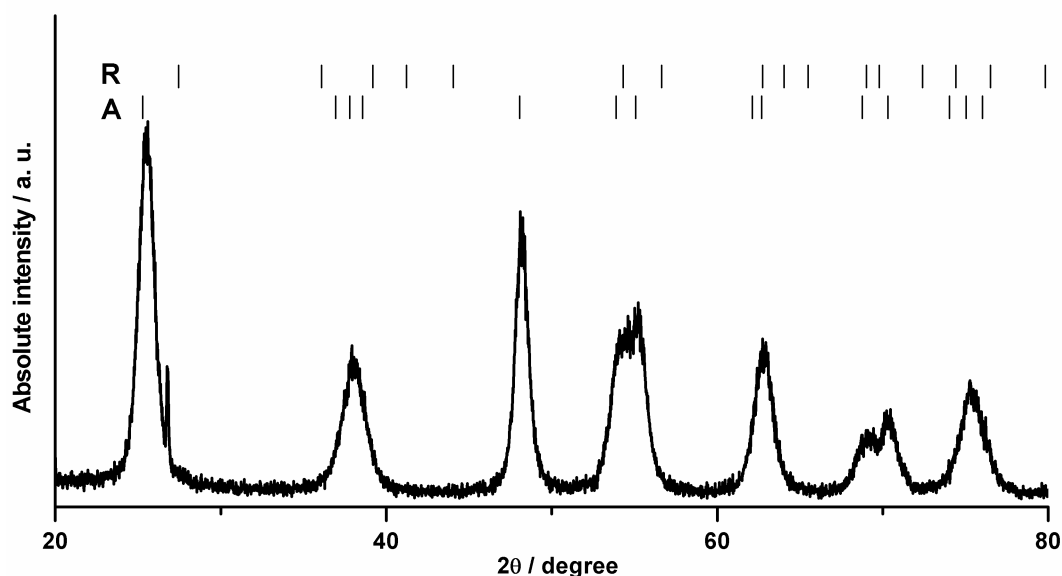


Figure 4.4. XRD patterns of as-synthesized nanocrystalline TiO₂ powders obtained by thermal hydrolysis of aqueous solutions of the TALH precursor at 160 °C for 48 h employing sealed glass ampoules. Labels R and A indicate Bragg positions for rutile and anatase, respectively.

In the present work, all further experiments have been carried out employing a Teflon cup as described in the experimental section (section 2.2.2). The XRD data (cf. Figure 3.8) clearly indicate that biphasial anatase and rutile mixtures are already formed after 24 and 48 h of

hydrothermal treatment of the TALH complex at 200 °C. At longer reaction times (72 and 96 h), only the pure rutile polymorph is obtained (cf. Figure 3.8c and d). These results indicate that there is a phase transformation from anatase nanoparticles to rutile nanorods with an increase of the reaction time. The hydrothermal treatment of rutile free anatase TiO₂ nanoparticles at 200 °C in the presence of ammonium lactate (a product expected from the thermal hydrolysis of the TALH complex) resulted only in an increase of the size of the nanoparticles but not in a direct transformation of anatase to rutile. From this experiment, it can be concluded that under the applied experimental conditions it is unlikely for anatase to transform to rutile without rutile nuclei being present. It has been reported that the presence of rutile seeds accelerates the crystallization of TiO₂ making the formation reaction of rutile kinetically more favorable than the formation of anatase during the hydrolysis of TiCl₄ at low temperature.[132] It is also important to mention that the hydrothermal treatment of the TALH complex for shorter reaction time (12 h) or at lower temperature (120 °C) leads to the formation of stable suspensions of TiO₂ nanoparticles. It is therefore assumed that small anatase and rutile TiO₂ nuclei covered with lactate anions as hydroxycarboxylate ligands are formed at the early stage of the reaction. Recently, a similar behavior was reported by Kakihana and co-workers [73, 75] who obtained pure rutile TiO₂ by hydrothermal treatment of aqueous solutions of the titanium glycolate complex at 200 °C for reaction times exceeding 24 h whereas mixtures of anatase and rutile TiO₂ were obtained at 160 °C (24 h reaction time) and at 200 °C (6 h reaction time).

Depending on the experimental results of the present work, the proposed formation route of the rutile TiO₂ nanorods is schematically given in the scheme presented in Figure 4.5: (1) condensation-dehydration reaction between the –OH ligands forming Ti–O–Ti oxo species, (2) competing formation of anatase and rutile seeds, and (3) anisotropic growth of the rutile TiO₂ seeds as the thermodynamically more stable phase, accompanied by the consumption of the small anatase TiO₂ nanoparticles. The anisotropic crystal growth along the c-axis [001] direction of the rutile TiO₂ seeds leads to the formation of rutile nanorods with primarily (110) type facets as confirmed by TEM analysis. This can be explained by the well established fact that during crystal growth a fast growing plane with a high surface energy tends to disappear leaving behind slower growing planes with lower surface energies. It is known that the (110) plane of rutile TiO₂ has the lowest surface energy whereas the (001) plane has the highest surface energy.[133-135] Additionally, the anisotropic crystal growth observed during the thermal hydrolysis of the TALH complex might be facilitated by the presence of lactate anions acting as chelating ligands attached to the surfaces of the

nanoparticles and thus possibly inhibiting the growth along other crystallographic directions.[136] Similar preferential growth of rutile nanorods along the c-axis has previously been reported.[137-139]

As observed in the FE-SEM and HR-TEM micrographs (Figures 3.9 and 3.10), the rutile nanorods obtained after 24 and 48 h of hydrothermal treatment are either embedded in or decorated with anatase nanoparticles (3-5 nm). These anatase nanoparticles adhere strongly to the surface of the rutile nanorods. In case of rutile nanorods embedded in anatase nanoparticles, it is possible to remove all excess anatase particles by washing which, however, does not remove the anatase particles adhering to the rutile surface. The strong interaction of these nanoparticles with the rutile nanorods' surfaces can be explained by the fact that at the end of all synthesis processes the final pH of the solution was found to be in the range of 5 to 5.3 (cf. Table 3.2). These pH values are close to the zero point of charge (pH_{ZPC}) of TiO_2 . [140, 141] Hence, the van der Waals attraction between the anatase nanoparticles and the rutile nanorods are expected to be strong since the electrostatic repulsion between particles are limited by their electrostatic surface charge density.

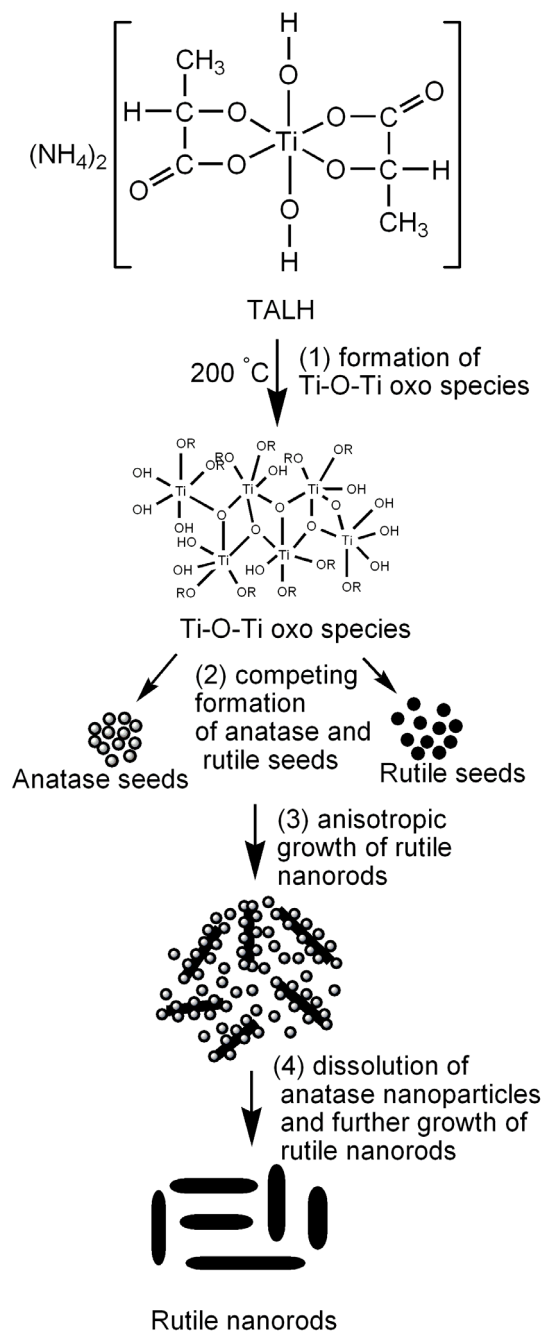


Figure 4.5. Proposed steps for the formation and the anisotropic growth of TiO₂ rutile nanorods.

4.1.3. TiO₂ anatase nanoparticles, anatase/brookite mixtures, and brookite nanorods

TiO₂ anatase nanoparticles, tailored anatase/brookite mixtures, and brookite nanorods are obtained by the thermal hydrolysis of titanium(IV) bis(ammoniumlactate) dihydroxide aqueous solutions in the presence of different concentrations of urea. The reaction ratio between anatase and brookite can readily be controlled by adjusting the urea concentration. To understand the reaction pathway, the ratio between anatase and brookite nanoparticles has been investigated at different reaction times during the synthesis process; namely after 3, 6, 12, 48 and 72 h while both urea concentration (1.0 M) and temperature (160 °C), were kept constant. The Rietveld analysis of the XRD pattern of the powder obtained after a reaction time of 3 h proves the presence of anatase and brookite phases; however, the phase composition can not be precisely determined due to the overall very low crystallinity. Whereas the Rietveld analysis of the XRD patterns of the other powders indicates that reaction times greater than 6 h have no effect on the ratio between anatase and brookite, also no apparent change in the crystallite size was observed after a reaction time of 12 h (cf. Figure 4.6 and Table 4.1).

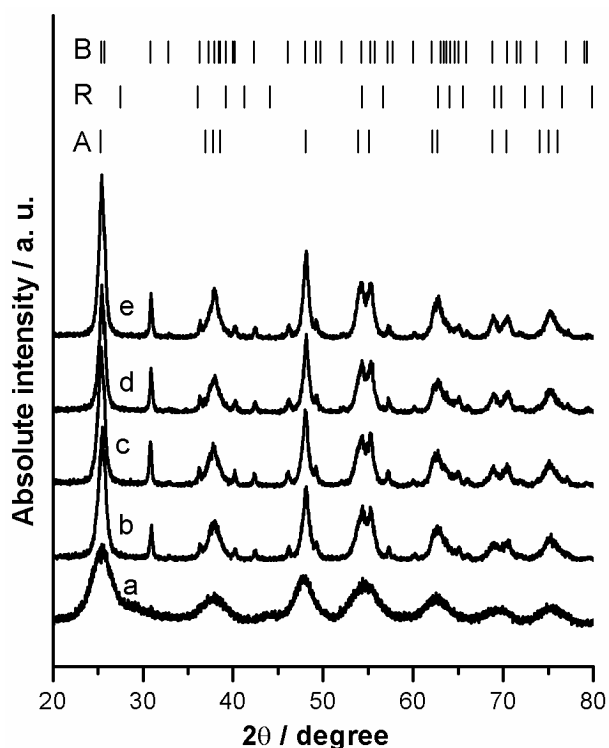


Figure 4.6. XRD patterns of as-synthesized nanocrystalline TiO₂ powders obtained by thermal hydrolysis of aqueous solutions of the TALH precursor at 160 °C for (a) 3 h, (b) 6 h, (c) 12 h, (d) 48 h, and (e) 72 h in the presence of 0.1 M of urea. Labels B, R, and A indicate Bragg positions for brookite, rutile, and anatase, respectively.

Table 4.1. Quantitative phase composition and crystallite sizes of nanocrystalline TiO₂ prepared by thermal hydrolysis of the TALH precursor at different reaction times and temperatures in the presence of 1.0 M of urea.

T (°C)	Reaction time (h)	Anatase (%)	Anatase crystallite size (nm)	Brookite (%)	Brookite crystallite size (nm)
160	6	77	6	23	20
160	12	77	10	23	38
160	24	72	12	28	40
160	48	72	11	28	40
160	72	75	14	25	40
120	24	82	6	18	22
200	24	87	13	13	32

These results are in good agreement with the previously reported fact that anatase nanoparticles with diameters ≤ 11 nm represent the most stable phase, while brookite nanoparticles with diameters between 11 and 35 nm are the most stable phase. [50, 51, 142] However, in the present study brookite has nanorod morphology with diameters up to 25 nm and lengths up to 150 nm. These results also indicate that there is no phase transformation between anatase and brookite under the applied conditions and that there is no further particle growth with an increase of the reaction time as proven by the scanning electron microscopy results. Depending on these results, more likely, brookite does not form through intermediate phases, the brookite seeds are rather directly formed from the TALH complex and continue to grow in the solution until reaching the appropriate size in good agreement with a previously reported observation.[74] The effect of temperature on the anatase/brookite ratio has also been investigated at 120 °C and 200 °C. The Rietveld analysis of the XRD patterns of the obtained powders indicates that the temperature has a minor effect on the anatase/brookite ratio (cf. Figure 4.7 and Table 4.1). It was also noted that the final pH in all experimental runs is about 9.9 when urea concentrations higher than 0.5 M were employed during the synthesis process. This reveals that under the present conditions the increase of the brookite content in the obtained powders at different urea concentrations is not governed by the final pH but rather by the dosing of the in situ produced OH⁻. To ensure the importance of the in situ OH⁻ generation for the formation of the brookite phase, one experiment has been performed at pH 9.9 employing ammonium hydroxide instead of urea for 24 h at 160 °C. The Rietveld analysis of the XRD pattern of the isolated powder indicates that the product is 100 % anatase (cf. Figure 4.8).

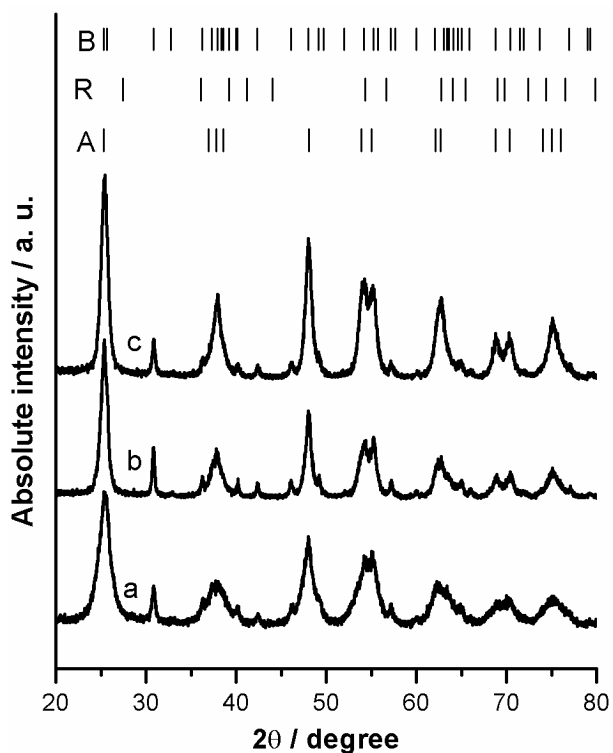


Figure 4.7. XRD patterns of as-synthesized nanocrystalline TiO_2 powders obtained by thermal hydrolysis of aqueous solutions of the TALH precursor at (a) 120 °C, (b) 160 °C, and (c) 200 °C for 24 h in the presence of 0.1 M of urea. Labels B, R, and A indicate Bragg positions for brookite, rutile, and anatase, respectively.

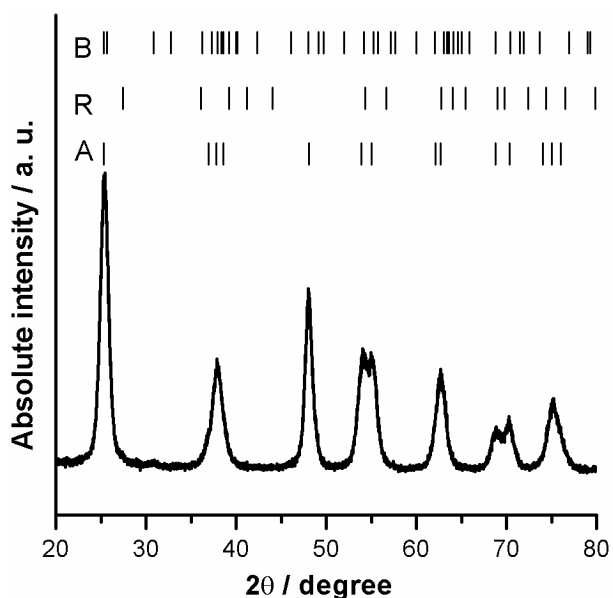


Figure 4.8. XRD patterns of as-synthesized nanocrystalline TiO_2 powders obtained by thermal hydrolysis of aqueous solutions of the TALH precursor at 160 °C for 24 h in the presence of NH_4OH (pH = 9.9). Labels B, R, and A indicate Bragg positions for brookite, rutile, and anatase, respectively.

From the results reported so far it becomes obvious that the anatase/brookite ratio is mainly controlled by the concentration of urea. Urea hydrolyzes extremely slowly at room temperature but more rapidly at temperatures higher than 90 °C producing OH⁻ ions (Eq. 4.1).[76] The observed first order rate constant for urea decomposition in water at 90 °C was reported to be 1.04×10⁵ sec⁻¹. [143] At low urea concentrations, the in situ produced OH⁻ ion dosing is only sufficient for a slow hydrolysis of the TALH precursor leading to the formation of pure anatase nanoparticles. An increase in the urea concentration leads to an increase in the OH⁻ ion dosing resulting in the rapid thermal hydrolysis of the TALH precursor and the formation of both anatase and brookite seeds. From the experimental results presented here it can be concluded that the increase of the in situ OH⁻ ion dosing favours the formation of brookite seeds. Once the formation of brookite or anatase seeds has occurred, it seems reasonable that the growth of the crystallites requires lower activation energy than the transformation to another phase. The increase of the urea concentration, also, might somehow effect the stereo conformation of the TALH complex so that the complex structure resembles the architecture of brookite. This will facilitate the brookite formation as previously suggested,[71] however, a complexation of urea with Ti(IV) appears to be unlikely, since urea complexes with Ti(IV) should have a rather low stability as compared with, e.g., lactate. If urea reacts with Ti(IV) as bidentate ligand, it will form a four-membered ring that is less stable than a five-membered ring formed by lactate. Even the possibility of urea reacting as monodentate ligand can be readily excluded by the fact that no change in the UV-Vis spectra of the TALH complex was observed after treatment with urea indicating that there is no ligand exchange. Based upon the experimental results the proposed reaction pathways are summarized in Figure 4.9.



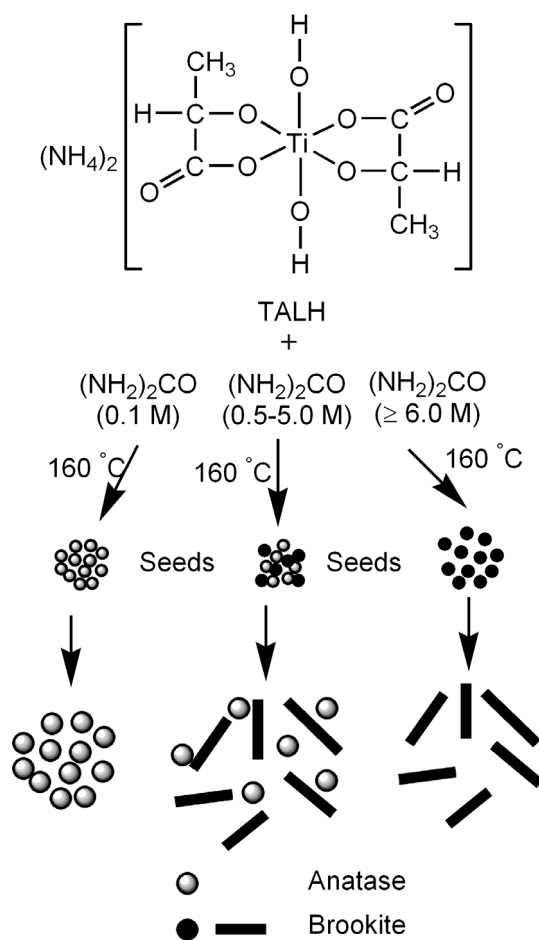


Figure 4.9. Proposed routes for the formation of anatase nanoparticles and brookite nanorods.

4.2. Evaluation of the photocatalytic activities

4.2.1. Liquid phase reactions

4.2.1.1. Photocatalytic H₂ evolution from aqueous methanol solution over:

(a) Pt-loaded TiO₂ P25, TiO₂ UV100, and TiO₂ P25HT

Despite the fact that TiO₂ exhibits generally relatively high photocatalytic activity towards the degradation of organic compounds under UV illumination in the presence of molecular oxygen, it usually does not show any ability to photocatalyse the H₂ evolution in oxygen free systems even in the presence of an electron donor. When TiO₂ absorbs a photon the energy of which exceeds its bandgap energy, an electron (e⁻)/hole (h⁺) pair is generated. Both e⁻ and h⁺ can either migrate to the TiO₂ surface and react with adsorbed reactants in a photocatalytic process, or they may undergo an undesired recombination. In the presence of an electron donor, such as methanol, and in the absence of O₂, the excess holes will be consumed and the photogenerated electrons will be trapped near the surface forming tri-valent titanium (Ti³⁺) sites instead of reducing H⁺. This phenomenon has been observed by Bahnemann et al. [45] in laser-flash photolysis experiments employing suspensions of colloidal TiO₂. Loading the TiO₂ surface with small Pt islands creates sinks for the electrons thus facilitating the separation of e⁻/h⁺ pairs photogenerated in TiO₂ and promoting the formation of H₂ gas.[9, 37, 46]

TiO₂ P25, TiO₂ UV100, and TiO₂ P25HT have been loaded with 0.5 wt% Pt nanoparticles via a photochemical deposition method as described in the experimental section (section 2.3.1). Pt-loaded TiO₂ UV100 shows higher photocatalytic activity for the evolution of H₂ from aqueous methanol solution (0.03 M, 2.25 mmol methanol) than both Pt-loaded TiO₂ P25 and Pt-loaded TiO₂ P25HT, respectively (cf. Figure 3.17). This higher photocatalytic activity of H₂ formation can be explained, at the first sight, by the fact that the surface area of TiO₂ UV100 is about six times larger than that of TiO₂ P25 and twice as large as that of TiO₂ P25HT (cf. Table 3.1). However, the observed differences in photocatalytic activity, in general, cannot be interpreted using only a single property of the photocatalysts.[3] In fact, the photocatalytic activity depends on various properties, e.g., surface area, crystallinity, particle size, optical properties, structure, and many other factors. For example, the rates of the photocatalytic H₂ evolution over Pt-loaded TiO₂ UV100 and Pt-loaded TiO₂ P25HT were found to be 303 and 252 μmol h⁻¹, respectively, while their BET surface areas are 293 and 169 m² g⁻¹, respectively. Though Pt-loaded TiO₂ UV100 has a significant higher BET surface area than Pt-loaded TiO₂ P25HT, it does not exhibit a much higher photocatalytic activity. This can be, for example, explained by the fact that TiO₂ P25HT exhibits a higher crystallinity

than TiO₂ UV100 as concluded from the crystallite size obtained from the XRD data analysis (cf. Table 3.1).

On the other hand, the significantly higher photocatalytic activity of both TiO₂ UV100 and TiO₂ P25HT as compared with TiO₂ P25 can not only be explained by the fact that the latter has a lower BET surface area but also by the differences in structure and phase composition. TiO₂ UV100 and TiO₂ P25HT exhibit a mesoporous structure as proved by the N₂ adsorption-desorption isotherms (cf. Figure 4.10A and B, respectively), whereas TiO₂ P25 is completely non-porous (cf. Figure 4.10 C).

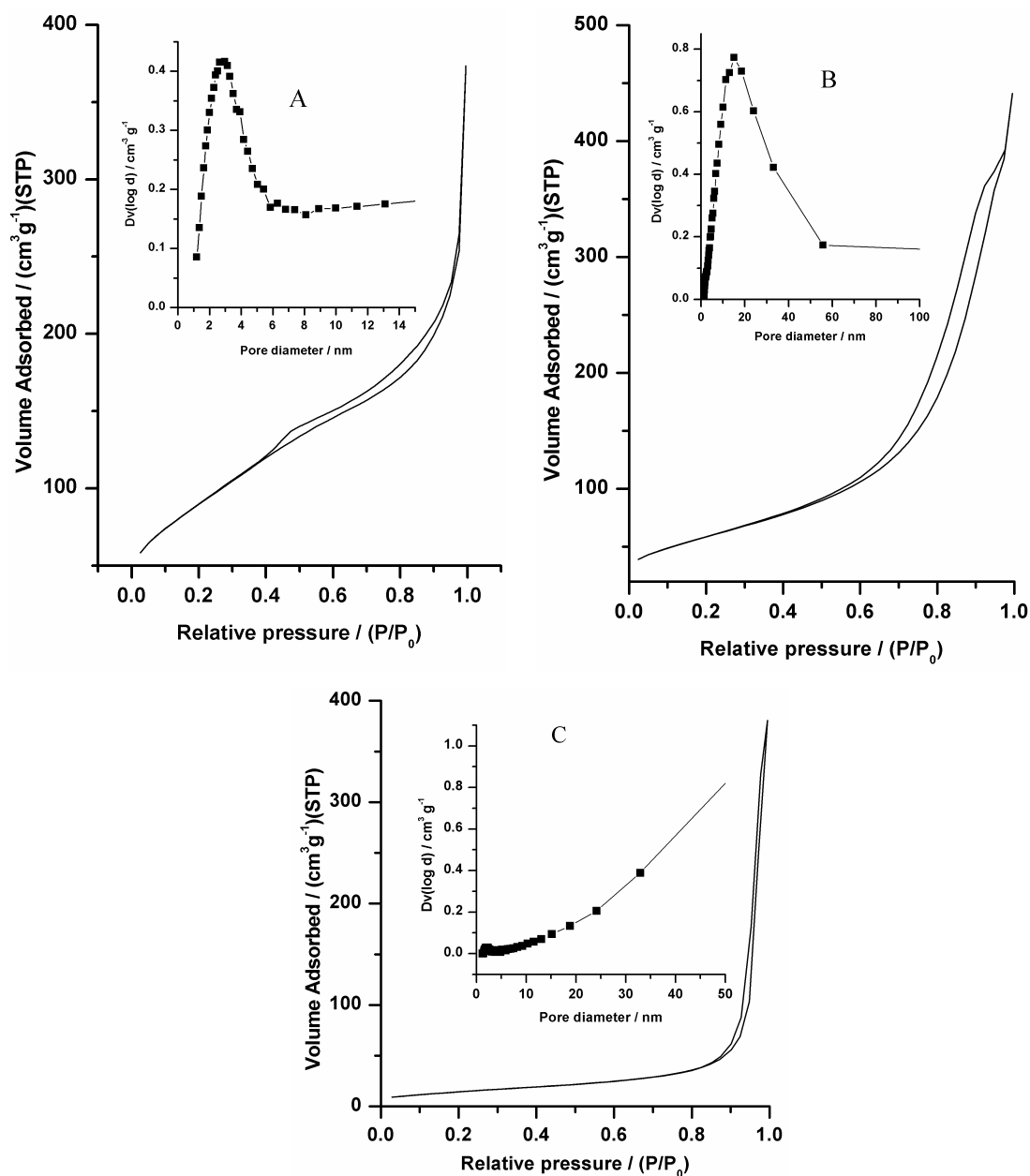


Figure 4.10. N₂ adsorption-desorption BET isotherms of Pt-loaded TiO₂ UV100 (A), of Pt-loaded TiO₂ P25HT (B), and of Pt-loaded TiO₂ P25 (C). The insets show the pore size distribution.

This mesoporous structure may either result from compactly packed nanoparticles or may be due to the agglomeration of the TiO_2 nanoparticles. This mesoporous structure can then provide suitable interfaces for facile interparticle charge transfer while the reactants can freely diffuse through the pores as illustrated in Figure 4.11.[144, 145] While the excited TiO_2 nanoparticle can transfer the absorbed energy through the mesoporous TiO_2 network to other ground-state TiO_2 particles, the probability of the hole trapping at an hydroxyl surface group forming an adsorbed hydroxyl radical that is subsequently transferred to an adsorbed CH_3OH molecule is considered to be high. Consequently, the probability of electron transfer to the Pt particle is increased by an increased CH_3OH diffusion through the pores of the nanostructures. It is therefore suggested that the so-called antenna mechanism [146-148] together with an increased CH_3OH diffusion can be employed to explain the higher photocatalytic H_2 evolution over Pt-loaded TiO_2 UV100 and Pt-loaded TiO_2 P25HT. Within this antenna model, it can be imagined that the overlap of the energy bands of the TiO_2 nanoparticles forming this network will result in unified energy bands for the entire system enabling a quasi-free movement of the photogenerated charge carriers throughout the mesoporous structure. Consequently, an electron generated by light absorption within one of the nanoparticles forming the network will subsequently be available to promote redox processes anywhere within the structure.

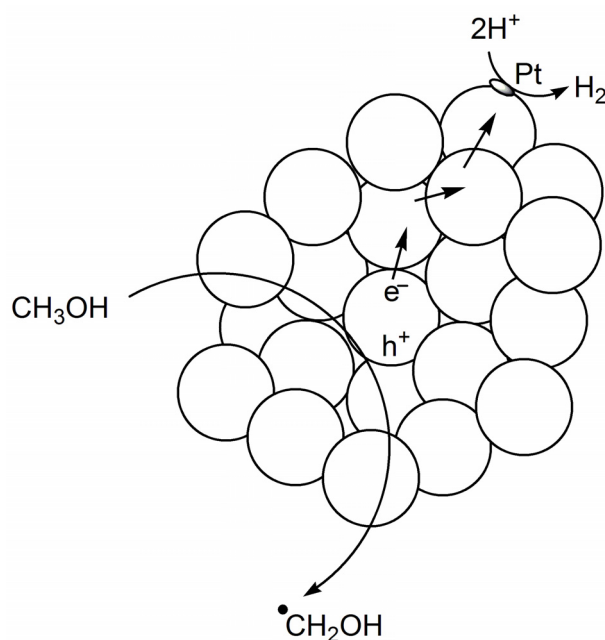


Figure 4.11. Schematic illustration showing the agglomerated TiO_2 nanoparticles with an interparticle charge carrier transport leading to enhanced electron/hole pair separation and with mesoporous structure facilitating the CH_3OH diffusion through the pores.

In order to verify the importance of this proposed antenna mechanism, the ratio of Pt islands to TiO₂ nanoparticles has been calculated. Assuming Pt nanoparticles are spherical and have a diameter of 3.0 nm (for example see Figure 4.12), the volume of one 3.0 nm Pt nanoparticle is $1.41 \times 10^{-20} \text{ cm}^3$. Considering the mass density of Pt is 21.4 g cm^{-3} , the average weight of one Pt nanoparticle is derived to be approximately $3.02 \times 10^{-19} \text{ g}$. Therefore, the number of Pt islands for each gram of 0.5 wt% Pt-loaded TiO₂ was calculated to be 1.65×10^{16} . Assuming spherical TiO₂ nanoparticles with 10 nm average diameter (see Table 3.1) and a mass density of 3.9 g cm^{-3} , the number of TiO₂ nanoparticles per gram were calculated to be 4.91×10^{17} . Thus, the ratio of Pt islands to TiO₂ nanoparticles was calculated to be 1 to 30. This emphasizes the importance of the transfer of the photogenerated electrons throughout the mesoporous structure.

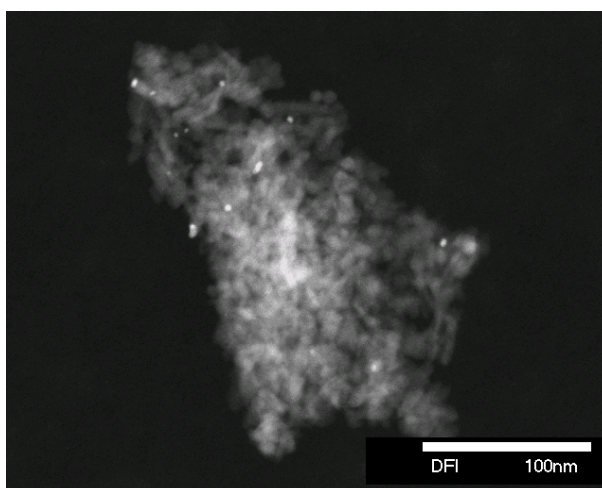


Figure 4.12. DF-TEM micrograph of TiO₂ P25HT modified with 0.5 wt% Pt (photochemical deposition method). Pt is seen as bright points with diameter of about 3.0 nm.

Furthermore, the phase composition might also affect the photocatalytic activity of H₂ evolution. TiO₂ UV100 and TiO₂ P25HT consist of pure anatase phase as proved by XRD analysis, whereas TiO₂ P25 is a mixture of anatase and rutile (82 % anatase and 18 % rutile). The flatband potential of the rutile phase coincides almost exactly with the redox potential of H⁺/H₂ vs. NHE, whereas, that of anatase is shifted cathodically by approximately 200 mV.[149, 150] In the latter case, a considerable driving force for the proton reduction is available, while in the case of rutile this driving force will be very small. This can also explain why TiO₂ UV100 and TiO₂ P25HT are more active than TiO₂ P25.

The effect of light intensity on the reaction rate and on the photonic efficiency of H₂ evolution has also been investigated. According to the data presented in Figure 3.21a and b (see section 3.2.1.1a), it is obvious that in the range of study there is no linear dependence between the light intensity and the rate of H₂ evolution. Deviations from such a linear behavior were observed for both Pt-loaded TiO₂ UV100 and Pt-loaded TiO₂ P25HT. In the case of Pt-loaded TiO₂ P25, the rate increases only initially before it reaches a plateau and remains almost constant upon further increase of the light intensity. Figure 3.21a and b indicate clearly that at low light intensity (4.40 $\mu\text{einstein min}^{-1}$) the rate of H₂ evolution over Pt-loaded TiO₂ P25 is similar to that observed for Pt-loaded TiO₂ UV100 and TiO₂ P25HT, while, at higher light intensity (44.87 $\mu\text{einstein min}^{-1}$) the rate of H₂ evolution over the latter materials is about four times higher than that measured for Pt-loaded TiO₂ P25. Apparently, it is extremely important to consider the effect of light intensity when comparing different photocatalysts. A possible explanation for these differences is that the e⁻/h⁺ recombination rate constant is higher for Pt-loaded TiO₂ P25 leading to the fact that this undesired reaction channel becomes more significant at high light intensity in case of Pt-loaded TiO₂ P25 as compared with Pt-loaded TiO₂ UV100 and Pt-loaded TiO₂ P25HT.

It is well known that the rates of photocatalytic reactions strongly depend on both the concentration of organic compound used as test molecule and the intensity of the incident light. This behaviour is usually described by an empirical kinetic expression, i.e., the so-called Langmuir-Hinshelwood rate law (Eq. 4.2). [11, 151, 152]

$$R = k_r \frac{Kc}{1 + Kc} \eta(I_0)^\beta \quad (\text{Eq. 4.2})$$

where the kinetic parameters k_r and K are usually found to be independent from the incident light intensity I_0 , with $\beta = 1$ at low values of I_0 , and $\beta = 0.5$ at higher I_0 values. β is an empirical constant related to the ratio between interfacial charge transfer and recombination of the charge carriers. Combining the definition of the photonic efficiency ζ , i.e., the ratio between the H₂ production rate and the incident flux of photons I_0 , with equation 4.2 for the initial concentration $c=c_0$ yields

$$\zeta = k_r \frac{Kc_0}{1 + Kc_0} \eta(I_0)^{\beta-1} \quad (\text{Eq. 4.3})$$

$$\log(\zeta) = \log\left(k_r \frac{Kc_0}{1 + Kc_0} \eta\right) + (\beta - 1)\log(I_0) \quad (\text{Eq. 4.4})$$

Equation 4.3 predicts that the photonic efficiency ζ should depend on the initial concentration of the degraded molecule c_0 as well as on the incident photon flux I_0 . In order to

investigate the relation between the light intensity and the photonic efficiency of H_2 production, the photonic efficiencies were calculated at different light intensities. High concentration of methanol was employed during the rate measurements and kept constant to ensure that the measured rate is unaffected by the methanol concentration. Plotting $\log(I_0)$ vs. $\log(\zeta)$ indicates a linear relation as shown in Figure 4.13. According to equation 4.4, the values of β were calculated from the slopes obtained by linear regression and estimated to be 0.84, 0.83, and 0.29 for Pt-loaded TiO_2 UV100, Pt-loaded TiO_2 P25HT and Pt-loaded TiO_2 P25, respectively.

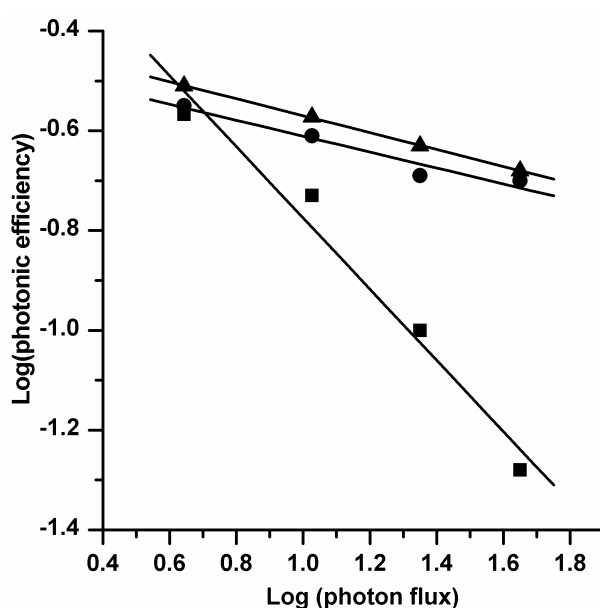
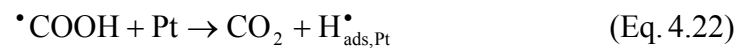
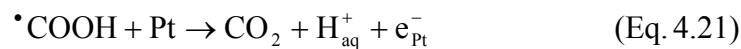
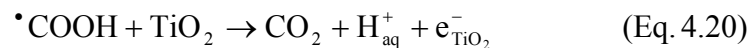
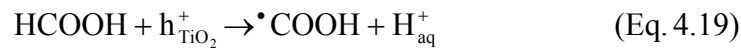
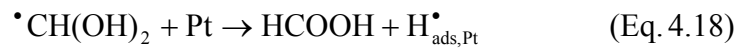
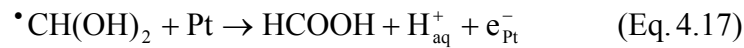
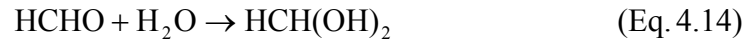
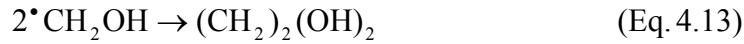
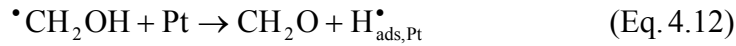
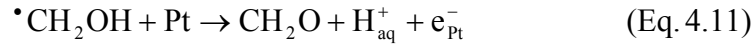
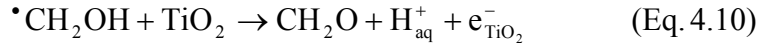
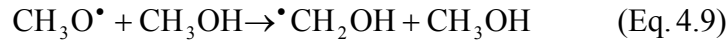
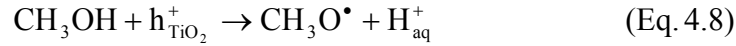
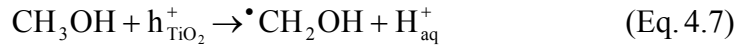


Figure 4.13. Plot of \log (photonic efficiency) vs. \log (photon flux) for the photocatalytic H_2 evolution over 0.5 wt% Pt-loaded photocatalysts (■) TiO_2 P25, (●) TiO_2 P25HT, and (▲) TiO_2 UV100. Conditions: 0.5 g l^{-1} photocatalysts, 75 ml aqueous methanol solutions (370 mmol methanol), UG1 black filter, neutral density filter, UV(A) illumination.

β value of 0.5 was observed in many systems as concluded from the linear dependence between the square root of the absorbed light and the quantum efficiency.[36, 39, 151, 153, 154] Since β is an empirical constant related to the ratio between interfacial charge transfer and recombination of the charge carriers, it is more likely that β value differs from one photocatalyst to another as experimentally found in the present study.

According to the literature [34-37, 155, 156] and depending on the detected products of the photocatalytic methanol oxidation, it is concluded that methanol is photooxidized to carbon dioxide via the formation of the stable intermediates formaldehyde and formic acid. The individual reaction steps can be summarized accordingly:



The e^-/h^+ pairs photogenerated in the TiO_2 particles upon photoexcitation (Eq. 4.5) will migrate to their surfaces where these redox reactions take place. The photogenerated electron will be trapped at the Pt islands (Eq. 4.6) followed by the reduction of a proton from water or/and from methanol producing adsorbed H^\cdot radicals (Eq. 4.23). On the oxidative side, the photogenerated holes will either react with surface Ti-OH groups producing trapped holes or with adsorbed water molecules producing adsorbed $\cdot\text{OH}$ radicals or they will be transferred directly to adsorbed methanol molecules as expressed in equations 4.7 and 4.8. However, the present study does not enable any differentiation between these pathways. The methanol photooxidation through the $\cdot\text{OH}$ pathway has been suggested to occur on bare titanium dioxide surfaces. [34-36, 155, 156] Regardless of which oxidation pathway is more likely, the only expected product of these reaction pathways are $\cdot\text{CH}_2\text{OH}$ and $\text{CH}_3\text{O}\cdot$ formed by hydrogen abstraction from the carbon atom and from the $-\text{OH}$ group of CH_3OH , respectively,

as expressed in equations 4.7 and 4.8. Asmus et al. [44] showed that in homogeneous aqueous solutions the efficiency of the reaction of $\cdot\text{OH}$ radicals with CH_3OH by hydrogen abstraction from the carbon atom is 93 %. The remaining 7 % is accounted for by the formation of methoxy radicals $\text{CH}_3\text{O}\cdot$. Methoxy radicals are subsequently reacting with methanol producing $\cdot\text{CH}_2\text{OH}$. [157] In the absence of O_2 , the only way to form HCHO from $\cdot\text{CH}_2\text{OH}$ is via electron injection either into the conduction band of TiO_2 or directly into the Pt islands since this radical has reduction potential more negative than that of the conduction band of TiO_2 (see Table 4.2). [37] This dark process is referred to as “current-doubling” in photoelectrochemistry and has been observed in many related systems including the photoanodic oxidation of alcohols on TiO_2 electrodes. [40-42, 158] The injected electron from $\cdot\text{CH}_2\text{OH}$ allows, in principle, the H_2 formation even after the absorption of just one photon. These proposed steps for the photocatalytic H_2 evolution from aqueous methanol solutions over platinized TiO_2 are schematically shown in Figure 4.14. HCHO can be further oxidized in an analogous manner producing HCOOH and finally CO_2 (Eqs. 4.14-4.22). [43, 159-162]

Table 4.2. Potentials of conduction band and valance band of TiO_2 and reduction potentials of some radicals relevant for the mechanisms of methanol photocatalytic oxidation.

Couple	Potential (E/V)	pH	Reference
E_{CB} (anatase)	-0.16	0 (1.0 M H_2SO_4)	[163]
E_{CB} (rutile)	0.04	0 (1.0 M H_2SO_4)	[163]
E_{VB} (anatase and rutile)	3.04 ^a	0 (1.0 M H_2SO_4)	
$\cdot\text{OH}$, $\text{H}^+/\text{H}_2\text{O}$	2.73		[164]
$\cdot\text{OH}/\text{OH}^-$	1.90		[164]
$\cdot\text{CH}_2\text{OH}$, $\text{H}^+/\text{CH}_3\text{OH}$	1.24	3.5	[37]
HCHO , $\text{H}^+/\cdot\text{CH}_2\text{OH}$	-1.18		[164]
$\text{CO}_2^{\cdot-}$, $\text{H}^+/\text{HCO}_2^-$	1.07		[164]
$\text{CO}_2/\text{CO}_2^{\cdot-}$	-1.90	7	[164]

^a calculated from the conduction band potential (given in the table) and the bandgap energy for rutile (3.0 eV) and for anatase (3.2 eV). [163]

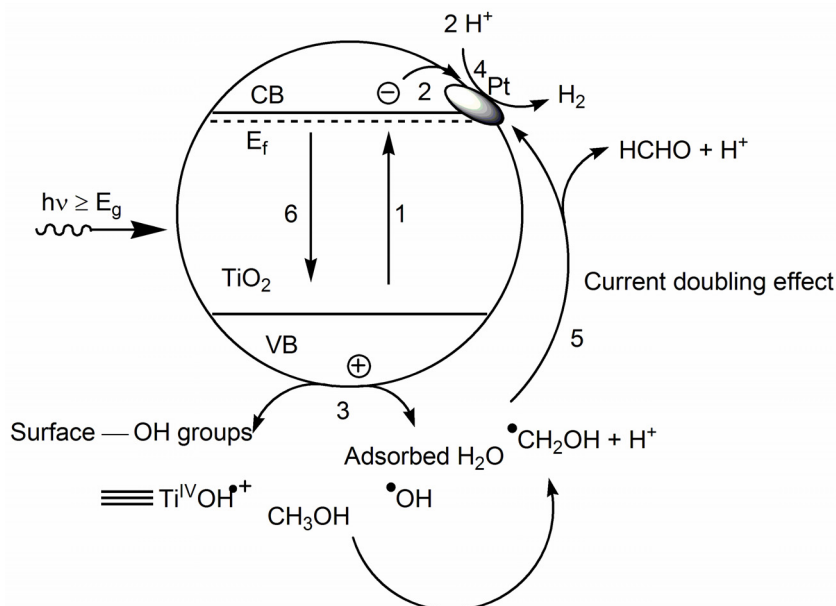


Figure 4.14. Schematic representing the proposed steps for the photocatalytic molecular hydrogen production from aqueous methanol solution, (1) photogeneration of charge carriers, e⁻ and h⁺; (2) trapping of e⁻ by Pt islands; (3) first oxidation step of CH₃OH either by trapped hole or by hydroxyl radical, •OH; (4) reduction of H⁺; (5) formation of HCHO through e⁻ injection into the conduction band of TiO₂ or to the Pt islands (current-doubling); (6) recombination channel.

Methanol is frequently used as an electron donor in so-called “sacrificial systems” for the photocatalytic H₂ production; however, there has been a controversy in the literature about describing this system. Some reports describe the photocatalytic H₂ production from aqueous methanol solutions as water splitting [165-168], while other reports describe the process as dehydrogenation of methanol to formaldehyde or reforming of methanol to carbon dioxide [37, 169]. In this work, the products of the photocatalytic oxidation of methanol have been qualitatively and quantitatively analyzed in order to investigate the balance between the concentration of evolved H₂ and the concentrations of the photooxidation products of methanol. The quantitative analysis of the products following 3 h of illumination employing 0.03 M aqueous methanol solution (2.25 mmol methanol) was performed. The results are given in Table 3.5 (section 3.2.1.1a). The yield of H₂ production is three times higher than the amount of HCHO formed even at different pH values (3.0, 7.0, and 10) (see Table 3.5 second column). Moreover, the molar ratio of the evolved H₂ is about 2.0 times higher than the value calculated from the sum of all CH₃OH oxidation products. Assuming that HCHO, HCOOH, and CO₂ are the only products of the photocatalytic methanol oxidation, the sum of their concentrations should be equivalent to the concentration of evolved H₂. Since this is not observed here it has to be assumed that there are undetected products, e.g., carbonate and

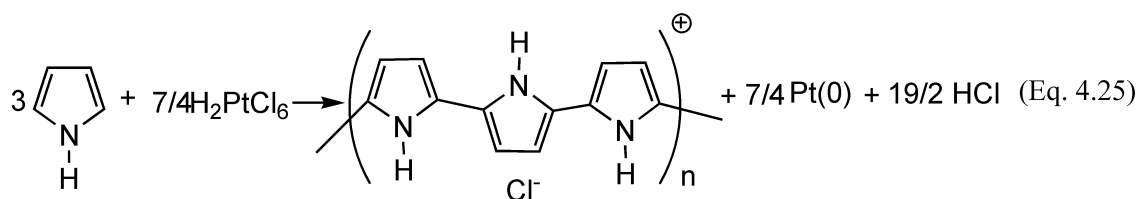
bicarbonate due to the high solubility of CO₂ in water. In an attempt to minimize the amount of secondary and tertiary photooxidation reaction of CH₃OH (e.g., reactions 4.14-4.18, and 4.19-4.22, respectively), the overall balance was tested after a short illumination time (15 min instead of 3 h). In this case, only HCHO was detected and the amount of evolved H₂ matches well the amount of HCHO formed even at different methanol concentrations and different pH values, e.g., 3.0 and 7.0 (see Table 3.5 third column). Unfortunately, the exact source of the protons yielding H₂ cannot be determined from the present study, i.e., it is unclear whether H⁺ originates from water or from CH₃OH. However, these results clearly indicate that methanol only acts as a hole scavenger resulting in equimolar H₂ production.

(b) TiO₂ modified with Pt-polypyrrole nanocomposites

As aforementioned in the previous section, the modification of TiO₂ with Pt nanoparticles is essential for the photocatalytic H₂ evolution. TiO₂ without Pt loading does not exhibit any ability to photocatalyze the H₂ evolution even in the presence of an electron donor, e.g., methanol. Besides Pt, reports have also shown that TiO₂ surfaces modified with conducting polymers such as nafion and polypyrrole have demonstrated enhanced photocatalytic activity for the degradation of organic compounds, e.g., paraquat, methylene blue, and methyl orange [91, 92, 96, 97] and for the production of hydrogen.[93, 94] Other photoelectrochemical studies report the use of polypyrrole coatings to inhibit the photocorrosion of narrow bandgap semiconductors such as n-GaP [170] and CdS.[98] Polypyrrole has the ability to channel the photogenerated holes from the surface of the semiconductor to the polymer/solution interface. Consequently, the role of the polymer is to channel the photogenerated holes to the polymer electrolyte interface at a rate that is much faster than the self-oxidation of the semiconductor.[99] A study performed by Yildiz et al. [95] has shown that the modification of TiO₂ with polypyrrole followed by platinization or platinization followed by modification with polypyrrole in conjunction with bandgap irradiation of TiO₂ decreases the photocatalytic H₂ production when compared to Pt-loaded TiO₂ prepared using a photochemical deposition method.

In this part of work, an attempt has been made to develop a new direct method for the in situ simultaneous modification of TiO₂ P25 with Pt-polypyrrole nanocomposites. The proposed method is simple and depends on the reduction of Pt(IV) to Pt(0) accompanied by the oxidative polymerization of pyrrole monomers at ambient temperature as described in the experimental section (section 2.3.2). The pyrrole monomers undergo oxidative polymerization

in the presence of Pt(IV) under mild aqueous conditions at ambient temperature. This leads to the formation of Pt-polypyrrole nanocomposites according to equation 4.25.[102] If this reaction occurs in suspensions of TiO₂, the Pt-polypyrrole nanocomposites are deposited on the TiO₂ surface. The SEM analysis did not provide any evidence for the presence of individual Pt-polypyrrole nanocomposites in the presence of TiO₂ nanoparticles. Therefore, it is assumed that a smooth thin film of the Pt-polypyrrole nanocomposites coats the TiO₂ nanoparticles.



The modified TiO₂ P25 powder demonstrates photocatalytic H₂ production activity from aqueous methanol solution that is three times higher than that observed for Pt-loaded TiO₂ P25 prepared by a photochemical deposition method (cf. Figure 3.22). Such enhanced photocatalytic activity can be understood by considering the properties of Pt nanoparticles and polypyrrole. As aforementioned, upon photon absorption by TiO₂, an electron/hole pair is generated. Pt islands present on the TiO₂ surface have the ability to trap the photogenerated electrons, [9, 37, 46] while the polypyrrole is assumed to collect and to channel the photogenerated holes to the polymer/solution interface.[98, 99] Combining the properties of the Pt nanoparticles and the polypyrrole, we thus conclude that a synergetic effect between Pt nanoparticles and polypyrrole will promote the charge carrier separation more effectively than the modification of TiO₂ with Pt or polypyrrole alone. Figure 4.15 shows a schematic diagram of the proposed mechanism.

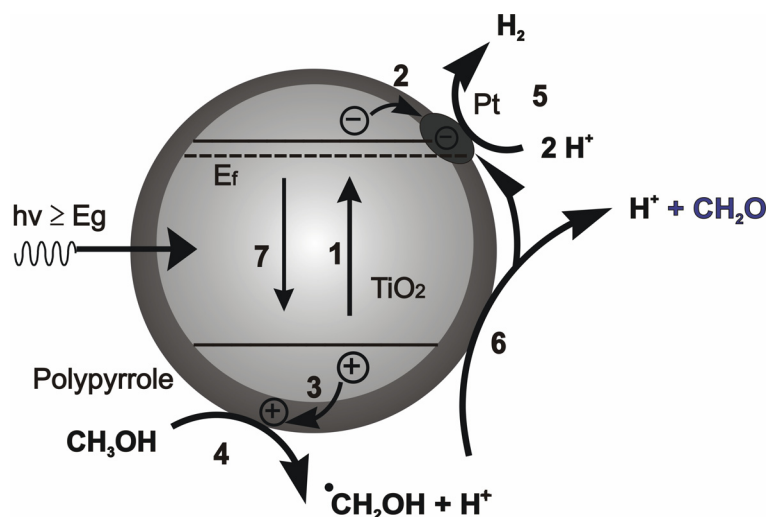


Figure 4.15. Scheme representing the enhanced charge carrier separation and the photocatalytic activity of TiO₂ modified with Pt-polypyrrole nanocomposites, (1) photogeneration of charge carriers, e⁻ and h⁺; (2) trapping of e⁻ by Pt islands; (3) photogenerated holes channelling by polypyrrole to the polymer/solution interface; (4) first oxidation step of CH₃OH; (5) reduction of H⁺; (6) formation of HCHO through e⁻ injection into the conduction band of TiO₂ (current-doubling); (7) recombination channel.

Other factors that could contribute to the enhanced photocatalytic activity are the size of the Pt nanoparticles and the adsorptive properties of the polypyrrole film. The size of Pt nanoparticles prepared via this method is in the range of 1.0 nm as revealed by the DF-STEM measurement (cf. Figure 3.6). However, in the case of photodeposited Pt the average diameter of the Pt nanoparticles was found to be ca. 3.0 nm (cf. Figure 4.12). Generally, the photocatalytic activity increases as the particle size of the deposited noble metal decreases.[9, 171]

Other TiO₂ nanomaterials, e.g., TiO₂ UV100 and TiO₂ P25HT, have also been modified with Pt-polypyrrole nanocomposites via in situ simultaneous reduction of Pt(IV) to Pt(0) accompanied by the oxidative polymerization of pyrrole monomers at ambient temperature. Figure 4.16 shows the time course of the photocatalytic H₂ evolution from 0.03 M aqueous methanol solution (2.25 mmol methanol) over TiO₂ UV100 and TiO₂ P25HT modified with Pt-polypyrrole nanocomposites. For comparison, the time courses of the photocatalytic H₂ evolution over these nanomaterials loaded with Pt nanoparticles via a photochemical deposition method have also been presented.

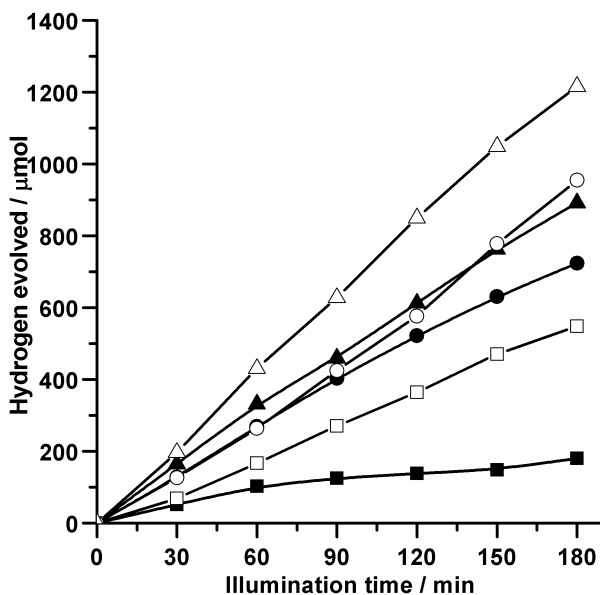


Figure 4.16. Time course of photocatalytic H₂ evolution over modified TiO₂ photocatalysts (■, □) TiO₂ P25, (●, ○) TiO₂ P25HT, and (▲, △) TiO₂ UV100. Solid symbols denote the modification with 0.5 wt% Pt via a photochemical deposition method, whereas open symbols denote the modification with Pt-polypyrrole nanocomposites (0.5 wt% Pt and 1.0 wt% polypyrrole). Conditions: 0.5 g l⁻¹ photocatalysts, 75 ml Ar-saturated aqueous methanol solution (0.03 M, 2.25 mmol methanol), UV-Vis illumination (60 mW cm⁻²).

It is obvious from Figure 4.16 that the TiO₂ nanomaterials modified with Pt-polypyrrole nanocomposites exhibit enhanced photocatalytic activity than those only modified with Pt nanoparticles via the photochemical deposition method. This can be attributed to the synergetic effect between Pt nanoparticles and polypyrrole as previously proposed in Figure 4.15. It is also obvious from Figure 4.16 that the enhancement of the photocatalytic activity in case of TiO₂ P25 is significantly higher than that in case of TiO₂ UV100 and of TiO₂ P25HT. The number of Pt islands per TiO₂ particles can explain this behavior. Assuming Pt nanoparticles that are prepared by reduction with pyrrole monomers are spherical and have a diameter of 1.0 nm (for example see Figure 3.6); the volume of one 1.0 nm Pt nanoparticle is calculated to be 5.23×10^{-22} cm³. Considering the mass density of Pt is 21.4 g cm⁻³, the average weight of one Pt nanoparticle is derived to be approximately 1.12×10^{-20} g. Therefore, the number of Pt islands for each gram of TiO₂ modified with 0.5 wt% Pt and 1.0 wt% polypyrrole was calculated to be 4.46×10^{17} . Assuming spherical TiO₂ nanoparticles with 30 nm average diameter (in case of TiO₂ P25, see Table 3.1) and a mass density of 3.9 g cm⁻³, the number of TiO₂ nanoparticles per gram is calculated to be 1.82×10^{16} . Thus, the number of Pt islands per TiO₂ P25 nanoparticle is calculated to be 25. The number of Pt islands per TiO₂ nanoparticle (TiO₂ UV100 or TiO₂ P25HT) was calculated to be 0.9 assuming a spherical

shape of the TiO₂ nanoparticles with a diameter of 10 nm (see Table 3.1) and a density of 3.9 g cm⁻³. By the same manner, the number of Pt islands prepared via the photochemical deposition method per TiO₂ nanoparticle for TiO₂ P25, TiO₂ UV100, and TiO₂ P25HT is calculated to be 0.9, 0.0337, and 0.0337, respectively, assuming a spherical shape of the Pt islands with a diameter of 3.0 nm (see Figure 4.12).

Combining these data with the fact that TiO₂ P25 is a non-porous material (see Figure 4.10 C), one can expect that the increase of the number of Pt islands per TiO₂ nanoparticle in case of TiO₂ P25 will significantly enhance the photocatalytic activity of H₂ evolution from aqueous methanol solution as compared with the case of TiO₂ UV100 and TiO₂ P25HT that have a much lower number of Pt islands per TiO₂ particle. Since the latter materials have mesoporous structure, it can be imagined that the overlap of the energy bands of the TiO₂ nanoparticles forming this network will result in unified energy bands for the entire system enabling a quasi-free movement of the photogenerated charge carriers throughout (so-called antenna model, discussed in section 4.2.1.1a). Consequently, an electron generated by light absorption within one of the nanoparticles forming the network will subsequently be available to promote redox processes anywhere within the structure. Therefore, a rather small number of Pt islands should still be sufficient to achieve high photocatalytic activity.

(c) Pt-loaded TiO₂ anatase nanoparticles, anatase/brookite mixtures, and brookite nanorods

The results discussed so far are concerning the photocatalytic H₂ evolution over modified TiO₂ nanomaterials which consist either of a biphasial rutile/anatase mixture (TiO₂ P25) or of a pure anatase phase (TiO₂ UV100 and TiO₂ P25HT). It is well known that TiO₂ exists mainly in three crystal phases: anatase (A), rutile (R), and brookite (B). Since most of the synthetic processes produce anatase, rutile or a mixture of them, both phases are readily employed for practical applications and extensively studied as photocatalysts due to the ease of their synthesis. Even most of the commercially available TiO₂ nanomaterials mainly consist of rutile, anatase or a mixture of them. In contrast, the brookite phase is rarely being studied [124, 172-175] mainly due to the difficulties encountered in obtaining its pure form; however, it was reported that brookite nanocrystals have markedly high photocatalytic activities as compared to those of rutile and anatase.[176] Recently, the synthesis of pure brookite TiO₂ with different morphology such as nanorods, nanotubes, and nanoflowers has been reported, [69, 70, 123] but readily tailoring its ratio in the synthesized TiO₂ powders has not been

reported up to date. Moreover, the precursors usually employed in the previously published synthetic processes are TiCl_4 or titanium alkoxides that are very sensitive to moisture and should hence be handled under inert gas and/or the processes suffer from multi reaction steps which might lead to low overall yields of their synthesis.

As a part of this thesis, the synthesis of high quality brookite nanorods has been achieved with the advantage of tailoring the anatase/brookite ratio by a simple hydrothermal method using aqueous solutions of commercially available titanium(IV) bis(ammoniumlactate) dihydroxide (TALH) in the presence of urea as in situ OH^- source (see section 3.1.4). The advantages of using TALH as a TiO_2 precursor are that it is a water soluble complex, and thus does not require an alcohol based solution, and that it is stable at ambient temperature in air, hence eliminating the need of an inert atmosphere during hydrolysis and condensation procedures.

Since the photocatalytic properties of anatase/brookite mixtures and of pure brookite have hardly been studied and little is known concerning their properties, this newly developed synthetic process provides a good opportunity to systematically investigate the relation between the physical properties and the photocatalytic activity of pure anatase, of anatase/brookite mixtures, and of pure brookite.

The photocatalytic activity of anatase nanoparticles, of tailored anatase/brookite mixtures, and of brookite nanorods has been assessed not only by determining the photonic efficiencies of the H_2 production from aqueous methanol solutions but also by determining the photonic efficiencies of the degradation of dichloroacetic acid (DCA) in aqueous solution. As shown in Figure 3.26 (section 3.2.1.1c), the rate of photocatalytic H_2 evolution from aqueous methanol solution (0.03 M, 2.25 mmol methanol) over 0.5 wt% Pt-loaded TiO_2 powders increases with increasing of the brookite content after which it slightly decreases. Pt nanoparticles have been loaded via a photochemical deposition method. To avoid the probability of the change of the particle size of the Pt nanoparticles during the Pt loading, the TiO_2 powders have also been loaded with 0.5 wt% Pt nanoparticles using colloidal Pt suspension. This colloidal Pt suspension has been used to ensure that the difference in the photocatalytic activity can clearly be attributed to the properties of the tested TiO_2 powders.

The photonic efficiencies (ζ) of the photocatalytic H_2 production from aqueous methanol solution (4.93 M, 370 mmol methanol) have been calculated by dividing the rate of H_2 evolution by the photon flux ($\zeta = R/I_0$). The rate of H_2 evolution has been calculated from the slope of the time course of the H_2 production upon UV-Vis illumination (see Figures 3.27 and 3.28). The photon flux has been calculated by employing ferrioxalate actinometry performed

under the same experimental conditions as those used during the rate of H₂ evolution measurements to eliminate any errors associated with the influence of light reflections and reactor geometry. Figure 4.17a shows that the photonic efficiency of the photocatalytic H₂ production increases as the content of the brookite phase in the investigated powders increases, followed by a slight decrease and subsequently a leveling off. The relation between the photonic efficiency and the BET surface area has also been investigated (cf. Figure 4.17b). Surprisingly, as shown in Figure 4.17a and b, there is a reverse dependency between the photonic efficiencies of photocatalytic H₂ production and the BET surface areas of the investigated powders relative to the brookite content. As the brookite content increases in the investigated powders, the photonic efficiency increases despite the simultaneous decrease of the surface area. Thus, the increase in the photonic efficiency can not be explained by a dependence on the BET surface area.

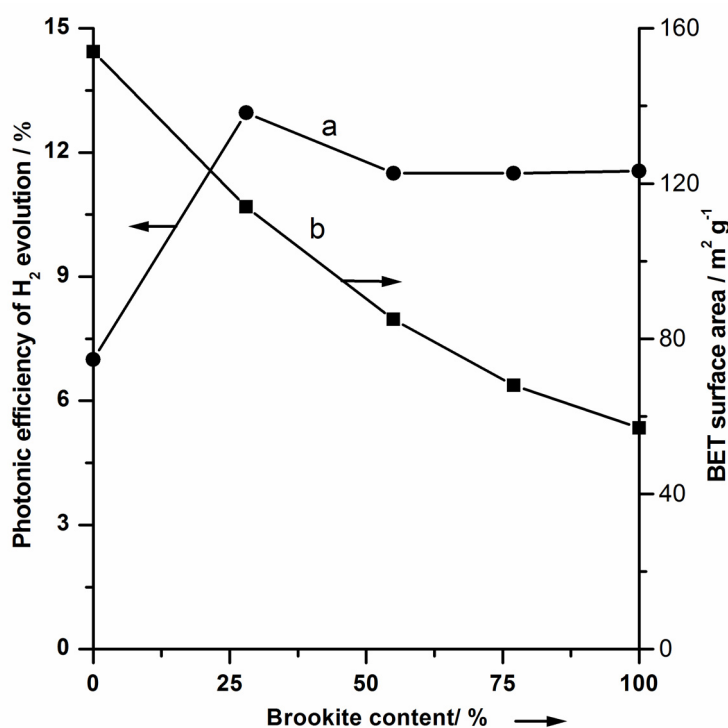


Figure 4.17. Relation between the photonic efficiency, the surface area, and the content of brookite; (●, a) photonic efficiency and (■, b) BET surface area. Conditions: 0.5 g l⁻¹ catalyst, 0.5 wt% Pt (colloidal Pt suspension), 75 ml Ar-saturated aqueous methanol solution (4.93 M, 370 mmol methanol), UG1 Black filter, UV(A) illumination (21.66 μeinstein min⁻¹).

For the TiO₂ powders investigated here, there is no apparent change in the primary particle size for anatase nanoparticles and for brookite nanorods as concluded from the measured crystallite sizes (see Table 3.3). Thus, it becomes obvious that the increased photocatalytic activity of anatase/brookite mixtures and of pure brookite nanorods relative to that of anatase nanoparticles can neither be explained by surface area nor by the primary particle size. However, it seems reasonable that the larger crystallite size of brookite nanorods in comparison with that of the anatase nanoparticles (see Table 3.3) should be regarded as a reason for the increased photocatalytic activity. This large crystallite size might lead to a low density of crystalline defects; hence, it will increase the photocatalytic activity of H₂ evolution from aqueous methanol solution.[177] In fact, the dependence of the photocatalytic activity on the physical properties is indeed very complex. [178] An examination of the flatband potential of the different TiO₂ phases might be also helpful to understand this behavior. In general, the potential of the valance band of titanium dioxide (~ + 3.0 V vs. NHE) is considerably more positive than the potential required for methanol oxidation (+1.24 V vs. NHE).[37] In contrast, the potential of the conduction band electrons in the anatase phase is only positioned by approximately 200 mV more negatively than the potential required for the H₂ evolution, whereas, in case of rutile, it almost coincides with the potential required for the H₂ evolution.[149, 150] Any further cathodic shift of the flatband potential of TiO₂ will therefore favor reduction reactions initiated by the conduction band electrons such as the photocatalytic H₂ production. Thus, the increased photocatalytic activity observed upon the increase of the brookite content might be resulting from a cathodic shift of the flatband potential of the brookite phase as compared with that of the anatase phase. To investigate this assumption experimentally, the flatband potential of both the anatase nanoparticles and the brookite nanorods, has been measured. The flatband potentials of semiconductor electrodes at the semiconductor/electrolyte junction can be obtained from Mott-Schottky plots (measured in the dark) using the following equation (4.26):[179]

$$\frac{1}{C^2} = \frac{2}{\epsilon_{\text{TiO}_2} \cdot \epsilon_0 \cdot e_0 \cdot N_D} \left(E - E_{\text{FB}} - \frac{kT}{e_0} \right) \quad (\text{Eq. 4.26})$$

with ϵ_0 being the permittivity of free space, ϵ_{TiO_2} the permittivity of the semiconductor electrode, e_0 the elementary charge, N_D the donor density, E the applied potential, E_{FB} the flatband potential, k the Boltzmann constant, T the temperature of operation, and C the space charge capacitance.

Plotting $(1/C^2)$ vs. E should thus yield a straight line, intersecting the potential axis at E_{FB} . The Mott-Schottky plots obtained for the anatase nanoparticles and for the brookite nanorods

prepared here are shown in Figure 4.18a and b, respectively. The results indicate that the flatband potential of the anatase nanoparticles is $E_{FB} = -0.35$ V vs. NHE, whereas the flatband potential of the brookite nanorods taken from Figure 4.18b is $E_{FB} = -0.54$ V vs. NHE.

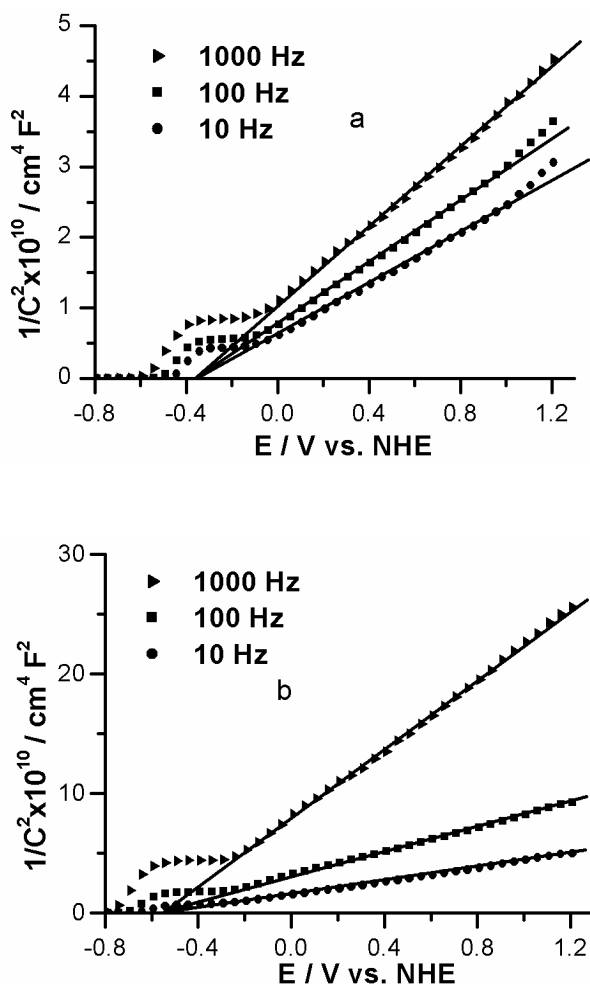


Figure 4.18. Mott-Schottky plots obtained at different frequencies for the TiO_2 film electrodes prepared with (a) anatase nanoparticles and (b) brookite nanorods.

To ensure that the potential of e^-_{CB} in the brookite nanorods is shifted cathodically in comparison with that of the anatase nanoparticles, the quasi-Fermi levels (*E_f) of anatase nanoparticles and brookite nanorods have furthermore been determined under UV(A)-Vis illumination according to the method of Roy et al.[106, 108] Employing this method, the photovoltage of a powder suspension is measured in the presence of a pH-independent redox couple such as methyl viologen dichloride (MV^{2+} , $E_{\text{red}} = -0.445$ V vs. NHE) as a function of the pH value. The *E_f of the anatase nanoparticles and the brookite nanorods have been obtained from the inflection points (pH_0) of the photovoltage–pH curves (cf. Figure 4.19a and

b). The obtained pH_0 values can readily be converted to the quasi-Fermi potentials at pH 7 by the following equation (Eq. 4.27).

$${}^*E_{\text{F}}(\text{pH } 7) = E_{\text{red}} + 0.059(\text{pH}_0 - 7) \quad (4.27)$$

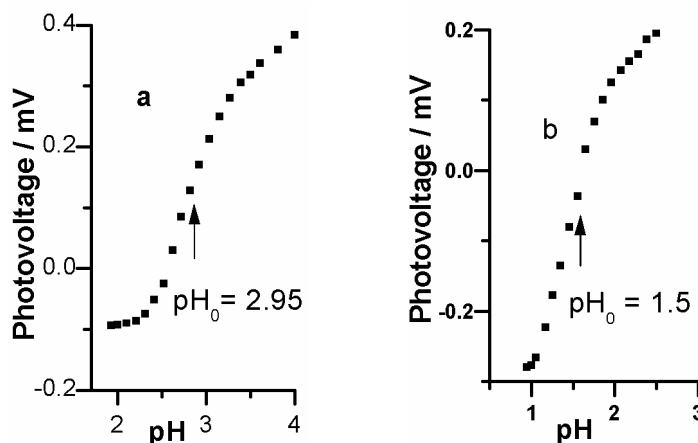


Figure 4.19. Photovoltage vs. suspension pH values measured for (a) anatase nanoparticles and (b) brookite nanorods in 0.1 M KNO_3 in the presence of MV^{2+} .

From the results shown in Figure 4.19 the quasi-Fermi level of the anatase nanoparticles is calculated to be ${}^*E_{\text{f}} = -0.68$ V vs. NHE, whereas the quasi-Fermi level of the brookite nanorods is found to be ${}^*E_{\text{f}} = -0.77$ V vs. NHE. The quasi-Fermi level is found to be more negative than the flatband potential by 0.33 and 0.23 V for anatase nanoparticles and brookite nanorods, respectively. These differences can be explained by the fact that the former was measured under illumination in an aqueous TiO_2 suspension while the latter was measured in the dark employing TiO_2 films. Regardless of this discrepancy, clearly, the results of both independent methods performed under dark and illuminated conditions, respectively, indicate that both the flatband potential and the quasi-Fermi level of brookite nanorods are positioned more cathodically as compared with the respective values of anatase nanoparticles (cf. Table 4.3). Even for the anatase/brookite mixture, the flatband potential and the quasi-Fermi level were found to be more negative than that of the pure anatase nanoparticles (cf. Table 4.3).

Table 4.3. Flatband potentials (E_{FB}), quasi-Fermi levels (*E_f), and calculated conduction band potentials (E_{CB}) of anatase nanoparticles, anatase/brookite mixture (72 % anatase and 28 % brookite), and brookite nanorods.

Nanomaterials	E_{FB} [V vs. NHE]	*E_f [V vs. NHE]	$E_{CB}(\text{calc})$ [V vs. NHE]
Anatase nanoparticles	-0.35	-0.68	-0.51
Anatase/brookite mixture	-0.41	-0.71	-0.56
Brookite nanorods	-0.54	-0.77	-0.65

Assuming that the flatband potential and the quasi-Fermi level are a direct measure of the lower edge of the conduction band, the value of the latter was calculated as the mean value of the former (cf. Table 4.3, fourth column). It is hence concluded that the conduction band of brookite TiO_2 is positioned by about 140 mV more cathodically than that of the anatase phase. As the valence band position of TiO_2 appears to be rather insensitive to the lattice structure,[18] this cathodic shift should reflect an effective increase of the bandgap energy of the brookite phase by 140 mV as compared with that of the anatase phase. To experimentally analyze this assumption, the bandgap energies of both materials have been determined by plotting the modified Kubelka-Munk function $[F(R)E]^{1/2}$ calculated from the optical absorption spectrum vs. the energy of the exciting light E assuming that TiO_2 has an indirect optical transition (Figure 4.20).[103, 104] The intercepts of the straight lines a and b plotted in Figure 4.20 yield bandgap energies of 3.18 eV and 3.31 eV for the anatase nanoparticles and the brookite nanorods, respectively. The difference in bandgap energies of the two nanomaterials of 130 meV coincides extremely well with the cathodic shift of the potential of the e^-_{CB} in the brookite nanorods determined by two completely independent experimental methods. Thus, in the case of the brookite nanorods, the driving force for the proton reduction is higher than that in the case of the anatase nanoparticles. This might also explain why anatase/brookite mixtures and pure brookite nanorods exhibit higher photocatalytic activity for the H_2 evolution from aqueous methanol solution than pure anatase nanoparticles despite of their smaller BET surface area.

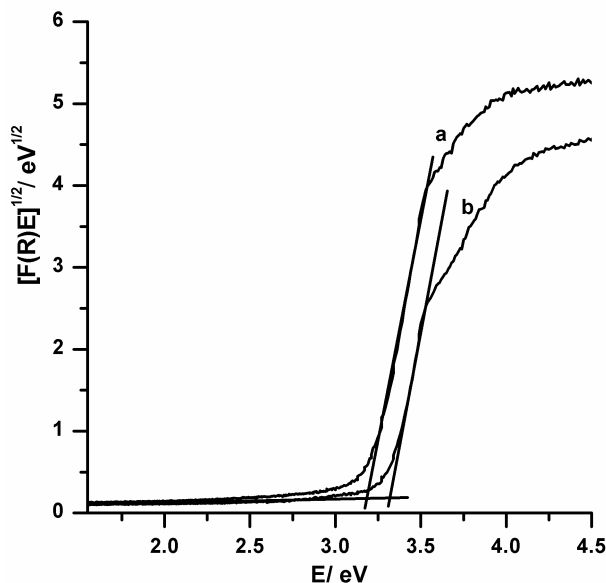


Figure 4.20. Plot of the modified Kubelka-Munk function versus the energy of light absorbed for (a) anatase nanoparticles and (b) brookite nanorods.

In conclusion, the conduction band of brookite TiO_2 is positioned by about 130 to 140 mV more cathodically than that of anatase. In anatase/brookite mixtures, this should facilitate interfacial electron transfer while the resulting energy barrier would suppress back electron transfer. Consequently, the holes left in the valance band of brookite efficiently oxidize organic substrates, while the electrons that have been transferred into the anatase phase are consumed by the reduction of H^+ at the Pt nanoparticles. This will lead to a better charge carrier separation and hence to an increase of the photocatalytic activity similar to that usually assumed for anatase/rutile mixtures.[180-183] This proposed synergistic effect between anatase nanoparticles and brookite nanorods is schematically presented in Figure 4.21.

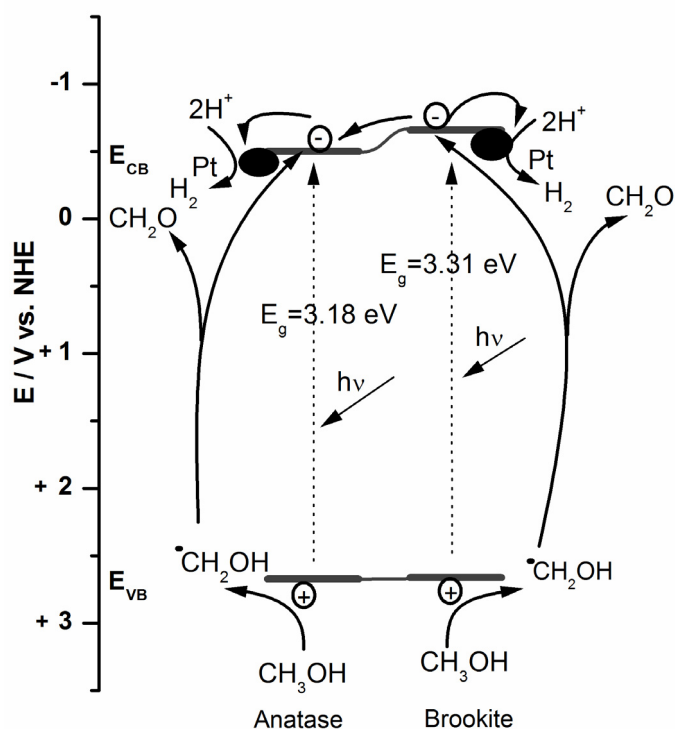


Figure 4.21. Electrochemical potentials (vs. NHE) of band edges of anatase and brookite phases and expected charge carrier transfer events. The recombination channels are not shown.

4.2.1.2. Comparison of the photocatalytic H_2 evolution activities of the different investigated photocatalysts

For a better comparison of the different investigated photocatalysts, the rates and the photonic efficiencies of the photocatalytic H_2 evolution over the different modified TiO_2 nanomaterials from 0.03 M (2.25 mmol methanol) and 4.93 M (370 mmol methanol) aqueous methanol solutions, respectively, are summarized in Tables 4.4 and 4.5, respectively. The anatase/brookite mixture (TiO_2 AB_{1.0,24}), which shows the highest photocatalytic activity among the tailored anatase/brookite nanomaterials, has also been modified with 0.5 wt% Pt and 1.0 wt% polypyrrole employing the same recipe described in section 2.3.2. Thus, the rate and the photonic efficiency of the photocatalytic H_2 evolution over this material have also been measured under the same conditions as for the other photocatalysts.

Table 4.4. Rates of photocatalytic H₂ evolution (R_{H₂}) from aqueous methanol solution (0.03 M, 2.25 mmol methanol) over different 0.5 wt% Pt-loaded TiO₂ nanomaterials under UV(A)-Vis illumination. Light intensity I = 60 mW cm⁻², illuminated area A = 7 cm², calculated photon flux I₀ = 4.42 × 10³ μeinsteins h⁻¹.

Nanomaterials	Modification methods	Anatase (%)	Rutile (%)	Brookite (%)	R _{H₂} (μmol h ⁻¹)	ζ (%)
TiO ₂ P25	photochemical deposition	82	18	-	66	1.5
	Pt-polypyrrole composites				180	4.1
TiO ₂ P25HT	photochemical deposition	100	-	-	252	5.7
	Pt-polypyrrole composites				305	6.9
TiO ₂ UV100	photochemical deposition	100	-	-	303	6.8
	Pt-polypyrrole composites				414	9.4
TiO ₂ A _{0.1,24}	photochemical deposition	100	-	-	153	3.5
TiO ₂ AB _{1.0,24}	photochemical deposition	72	-	28	239	5.4
	Pt-polypyrrole composites				254	5.7
TiO ₂ AB _{1.5,24}	photochemical deposition	45	-	55	227	5.1
TiO ₂ AB _{2.0,24}	photochemical deposition	23	-	77	225	5.1
TiO ₂ B _{6.0,24}	photochemical deposition	-	-	100	220	5.0

Table 4.5. Photonic efficiencies (ζ) of photocatalytic H₂ evolution from aqueous methanol solution (4.93 M, 370 mmol methanol) over different Pt-loaded TiO₂ nanomaterials under UV(A) illumination.

Nanomaterials	Modification methods	R _{H₂} ($\mu\text{mol h}^{-1}$)	I ₀ ($\mu\text{einstein h}^{-1}$)	ζ (%)
TiO ₂ P25	photochemical deposition	140	2700	5.2
			1944	7.5
	Pt-polypyrrole composites colloidal Pt suspension	286	2700	10.6
		75	1300	5.7
TiO ₂ P25HT	photochemical deposition	537	2700	19.9
			1944	20.2
	Pt-polypyrrole composites	440	1944	22.6
TiO ₂ UV100	photochemical deposition	562	2700	20.8
			1944	22.2
	Pt-polypyrrole composites	524	1944	26.9
TiO ₂ A _{0.1,24}	photochemical deposition	260	1944	13.4
	colloidal Pt suspension	92	1300	7.1
TiO ₂ AB _{1.0,24}	photochemical deposition	378	1944	19.4
	Pt-polypyrrole composites	372	1944	19.1
	colloidal Pt suspension	156	1300	12.0
TiO ₂ AB _{1.5,24}	photochemical deposition	336	1944	17.2
	colloidal Pt suspension	150	1300	11.5
TiO ₂ AB _{2.0,24}	photochemical deposition	335	1944	17.2
	colloidal Pt suspension	150	1300	11.5
TiO ₂ B _{6.0,24}	photochemical deposition	335	1944	17.2
	colloidal Pt suspension	151	1300	11.5

From the rates and the photonic efficiency values of the photocatalytic H₂ evolution, which are summarized in Table 4.4 and 4.5, respectively, one can see that TiO₂ UV100 and TiO₂ P25HT exhibit the highest photocatalytic activities. Anatase nanoparticles (TiO₂ P25HT) that are prepared via the hydrothermal treatment of TiO₂ P25 show a comparable photocatalytic activity to that of TiO₂ UV100. In contrast, TiO₂ P25 exhibits the lowest photocatalytic activity. However, its modification with Pt-polypyrrole nanocomposites significantly enhances its photocatalytic activity. Biphasial anatase/brookite mixtures and brookite nanorods exhibit higher photocatalytic activity than pure anatase nanoparticles (TiO₂ A_{0.1,24}) that are prepared employing the same conditions and even they exhibit higher photocatalytic activity than TiO₂ P25. Interestingly, they also show slightly lower photocatalytic activity than TiO₂ UV100 and TiO₂ P25HT; however, they have a significant lower BET surface area than the later. In particular, the anatase/brookite mixture (TiO₂ AB_{1.0,24}) that consists of 72 % anatase and 28 % brookite and is loaded with 0.5 wt% Pt via the photochemical deposition method exhibits a comparable photocatalytic activity to that of TiO₂ UV100 and TiO₂ P25HT. The significantly high photocatalytic activities of anatase/brookite mixtures and of brookite nanorods, despite the fact that they have lower BET surface areas in comparison with TiO₂ UV100 and TiO₂ P25HT, can be explained by the synergistic effect between anatase and brookite nanoparticles and/or by the fact that the conduction band of the brookite phase is positioned by about 140 mV more cathodically than that of anatase (see Table 4.3). This will raise the driving force for the photocatalytic H₂ evolution reaction. TiO₂ UV100 modified with Pt-polypyrrole composites shows significantly higher photocatalytic H₂ evolution activity than the anatase/brookite mixture (TiO₂ AB_{1.0,24}) modified with the same composites. This can be explained in terms of the difference in Pt-polypyrrole dispersity. Pt-polypyrrole might coat TiO₂ UV100 more homogeneously than TiO₂ AB_{1.0,24} due to the fact that the former disperses in water more homogeneously than the later. It is obvious from Tables 4.4 and 4.5 that the modification of the different photocatalysts with Pt-polypyrrole either enhances the photocatalytic H₂ evolution activity in comparison with the modification with Pt alone via the photochemical deposition method and by mixing with colloidal Pt or at least exhibits comparable activity to that of the photocatalysts modified by the photochemical deposition method. This can be explained by the synergetic effect between Pt nanoparticles and polypyrrole as discussed in section 4.2.1.1b or by the difference in Pt particle size, e.g., Pt islands with diameters of 1.0 nm are observed in case of Pt-polypyrrole composites, whereas Pt islands with diameters of approximately 3.0 nm are formed employing the photochemical deposition method.

At this point, it is also important to mention that rutile nanorods either decorated with anatase nanoparticles or pure showed negligibly small photocatalytic H₂ production activities from aqueous methanol solution. It has been reported that TiO₂ has flatband potentials, dependent on the crystalline forms, positioned at -0.16 and 0.04 V vs. NHE at pH = 0 for anatase and rutile TiO₂, respectively.[163] Assuming that the flatband potential is equal to the potential of the conduction band edge of TiO₂, E_{CB}, the potential of the valence band edge, E_{VB}, is readily calculated to be almost constant at 3.04 V vs. NHE at pH = 0 by subtraction of the energy gaps of anatase and rutile (3.2 and 3.0 eV, respectively) from E_{CB}, being independent of the crystalline phase, anatase or rutile. The difference in E_{CB} of 0.2 V between the anatase and the rutile phases might account for the changes in the photocatalytic activities of H₂ evolution depending on the crystalline phase, anatase or rutile. In the latter case, the driving force for the H⁺ reduction will be smaller than in the former. Therefore, it is obvious that the photocatalytic activity of H₂ evolution over anatase TiO₂ is found to be higher than that of rutile. Some studies have shown that reduction of 2H⁺ to H₂ occurred with irradiation of Pt-loaded rutile TiO₂,[8, 184] though in most experiments the flatband potential of a TiO₂ single crystal having a rutile structure was observed at a potential slightly positive with respect to the H⁺/H₂ redox potential.[163] But even in these studies, the H₂ production rates were very small in respect to those observed for anatase.

Depending on the results presented here and after comparing the different TiO₂ modifications, it seems clear that anatase/brookite mixture and brookite TiO₂ are the most suitable materials for the photocatalytic H₂ evolution, however, TiO₂ UV100 that has a pure anatase structure still exhibits the highest photocatalytic activity. Anatase/brookite mixtures and brookite TiO₂ nanomaterials with high BET surface area and mesoporous structure are consequently expected to show very high photocatalytic activities.

4.2.1.3. Photocatalytic degradation of dichloroacetic acid using TiO₂ anatase nanoparticles, anatase/brookite mixtures, and brookite nanorods

Since the photocatalytic properties of anatase/brookite mixtures and of pure brookite have hardly been studied and little is known concerning their properties, their photocatalytic activities have also been assessed by the photocatalytic degradation of dichloroacetic acid (DCA) (see section 3.2.1.2). The resulting photonic efficiencies as well as the BET surface area have been plotted versus the ratio of the brookite content in the investigated powders (cf. Figure 4.22).

As shown in Figure 4.22a, the photonic efficiency of the DCA degradation decreases as the brookite content increases in the investigated powders, in contrast to the behavior observed for the photocatalytic hydrogen evolution from aqueous methanol solutions. Apparently, the dependency of the photonic efficiency of the DCA degradation and of the surface area upon the content of brookite in the investigated photocatalysts exhibit the same trend (cf. Figure 4.22a and b). With increasing brookite content in the investigated powders, both, the photonic efficiency and the BET surface area decrease. Thus, the decrease of the photocatalytic activity in this case can readily be attributed to the decrease of the surface area. It is often assumed that the larger the specific area, and thus the higher the adsorption of the organic molecules, the higher will be the photocatalytic degradation rate. However, the observed differences in photocatalytic activity, in general, cannot be interpreted using only a single property of the photocatalysts. The photonic efficiency of the DCA degradation on TiO₂ P25 has been determined under the same condition and was found to be 4.8 %. These results reveal that pure anatase nanoparticles exhibit slightly higher photonic efficiency than TiO₂ P25 whereas anatase/brookite mixtures and pure brookite have lower photonic efficiencies than TiO₂ P25.

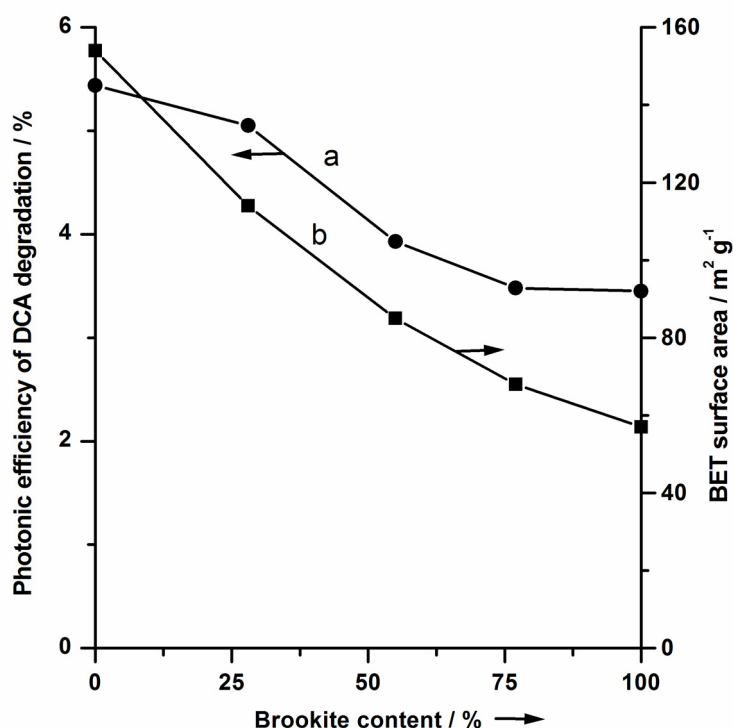
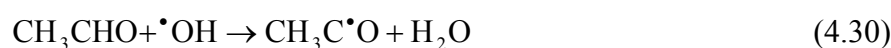
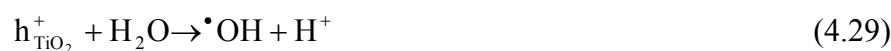


Figure 4.22. Relation between the photonic efficiency, the BET surface area, and the content of brookite; (●, a) photonic efficiency and (■, b) surface area. Conditions: 0.5 g l⁻¹ catalyst, 60 ml aqueous DCA solution (1.0 mM), pH 3.

4.2.2. Gas phase reactions

4.2.2.1. Photocatalytic decomposition of acetaldehyde using TiO₂ rutile nanorods

The photocatalytic activities of rutile nanorods, either decorated with anatase nanoparticles or free of any anatase contact, were evaluated for the gas-phase decomposition of acetaldehyde (see section 3.2.2.1), which is often used as a model compound resembling harmful organic gas. With the rutile bandgap of 3.0 eV (cf. Figure 3.12B), electron-hole pairs can be generated by absorption of UV(A) light with wavelengths below 420 nm (Eq. 4.5). On the film surface the photogenerated holes react with OH⁻ ions or H₂O molecules, yielding highly oxidative hydroxyl [•]OH radicals (Eqs. 4.28 and 4.29), which are the key oxidants in the photocatalytic oxidation process.[11, 185-187] These radicals quickly react with absorbed acetaldehyde, which is further oxidized to acetic acid (Eqs. 4.30-4.34) and finally to carbon dioxide via chain radical reactions.[185, 186] The photogenerated electrons are consumed by adsorbed oxygen molecules to form superoxide radicals and/or hydrogen peroxide (Eqs. 4.35-4.37), which also contribute to the oxidation of acetaldehyde via the intermediate formation of [•]OH radicals (Eq. 4.38). The superoxide radicals and/or hydrogen peroxide can also react with the photogenerated holes mediating a recombination channel (Eqs. 4.39-4.41).



With the illumination area being $A = 30 \text{ cm}^2$ the complete degradation of all incoming acetaldehyde with an initial concentration of 1 ppm, which corresponds to $\Delta \dot{n}_{\text{acetaldehyde}} = 6.76 \times 10^{-10} \text{ mol s}^{-1}$, results in a maximum achievable photonic efficiency ζ_{th} of 0.77 %. Figure 4.23 shows the photonic efficiencies of acetaldehyde decomposition for the different synthesized as well as for commercial rutile TiO_2 nanomaterials. As shown in Figure 4.23, the rutile nanorods decorated with 9 % anatase nanoparticles (RA48) exhibit a higher photocatalytic activity than pure rutile nanorods (R72 and R96) and even a higher activity than the rutile nanorods embedded in 53 % anatase nanoparticles (RA24). Moreover, the photocatalytic activity of RA48 is found to be higher than that of rutile nanoparticles (R25 and R34) and at least comparable to that of TiO_2 P25.

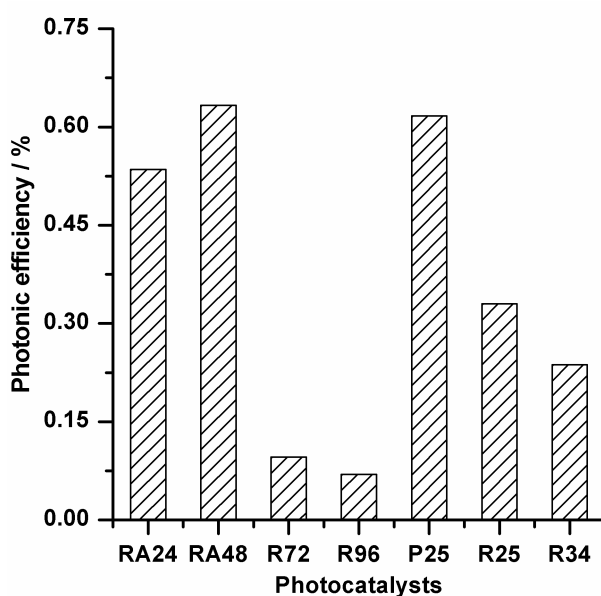


Figure 4.23. Photonic efficiencies of gaseous acetaldehyde decomposition for rutile nanorods embedded in anatase nanoparticles (RA24), rutile nanorods decorated with anatase nanoparticles (RA48), pure rutile nanorods (R72 and R96), TiO_2 P25 (P25), and for commercial rutile nanoparticles (R25 and R34). Conditions: 3.33 mg cm^{-2} photocatalysts, TiO_2 films (30 cm^2), initial acetaldehyde concentration (1.0 ppm), 50 % relative humidity, gas flow (1006 ml min^{-1}), UV(A) illumination (1.0 mW cm^{-2}), ambient temperature ($25 \text{ }^\circ\text{C}$).

The higher photocatalytic activity of rutile nanorods decorated with 9 % anatase nanoparticles (RA48) as compared with that of pure rutile nanorods (R72 and R96) can be explained by the fact that anatase nanoparticles usually exhibit a higher photocatalytic activity than rutile in the case of the acetaldehyde decomposition.[183, 188] Interestingly, the rutile nanorods decorated with only 9 % anatase nanoparticles (RA48) show a higher photocatalytic activity than rutile nanorods embedded in anatase nanoparticles (RA24), whereas the latter

material has a higher content of anatase (53 %). This can be explained by the fact that the conduction band edge of TiO_2 anatase is about 0.2 eV more negative than that of rutile.[163] This is suggested to facilitate interfacial electron transfer, and the energy barrier would suppress back electron transfer. Consequently, the holes left in the valance band of anatase efficiently oxidize the organic substrates, while the electrons having moved to the rutile are consumed by the reduction of oxygen. This will lead to better charge carrier separation and thus to an increase of the photocatalytic activity.[180-182] This charge transfer behavior between anatase and rutile is experimentally supported by photodeposition experiments of Ag [188] in similar structures and has been noted in many systems.[180-183] The slightly lower activity of the rutile nanorods totally covered by anatase nanoparticles as compared with that of the rutile nanorods only decorated with a smaller amount of anatase nanoparticles, however, can be explained by geometric considerations. Due to the complete coverage of the rutile rods by anatase particles, it becomes more difficult for the photogenerated electrons to be scavenged by oxygen molecules because of a blocking effect (i.e., lack of free access of molecular oxygen to the rutile surface) whereas in the case of the rutile nanorods decorated with anatase nanoparticles there is sufficient room enabling free access of molecular oxygen to the rutile surface.

4.2.2.2. Photocatalytic decomposition of acetaldehyde using TiO_2 anatase nanoparticles, anatase/brookite mixtures, and brookite nanorods

The photocatalytic activities of anatase nanoparticles, of anatase/brookite mixtures, and of brookite have also been evaluated by the decomposition of gaseous acetaldehyde (see section 3.2.2.2). Figure 4.24 shows the photonic efficiencies of anatase nanoparticles, of anatase/brookite mixtures, and of brookite nanorods as well as the BET surface area as a function of the brookite ratio in the investigated powders. As shown in Figure 4.24 a and b, both the photonic efficiency and the BET surface area decrease as the brookite content increase in the investigated powders. However, the decrease of the surface area is considerably more significant than that of the photonic efficiency. Thus, one can conclude that the photocatalytic activity over anatase/brookite mixtures and over brookite nanorods does not only depend on the surface area but also on other properties, e.g., the conduction band potential (E_{CB}). In the case of the decomposition of gaseous acetaldehyde, the photogenerated electrons must be scavenged by molecular oxygen at the TiO_2 surface, where reduction of O_2 occurs. Since the conduction band potential of brookite TiO_2 is positioned by

about 140 mV more cathodically than anatase, it is expected that an increase of the brookite content in the investigated powders will raise the driving force for the O₂ reduction, hence increasing the photocatalytic activity of gaseous acetaldehyde decomposition.

The photonic efficiencies of TiO₂ P25, TiO₂ UV100, and TiO₂ P25HT have also been calculated employing the same conditions and are given in Figure 4.25 for comparison with those of the anatase nanoparticles, of anatase/brookite mixtures, and of brookite nanorods. The photonic efficiencies were calculated according to equations 3.1 and 3.3. With the illumination area being $A = 6.25 \text{ cm}^2$ the complete degradation of all incoming acetaldehyde with an initial concentration of 1 ppm, which corresponds to $\Delta \dot{n}_{\text{acetaldehyde}} = 6.76 \times 10^{-10} \text{ mol s}^{-1}$, results in a maximum achievable photonic efficiency ζ_{th} of 3.7 %.

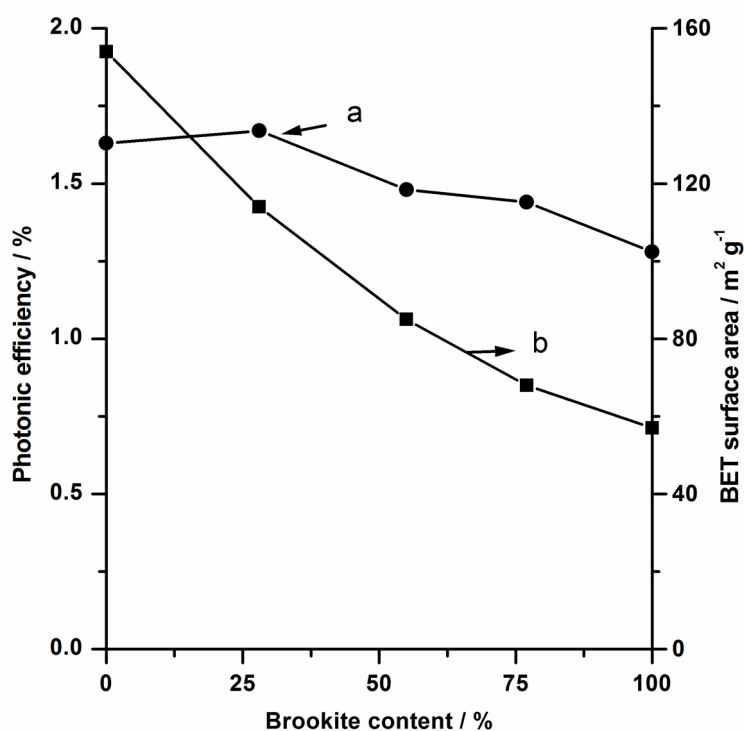


Figure 4.24. Relation between the photonic efficiency of gaseous acetaldehyde decomposition, the BET surface area, and the content of brookite; (●, a) photonic efficiency and (■, b) BET surface area. Conditions: 0.08 g cm⁻² photocatalysts, TiO₂ pellets (6.25 cm²), initial acetaldehyde concentration (1.0 ppm), 50 % relative humidity, gas flow (1006 ml min⁻¹), UV(A) illumination (1.0 mW cm⁻²), ambient temperature (25 °C).

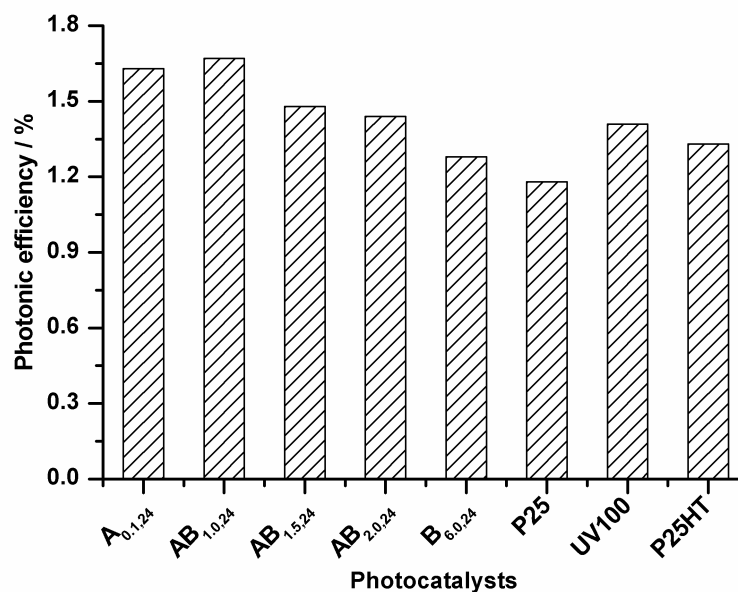


Figure 4.25. Photonic efficiencies of gaseous acetaldehyde decomposition for anatase nanoparticles ($A_{0.1,24}$), anatase/brookite mixtures ($AB_{1.0,24}$, $AB_{1.5,24}$, and $AB_{2.0,24}$), brookite nanorods ($B_{6.0,24}$), TiO_2 P25 (P25), TiO_2 UV100 (UV100), and for TiO_2 P25HT (P25HT). Conditions: 0.08 g cm^{-2} photocatalysts, TiO_2 pellets (6.25 cm^2), initial acetaldehyde concentration (1.0 ppm), 50 % relative humidity, gas flow (1006 ml min^{-1}), UV(A) illumination (1.0 mW cm^{-2}), ambient temperature ($25 \text{ }^\circ\text{C}$).

4.2.2.3. Comparison of the photocatalytic activity of gaseous acetaldehyde decomposition on the different investigated photocatalysts

For comparison of the different investigated nanomaterials, the photonic efficiencies of the gaseous acetaldehyde decomposition on the different nanomaterials are summarized in Table 4.6. Since the illuminated area and the way of TiO_2 surface preparation in case of rutile nanomaterials are different from those in case of tailored anatase/brookite mixtures, the ratio between the photonic efficiencies of the different TiO_2 nanomaterials and TiO_2 P25 were also calculated. The results clearly indicate that anatase nanoparticles (TiO_2 $A_{0.1,24}$) and anatase/brookite mixtures exhibit higher photocatalytic activity than TiO_2 UV100 and TiO_2 P25HT. Rutile nanorods decorated with anatase nanoparticles (R24) also show considerably high photocatalytic activity, but still less than that of anatase/brookite mixtures and less than that of TiO_2 UV100 and TiO_2 P25HT. These results supported the conclusion that brookite phase TiO_2 might have the highest photocatalytic activity among the three TiO_2 phases. Even anatase/brookite mixtures seem to be more preferable than anatase/rutile mixtures.

Table 4.6. Photonic efficiencies (ζ) of gaseous acetaldehyde decomposition under UV(A) illumination as well as the ratio between the photonic efficiency of TiO₂ nanomaterials and that of TiO₂ P25 ($\zeta_{\text{nanomaterials}} / \zeta_{\text{TiO}_2\text{P25}}$).

Nanomaterials	ζ (%)	$\zeta_{\text{nanomaterials}} /$ $\zeta_{\text{TiO}_2\text{P25}}$
TiO ₂ P25	0.617	
R24	0.535	0.87
R48	0.633	1.02
R72	0.096	0.15
R96	0.070	0.11
R25	0.330	0.53
R34	0.237	0.38
TiO ₂ P25	1.18	
TiO ₂ A _{0.1,24}	1.63	1.38
TiO ₂ AB _{1.0,24}	1.67	1.40
TiO ₂ AB _{1.5,24}	1.48	1.25
TiO ₂ AB _{2.0,24}	1.44	1.22
TiO ₂ B _{6.0,24}	1.28	1.08
TiO ₂ UV100	1.41	1.19
TiO ₂ P25HT	1.33	1.13

5. Summary

The starting point of this work was the question whether the photocatalytic H₂ production from aqueous methanol solutions can be described as water splitting. Thus, this reaction over commercial (TiO₂ P25 and TiO₂ UV100) and home made (TiO₂ P25HT) TiO₂ nanomaterials has been extensively studied. The photonic efficiency (ζ) has been calculated by dividing the rate of H₂ evolution by the photon flux ($\zeta = R / I_0$). The effect of light intensity on the reaction rate and on the photonic efficiency of H₂ evolution has been investigated. The products of methanol photocatalytic oxidation have been qualitatively and quantitatively analyzed.

The results revealed that TiO₂ UV100 exhibits a photonic efficiency ($\zeta = 20.8 \%$) that is four times greater than that of TiO₂ P25 ($\zeta = 5.2 \%$) and more or less the same as that of TiO₂ P25HT ($\zeta = 19.9 \%$). These results have been discussed depending on the BET surface area, the structure, and the phase composition of the investigated powders (see section 4.2.1.1a). Studying the effect of the light intensity on the rate of the photocatalytic H₂ evolution indicates that a nonlinear dependency between the light intensity and the rate exists (see Figure 3.21). Deviations from such a linear behavior were observed for both Pt-loaded TiO₂ UV100 and Pt-loaded TiO₂ P25HT. In the case of Pt-loaded TiO₂ P25, the rate of the H₂ evolution increases only initially before it reaches a plateau and remains almost constant upon further increase of the light intensity. Thus, it is of great importance to consider the light intensity when comparing different nanomaterials. For instance, at low light intensity (4.40 $\mu\text{einstein min}^{-1}$) the rate of H₂ evolution over Pt-loaded TiO₂ P25 is similar to that observed for Pt-loaded TiO₂ UV100 and for Pt-loaded TiO₂ P25HT, while, at higher light intensity (44.87 $\mu\text{einstein min}^{-1}$) the rate of H₂ evolution over the latter materials is about four times higher than that measured for Pt-loaded TiO₂ P25. A possible explanation for these differences is that the e^-/h^+ recombination rate constant is higher for Pt-loaded TiO₂ P25 leading to the fact that this undesired reaction channel becomes more significant at high light intensity in case of Pt-loaded TiO₂ P25 as compared with Pt-loaded TiO₂ UV100 and Pt-loaded TiO₂ P25HT.

Qualitative analysis of the photocatalytic methanol oxidation products following different illumination times and working at different pH values employing different methanol concentrations indicates that formaldehyde, formic acid, and carbon dioxide are the only products detected. Based on these detected products, the mechanism of the photocatalytic methanol oxidation has been proposed and the different steps are presented. The quantitative analysis of the photocatalytic methanol oxidation products indicates that following 3 h of

UV(A)-Vis illumination, the yield of H₂ evolved is three times higher than the amount of HCHO formed and about 2.0 times higher than the value calculated from the sum of all methanol photooxidation products (see Table 3.5). This difference can only be explained by the presence of undetected products, e.g., carbonate and bicarbonate due to the high solubility of CO₂ in water. Following 15 min of illumination; however, only HCHO is detected, and the amount of evolved H₂ matches very well the amount of HCHO formed even at different pH values (3.0 and 7.0) and employing different methanol concentrations (0.03 or 4.93 M). These results clearly indicate that methanol only acts as a hole scavenger resulting in equimolar H₂ production. Hence, it seems more likely that this system should be described as a methanol dehydrogenation reaction when it is stopped at the first step of methanol photooxidation (HCHO formation) or as a photocatalytic methanol reforming when CO₂ is detected but not as a real water splitting system. It is also important to mention that no O₂ was detected at all different applied conditions.

Another focus of this thesis was to enhance the efficiency of the photocatalytic H₂ production from aqueous methanol solutions. It is well-known that loading of TiO₂ with Pt nanoparticles is essential for the photocatalytic H₂ production. On the other hand, recent reports showed also that the modification of TiO₂ with organic polymers, e.g., nafion or polypyrrole enhances the photocatalytic activity of TiO₂. Therefore, the modification of the TiO₂ surface with the combination of both, Pt nanoparticles and a polypyrrole polymer, has been investigated. TiO₂ has readily been modified with Pt-polypyrrole nanocomposites by the in situ simultaneous reduction of Pt(IV) and the oxidative polymerization of pyrrole monomers at ambient temperature. The results indicate that 0.5 and 1.0 wt% (in relation to the amount of TiO₂ present) Pt and polypyrrole, respectively, are the optimum loadings to achieve high photocatalytic H₂ production efficiencies (see section 3.2.1.1b). This TiO₂ surface modification greatly enhances the photocatalytic H₂ evolution from aqueous methanol solutions; moreover, the rate of H₂ evolution has been found to be stable without any notable deactivation. A synergetic effect between the Pt nanoparticles and the polypyrrole surface coating, leading to a better charge carrier separation, might explain this enhanced photocatalytic activity. Pt nanoparticles have the ability to trap the photogenerated electrons, while polypyrrole is assumed to have the ability to channel the photogenerated holes to the polymer/solution interface. The Pt nanoparticles produced by this method are in the size range of 1.0 nm, which might also be important to achieve the observed photocatalytic activity enhancement. (see section 4.2.1.1b)

TiO₂ nanomaterials are frequently synthesized via sol-gel methods employing either titanium tetrachloride or titanium alkoxides as starting materials that are, however, very sensitive to moisture and hence need to be handled under inert gas atmospheres. Thus, the synthesis of TiO₂ nanomaterials with the desired morphologies and phase compositions employing aqueous solution still presents a great challenge. Therefore, considerable synthetic efforts have been focused here on the development of alternative synthetic methods to prepare crystalline TiO₂ nanoparticles. In this thesis, TiO₂ rutile nanorods either decorated with anatase nanoparticles or anatase free have thus been prepared via a novel facile one-step hydrothermal method using commercially available aqueous solutions of titanium(IV) bis(ammoniumlactate) dihydroxide (TALH) at natural pH (~ 8.0) without any additives (see section 3.1.3). The photocatalytic H₂ production activity from aqueous methanol solution employing these materials as photocatalysts shows a negligibly small photocatalytic activity. It has been reported that the flatband potential of rutile TiO₂ materials barely coincides with the potential of H₂ evolution or even might be more positive. Hence, the driving force for the H₂ evolution reaction employing rutile TiO₂ will be very small thus explaining the observed low photocatalytic activities of H₂ evolution over the newly prepared TiO₂ rutile nanomaterials. The photocatalytic activities of gaseous acetaldehyde decomposition on these nanomaterials have also been investigated (see section 3.2.2.1). The results indicate that TiO₂ rutile nanorods decorated with anatase nanoparticles exhibit higher photocatalytic activities than those either totally covered by anatase nanoparticles or free from any anatase contact. This is explained by a better charge carrier separation in case of the anatase/rutile mixtures. The slightly lower activity of the rutile nanorods totally covered by anatase nanoparticles as compared with that of the rutile nanorods only decorated with a smaller amount of anatase nanoparticles, on the other hand, can be explained by geometric considerations. In case of a complete coverage of the rutile rods by anatase particles, it becomes more difficult for the photogenerated electrons to be scavenged by molecular oxygen because of a blocking effect (i.e., lack of free access of molecular oxygen to the rutile surface), whereas in the case of the rutile nanorods decorated with anatase nanoparticles there is sufficient room enabling free access of molecular oxygen to the rutile surface.

In addition to the rutile nanomaterials, tailored anatase/brookite mixtures have also been synthesized employing aqueous solutions of the TALH complex in the presence of urea via a facile one step hydrothermal method (see section 3.1.4). High quality brookite nanorods have been obtained by the thermal hydrolysis of aqueous solutions of the TALH complex in the presence of high concentrations of urea (≥ 6.0 M) as an in situ OH⁻ source. Biphasial

anatase/brookite powders are obtained at lower urea concentrations. The ratio between anatase and brookite can readily be tailored by controlling the urea concentration. The photocatalytic activity of pure anatase, of anatase/brookite mixtures, and of pure brookite nanorods has also been assessed by the measurements of the H₂ evolution from aqueous methanol solutions as well as by the degradation of dichloroacetic acid (DCA) in aqueous solution. The results indicate that the photocatalytic H₂ evolution activity of anatase/brookite mixtures and of pure brookite suspensions is higher than that of pure anatase despite the fact that the former exhibit a lower surface area. This behavior is explained by the fact that the flatband potential of the brookite nanorods is cathodically shifted by approx. 140 mV as compared with the flatband potential of the anatase nanoparticles. Moreover, a better charge carrier separation in the case of anatase/brookite mixtures is also envisaged (see section 4.2.1.1c). However, in the case of the photocatalytic degradation of DCA, anatase/brookite mixtures and pure brookite suspensions are photocatalytically less active than anatase nanoparticles alone. This behavior is readily explained by the higher surface area of the latter enabling a better adsorption of DCA molecules on the photocatalysts surfaces. The photocatalytic decomposition of the gaseous acetaldehyde over the tailored anatase/brookite mixtures has also been investigated (see section 3.2.2.2). The results revealed that the anatase/brookite mixtures exhibit higher activity than TiO₂ P25, TiO₂ UV100, and TiO₂ P25HT.

Following the comparison of the photonic efficiencies of the different TiO₂ nanomaterials investigated here (see Table 4.5 and 4.6), it can be concluded that TiO₂ brookite and anatase/brookite mixtures are potentially very suitable photocatalysts for the photocatalytic H₂ evolution. They exhibit higher photocatalytic activity than anatase nanoparticles prepared under the same conditions despite of the higher surface area of the latter. Anatase/brookite mixtures (e.g., 72 % anatase and 28 % brookite) show even a comparable photocatalytic activity to that of the best commercially available materials, TiO₂ UV100, when both are modified with Pt via an identical photochemical deposition method despite the fact that the latter has a 2.6 times larger surface area. Thus, future work focused on the preparation of TiO₂ nanomaterials for photocatalytic H₂ production should consider the preparation of brookite TiO₂ or of anatase/brookite mixtures with high surface area and mesoporous structure. These features are expected to enhance significantly the photocatalytic H₂ production over these materials. Even for the photocatalytic decomposition of gaseous acetaldehyde, anatase/brookite mixtures exhibit higher photocatalytic activities than all investigated TiO₂ nanomaterials including the commercial materials, e.g., TiO₂ P25 and TiO₂ UV100.

6. References

1. Hashimoto, K.; Irie, H.; Fujishima, A. "TiO₂ photocatalysis: a historical overview and future prospects" *Jpn. J. Appl. Phys.*, **2005**, *44*, 8269-8285.
2. Goodeve, C. F.; Kitchener, J. A. "The mechanism of photosensitisation by solids" *Trans. Faraday Soc.*, **1938**, *34*, 902-908.
3. Reference 2 in: Ohtani, B. "Preparing articles on photocatalysis-Beyond the illusions, misconceptions, and speculation" *Chem. Lett.*, **2008**, *37*, 217-229.
4. McLintock, I. S.; Mowbray, R. "Reactions on titanium dioxide; photo-adsorption and oxidation of ethylene and propylene" *Trans. Faraday Soc.*, **1965**, *61*, 1007-1016.
5. Fujishima, A.; Honda, K. "Electrochemical photolysis of water at a semiconductor electrode" *Nature*, **1972**, *238*, 37-38.
6. Ohashi, K.; McCann, J.; Bockris, J. O. M. "Stable photoelectrochemical cells for splitting of water" *Nature*, **1977**, *266*, 610-611.
7. Sato, S.; White, J. M. "Photodecomposition of water over Pt/TiO₂ catalysts" *Chem. Phys. Lett.*, **1980**, *72*, 83-86.
8. Mills, A.; Porter, G. "Photosensitized dissociation of water using dispersed suspensions of n-type semiconductors" *J. Chem. Soc., Faraday Trans. I*, **1982**, *78*, 3659-3669.
9. Kiwi, J.; Grätzel, M. "Optimization of conditions for photochemical water cleavage. Aqueous Pt/TiO₂ (Anatase) dispersions under ultraviolet light" *J. Phys. Chem.*, **1984**, *88*, 1302-1307.
10. Mills, A.; Davies, R. H.; Worsley, D. "Water purification by semiconductor photocatalysis" *Chem. Soc. Rev.*, **1993**, *22*, 417-425.
11. Hoffmann, M. R.; Martin, S. T.; Choi, W. Y.; Bahnemann, D. W. "Environmental applications of semiconductor photocatalysis" *Chem. Rev.*, **1995**, *95*, 69-96.
12. Linsebigler, A. L.; Lu, G. Q.; Yates, J. T. "Photocatalysis on TiO₂ surfaces: principles, mechanisms, and selected results" *Chem. Rev.*, **1995**, *95*, 735-758.
13. Asahi, R.; Morikawa, T.; Ohwaki, T.; Aoki, K.; Taga, Y. "Visible-light photocatalysis in nitrogen-doped titanium oxides" *Science*, **2001**, *293*, 269-271.
14. Fujishima, A.; Rao, T. N.; Tryk, D. A. "Titanium dioxide photocatalysis" *J. Photochem. Photobiol., C: Photochem. Rev.*, **2000**, *1*, 1-21.
15. Fujishima, A.; Zhang, X. T. "Titanium dioxide photocatalysis: present situation and future approaches" *C. R. Chim.*, **2006**, *9*, 750-760.
16. Ni, M.; Leung, M. K. H.; Leung, D. Y. C.; Sumathy, K. "A review and recent developments in photocatalytic water-splitting using TiO₂ for hydrogen production" *Renew. Sust. Energ. Rev.*, **2007**, *11*, 401-425.

17. Osterloh, F. E. "Inorganic materials as catalysts for photochemical splitting of water" *Chem. Mater.*, **2008**, *20*, 35-54.
18. Zhang, H. J.; Chen, G. H.; Bahnemann, D. W. "Photoelectrocatalytic materials for environmental applications" *J. Mater. Chem.*, **2009**, *19*, 5089-5121.
19. Kudo, A.; Miseki, Y. "Heterogeneous photocatalyst materials for water splitting" *Chem. Soc. Rev.*, **2009**, *38*, 253-278.
20. Grätzel, M. "Photoelectrochemical cells" *Nature*, **2001**, *414*, 338-344.
21. Bahnemann, D. "Photocatalytic water treatment: solar energy applications" *Sol. Energy*, **2004**, *77*, 445-459.
22. Herrmann, J. M. "Heterogeneous photocatalysis: fundamentals and applications to the removal of various types of aqueous pollutants" *Catal. Today*, **1999**, *53*, 115-129.
23. Navarro, R. M.; Sanchez-Sanchez, M. C.; Alvarez-Galvan, M. C.; del Valle, F.; Fierro, J. L. G. "Hydrogen production from renewable sources: biomass and photocatalytic opportunities" *Energy Environ. Sci.*, **2009**, *2*, 35-54.
24. Navarro, R. M.; Pena, M. A.; Fierro, J. L. G. "Hydrogen production reactions from carbon feedstocks: fossils fuels and biomass" *Chem. Rev.*, **2007**, *107*, 3952-3991.
25. Hamelinck, C. N.; Faaij, A. P. C. "Future prospects for production of methanol and hydrogen from biomass" *J. Power Sources*, **2002**, *111*, 1-22.
26. Maeda, K.; Domen, K. "New non-oxide photocatalysts designed for overall water splitting under visible light" *J. Phys. Chem. C*, **2007**, *111*, 7851-7861.
27. Meissner, D.; Memming, R.; Kastening, B.; Bahnemann, D. "Fundamental problems of water splitting at cadmium sulfide" *Chem. Phys. Lett.*, **1986**, *127*, 419-423.
28. Yamaguti, K.; Sato, S. "Photolysis of water over metallized powdered titanium dioxide" *J. Chem. Soc., Faraday Trans. I*, **1985**, *81*, 1237-1246.
29. Sayama, K.; Arakawa, H. "Significant effect of carbonate addition on stoichiometric photodecomposition of liquid water into hydrogen and oxygen from platinum-titanium(IV) oxide suspension" *J. Chem. Soc., Chem. Commun.*, **1992**, 150-152.
30. Abe, T.; Suzuki, E.; Nagoshi, K.; Miyashita, K.; Kaneko, M. "Electron source in photoinduced hydrogen production on Pt-supported TiO₂ particles" *J. Phys. Chem. B*, **1999**, *103*, 1119-1123.
31. Kawai, T.; Sakata, T. "Conversion of carbohydrate into hydrogen fuel by a photocatalytic process" *Nature*, **1980**, *286*, 474-476.
32. Kawai, T.; Sakata, T. "Photocatalytic hydrogen production from liquid methanol and water" *J. Chem. Soc., Chem. Commun.*, **1980**, 694-695.

33. Lin, W. C.; Yang, W. D.; Huang, I. L.; Wu, T. S.; Chung, Z. J. "Hydrogen production from methanol/water photocatalytic decomposition using Pt/TiO_{2-x}N_x catalyst" *Energy Fuels*, **2009**, *23*, 2192-2196.
34. Chen, J.; Ollis, D. F.; Rulkens, W. H.; Bruning, H. "Photocatalyzed oxidation of alcohols and organochlorides in the presence of native TiO₂ and metallized TiO₂ suspensions. Part (I): photocatalytic activity and pH influence" *Water Res.*, **1999**, *33*, 661-668.
35. Chen, J.; Ollis, D. F.; Rulkens, W. H.; Bruning, H. "Photocatalyzed oxidation of alcohols and organochlorides in the presence of native TiO₂ and metallized TiO₂ suspensions. Part (II): photocatalytic mechanisms" *Water Res.*, **1999**, *33*, 669-676.
36. Wang, C. Y.; Rabani, J.; Bahnemann, D. W.; Dohrmann, J. K. "Photonic efficiency and quantum yield of formaldehyde formation from methanol in the presence of various TiO₂ photocatalysts" *J. Photochem. Photobiol., A: Chem.*, **2002**, *148*, 169-176.
37. Wang, C. Y.; Pagel, R.; Bahnemann, D. W.; Dohrmann, J. K. "Quantum yield of formaldehyde formation in the presence of colloidal TiO₂-based photocatalysts: effect of intermittent illumination, platinization, and deoxygenation" *J. Phys. Chem. B*, **2004**, *108*, 14082-14092.
38. Wang, C. Y.; Groenzin, H.; Shultz, M. J. "Direct observation of competitive adsorption between methanol and water on TiO₂: an in situ sum-frequency generation study" *J. Am. Chem. Soc.*, **2004**, *126*, 8094-8095.
39. Sun, L. Z.; Bolton, J. R. "Determination of the quantum yield for the photochemical generation of hydroxyl radicals in TiO₂ suspensions" *J. Phys. Chem.*, **1996**, *100*, 4127-4134.
40. Hykaway, N.; Sears, W. M.; Morisaki, H.; Morrison, S. R. "Current-doubling reactions on titanium dioxide photoanodes" *J. Phys. Chem.*, **1986**, *90*, 6663-6667.
41. Memming, R. "Photoinduced charge transfer processes at semiconductor electrodes and particles" *Top. Curr. Chem.*, **1994**, *169*, 105-181.
42. Nogami, G.; Kennedy, J. H. "Investigation of current doubling mechanism of organic compounds by the rotating ring disk electrode technique" *J. Electrochem. Soc.*, **1989**, *136*, 2583-2588.
43. Villarreal, T. L.; Gomez, R.; Neumann-Spallart, M.; Alonso-Vante, N.; Salvador, P. "Semiconductor photooxidation of pollutants dissolved in water: a kinetic model for distinguishing between direct and indirect interfacial hole transfer. I. photoelectrochemical experiments with polycrystalline anatase electrodes under current doubling and absence of recombination" *J. Phys. Chem. B*, **2004**, *108*, 15172-15181.
44. Asmus, K. D.; Möckel, H.; Henglein, A. "Pulse radiolytic study of site of OH[•] radical attack on aliphatic alcohols in aqueous solution" *J. Phys. Chem.*, **1973**, *77*, 1218-1221.
45. Bahnemann, D.; Henglein, A.; Lilie, J.; Spanhel, L. "Flash photolysis observation of the absorption spectra of trapped positive holes and electrons in colloidal TiO₂" *J. Phys. Chem.*, **1984**, *88*, 709-711.

46. Bahnemann, D.; Henglein, A.; Spanhel, L. "Detection of the intermediates of colloidal TiO₂-catalyzed photoreactions" *Faraday Discuss.*, **1984**, *78*, 151-163.
47. Mo, S. D.; Ching, W. Y. "Electronic and optical properties of three phases of titanium dioxide: rutile, anatase, and brookite" *Phys. Rev. B*, **1995**, *51*, 13023-13032.
48. Cromer, D. T.; Herrington, K. "The structures of anatase and rutile" *J. Am. Chem. Soc.*, **1955**, *77*, 4708-4709.
49. Baur, W. H. "Atomabstände und Bindungswinkel im Brookit, TiO₂" *Acta Cryst.*, **1961**, *14*, 214-216.
50. Zhang, H. Z.; Banfield, J. F. "Thermodynamic analysis of phase stability of nanocrystalline titania" *J. Mater. Chem.*, **1998**, *8*, 2073-2076.
51. Zhang, H. Z.; Banfield, J. F. "Understanding polymorphic phase transformation behavior during growth of nanocrystalline aggregates: insights from TiO₂" *J. Phys. Chem. B*, **2000**, *104*, 3481-3487.
52. Finnegan, M. P.; Zhang, H. Z.; Banfield, J. F. "Anatase coarsening kinetics under hydrothermal conditions as a function of pH and temperature" *Chem. Mater.*, **2008**, *20*, 3443-3449.
53. Finnegan, M. P.; Zhang, H. Z.; Banfield, J. F. "Phase stability and transformation in titania nanoparticles in aqueous solutions dominated by surface energy" *J. Phys. Chem. C*, **2007**, *111*, 1962-1968.
54. Saponjic, Z. V.; Dimitrijevic, N. M.; Tiede, D. M.; Goshe, A. J.; Zuo, X. B.; Chen, L. X.; Barnard, A. S.; Zapol, P.; Curtiss, L.; Rajh, T. "Shaping nanometer-scale architecture through surface chemistry" *Adv. Mater.*, **2005**, *17*, 965-971.
55. Barnard, A. S.; Curtiss, L. A. "Prediction of TiO₂ nanoparticle phase and shape transitions controlled by surface chemistry" *Nano Lett.*, **2005**, *5*, 1261-1266.
56. Byrappa, K.; Yoshimura, M. "Handbook of hydrothermal technology" Noyes Publications: Park Ridge, New Jersey, U.S.A, **2001**.
57. Suchanek, W. L.; Riman, R. E. "Hydrothermal synthesis of advanced ceramic powders" *Advances in Science and Technology*, **2006**, *45*, 184-193.
58. Chae, S. Y.; Park, M. K.; Lee, S. K.; Kim, T. Y.; Kim, S. K.; Lee, W. I. "Preparation of size-controlled TiO₂ nanoparticles and derivation of optically transparent photocatalytic films" *Chem. Mater.*, **2003**, *15*, 3326-3331.
59. Aruna, S. T.; Tirosh, S.; Zaban, A. "Nanosize rutile titania particle synthesis via a hydrothermal method without mineralizers" *J. Mater. Chem.*, **2000**, *10*, 2388-2391.
60. Nian, J. N.; Teng, H. S. "Hydrothermal synthesis of single-crystalline anatase TiO₂ nanorods with nanotubes as the precursor" *J. Phys. Chem. B*, **2006**, *110*, 4193-4198.

61. Zhang, Q. H.; Gao, L. "Preparation of oxide nanocrystals with tunable morphologies by the moderate hydrothermal method: insights from rutile TiO₂" *Langmuir*, **2003**, *19*, 967-971.
62. Liu, B.; Aydil, E. S. "Growth of oriented single-crystalline rutile TiO₂ nanorods on transparent conducting substrates for dye-sensitized solar cells" *J. Am. Chem. Soc.*, **2009**, *131*, 3985-3990.
63. Zhang, Y. X.; Li, G. H.; Jin, Y. X.; Zhang, Y.; Zhang, J.; Zhang, L. D. "Hydrothermal synthesis and photoluminescence of TiO₂ nanowires" *Chem. Phys. Lett.*, **2002**, *365*, 300-304.
64. Wei, M. D.; Konishi, Y.; Zhou, H. S.; Sugihara, H.; Arakawa, H. "A simple method to synthesize nanowires titanium dioxide from layered titanate particles" *Chem. Phys. Lett.*, **2004**, *400*, 231-234.
65. Kasuga, T.; Hiramatsu, M.; Hoson, A.; Sekino, T.; Niihara, K. "Formation of titanium oxide nanotube" *Langmuir*, **1998**, *14*, 3160-3163.
66. Kasuga, T.; Hiramatsu, M.; Hoson, A.; Sekino, T.; Niihara, K. "Titania nanotubes prepared by chemical processing" *Adv. Mater.*, **1999**, *11*, 1307-1311.
67. Yang, H. G.; Sun, C. H.; Qiao, S. Z.; Zou, J.; Liu, G.; Smith, S. C.; Cheng, H. M.; Lu, G. Q. "Anatase TiO₂ single crystals with a large percentage of reactive facets" *Nature*, **2008**, *453*, 638-641.
68. Zheng, Y. Q.; Shi, E. W.; Cui, S. X.; Li, W. J.; Hu, X. F. "Hydrothermal preparation of nanosized brookite powders" *J. Am. Ceram. Soc.*, **2000**, *83*, 2634-2636.
69. Zhao, B.; Chen, F.; Huang, Q. W.; Zhang, J. L. "Brookite TiO₂ nanoflowers" *Chem. Commun.*, **2009**, 5115-5117.
70. Deng, Q. X.; Wei, M. D.; Ding, X. K.; Jiang, L. L.; Ye, B. H.; Wei, K. M. "Brookite-type TiO₂ nanotubes" *Chem. Commun.*, **2008**, 3657-3659.
71. Tomita, K.; Petrykin, V.; Kobayashi, M.; Shiro, M.; Yoshimura, M.; Kakihana, M. "A water-soluble titanium complex for the selective synthesis of nanocrystalline brookite, rutile, and anatase by a hydrothermal method" *Angew. Chem., Int. Ed. Engl.*, **2006**, *45*, 2378-2381.
72. Morishina, Y.; Kobayashi, M.; Petrykin, V.; Kakihana, M.; Tomita, K. "Microwave-assisted hydrothermal synthesis of brookite nanoparticles from a water-soluble titanium complex and their photocatalytic activity" *J. Ceram. Soc. Jpn.*, **2007**, *115*, 826-830.
73. Kobayashi, M.; Petrykin, V.; Kakihana, M.; Tomita, K. "Morphology control of rutile nanoparticles in a hydrothermal synthesis from water-soluble titanium complex aqueous solution" *J. Ceram. Soc. Jpn.*, **2007**, *115*, 835-839.
74. Kobayashi, M.; Tomita, K.; Petrykin, V.; Yoshimura, M.; Kakihana, M. "Direct synthesis of brookite-type titanium oxide by hydrothermal method using water-soluble titanium complexes" *J. Mater. Sci.*, **2008**, *43*, 2158-2162.

75. Kobayashi, M.; Petrykin, V.; Kakihana, M.; Tomita, K. "Hydrothermal synthesis and photocatalytic activity of whisker-like rutile-type titanium dioxide" *J. Am. Ceram. Soc.*, **2009**, *92*, S21-S26.
76. Hanprasopwattana, A.; Rieker, T.; Sault, A. G.; Datye, A. K. "Morphology of titania coatings on silica gel" *Catal. Lett.*, **1997**, *45*, 165-175.
77. Baskaran, S.; Song, L.; Liu, J.; Chen, Y. L.; Graff, G. L. "Titanium oxide thin films on organic interfaces through biomimetic processing" *J. Am. Ceram. Soc.*, **1998**, *81*, 401-408.
78. Lee, S. W.; Sigmund, W. M. "Formation of anatase TiO₂ nanoparticles on carbon nanotubes" *Chem. Commun.*, **2003**, 780-781.
79. Lee, S. W.; Drwiega, J.; Wu, C. Y.; Mazyck, D.; Sigmund, W. M. "Anatase TiO₂ nanoparticle coating on barium ferrite using titanium bis-ammonium lactato dihydroxide and its use as a magnetic photocatalys" *Chem. Mater.*, **2004**, *16*, 1160-1164.
80. Caruso, F.; Shi, X. Y.; Caruso, R. A.; Susa, A. "Hollow titania spheres from layered precursor deposition on sacrificial colloidal core particles" *Adv. Mater.*, **2001**, *13*, 740-744.
81. Mayya, K. S.; Gittins, D. I.; Caruso, F. "Gold-titania core-shell nanoparticles by polyelectrolyte complexation with a titania precursor" *Chem. Mater.*, **2001**, *13*, 3833-3836.
82. Shi, X. Y.; Cassagneau, T.; Caruso, F. "Electrostatic interactions between polyelectrolytes and a titania precursor: thin film and solution studies" *Langmuir*, **2002**, *18*, 904-910.
83. Katagiri, K.; Suzuki, T.; Muto, H.; Sakai, M.; Matsuda, A. "Low temperature crystallization of TiO₂ in layer-by-layer assembled thin films formed from water-soluble Ti-complex and polycations" *Colloids Surf., A: Physicochem. Eng. Asp.*, **2008**, *321*, 233-237.
84. Li, X. S.; Fryxell, G. E.; Wang, C.; Engelhard, M. H. "The synthesis of Ag-doped mesoporous TiO₂" *Microporous Mesoporous Mater.*, **2008**, *111*, 639-642.
85. Möckel, H.; Giersig, M.; Willig, F. "Formation of uniform size anatase nanocrystals from bis(ammonium lactato)titanium dihydroxide by thermohydrolysis" *J. Mater. Chem.*, **1999**, *9*, 3051-3056.
86. Bamwenda, G. R.; Tsubota, S.; Nakamura, T.; Haruta, M. "Photoassisted hydrogen production from a water-ethanol solution: a comparison of activities of Au-TiO₂ and Pt-TiO₂" *J. Photochem. Photobiol., A: Chem.*, **1995**, *89*, 177-189.
87. Sreethawong, T.; Yoshikawa, S. "Comparative investigation on photocatalytic hydrogen evolution over Cu-, Pd-, and Au-loaded mesoporous TiO₂ photocatalysts" *Catal. Commun.*, **2005**, *6*, 661-668.

88. Lee, S. L.; Scott, J.; Chiang, K.; Amal, R. "Nanosized metal deposits on titanium dioxide for augmenting gas-phase toluene photooxidation" *J. Nanopart. Res.*, **2009**, *11*, 209-219.
89. Anpo, M.; Takeuchi, M. "The design and development of highly reactive titanium oxide photocatalysts operating under visible light irradiation" *J. Catal.*, **2003**, *216*, 505-516.
90. Subramanian, V.; Wolf, E. E.; Kamat, P. V. "Catalysis with TiO₂/gold nanocomposites. Effect of metal particle size on the fermi level equilibration" *J. Am. Chem. Soc.*, **2004**, *126*, 4943-4950.
91. Vohra, M. S.; Tanaka, K. "Enhanced photocatalytic activity of nafion-coated TiO₂" *Environ. Sci. Technol.*, **2001**, *35*, 411-415.
92. Park, H.; Choi, W. "Photocatalytic reactivities of nafion-coated TiO₂ for the degradation of charged organic compounds under UV or visible light" *J. Phys. Chem. B*, **2005**, *109*, 11667-11674.
93. Park, H.; Choi, W. "Visible-light-sensitized production of hydrogen using perfluorosulfonate polymer-coated TiO₂ nanoparticles: an alternative approach to sensitizer anchoring" *Langmuir*, **2006**, *22*, 2906-2911.
94. Park, H.; Park, Y.; Bae, E.; Choi, W. "Photoactive component-loaded nafion film as a platform of hydrogen generation: alternative utilization of a classical sensitizing system" *J. Photochem. Photobiol., A: Chem.*, **2009**, *203*, 112-118.
95. Yildiz, A.; Sobczynski, A.; Bard, A. J.; Campion, A.; Fox, M. A.; Mallouk, T. E.; Webber, S. E.; White, J. M. "Sensitized polypyrrole-coated semiconducting powders as materials in photosystems for hydrogen generation" *Langmuir*, **1989**, *5*, 148-149.
96. Chowdhury, D.; Paul, A.; Chattopadhyay, A. "Photocatalytic polypyrrole-TiO₂-nanoparticles composite thin film generated at the air-water interface" *Langmuir*, **2005**, *21*, 4123-4128.
97. Wang, D. S.; Wang, Y. H.; Li, X. Y.; Luo, Q. Z.; An, J.; Yue, H. X. "Sunlight photocatalytic activity of polypyrrole-TiO₂ nanocomposites prepared by in situ method" *Catal. Commun.*, **2008**, *9*, 1162-1166.
98. Frank, A. J.; Honda, K. "Polymer-modified electrodes, catalysis and water-splitting reactions" *J. Photochem.*, **1985**, *29*, 195-204.
99. Cooper, G.; Noufi, R.; Frank, A. J.; Nozik, A. J. "Oxygen evolution on tantalum polypyrrole platinum anodes" *Nature*, **1982**, *295*, 578-580.
100. Sato, S. "Photoelectrochemical preparation of Pt/TiO₂ catalysts" *J. Catal.*, **1985**, *92*, 11-16.
101. Abe, R.; Sayama, K.; Sugihara, H. "Development of new photocatalytic water splitting into H₂ and O₂ using two different semiconductor photocatalysts and a shuttle redox mediator IO₃⁻/I⁻" *J. Phys. Chem. B*, **2005**, *109*, 16052-16061.

102. Deki, S.; Nishikawa, H.; Mizuhata, M. "Fabrication of Pt nanoparticles-polypyrrole composite for electrocatalyst" *Electrochemistry*, **2004**, *72*, 415-417.
103. Tauc, J.; Grigorov, R.; Vancu, A. "Optical properties and electronic structure of amorphous germanium" *Phys. Status Solidi*, **1966**, *15*, 627-637.
104. Sakthivel, S.; Janczarek, M.; Kisch, H. "Visible light activity and photoelectrochemical properties of nitrogen-doped TiO₂" *J. Phys. Chem. B*, **2004**, *108*, 19384-19387.
105. Moses, P. R.; Wier, L. M.; Lennox, J. C.; Finklea, H. O.; Lenhard, J. R.; Murray, R. W. "X-ray photoelectron spectroscopy of alkylamine-silanes bound to metal oxide electrodes" *Anal. Chem.*, **1978**, *50*, 576-585.
106. Roy, A. M.; De, G. C.; Sasmal, N.; Bhattacharyya, S. S. "Determination of the flat-band potential of semiconductor particles in suspension by photovoltage measurement" *Int. J. Hydrog. Energy*, **1995**, *20*, 627-630.
107. Gartner, M.; Dremov, V.; Muller, P.; Kisch, H. "Bandgap widening of titania through semiconductor support interactions" *ChemPhysChem*, **2005**, *6*, 714-718.
108. Long, M. C.; Cai, W. M.; Kisch, H. "Visible light induced photoelectrochemical properties of n-BiVO₄ and n-BiVO₄/p-Co₃O₄" *J. Phys. Chem. C*, **2008**, *112*, 548-554.
109. Menendez-Flores, V. M.; Friedmann, D.; Bahnemann, D. W. "Durability of Ag-TiO₂ photocatalysts assessed for the degradation of dichloroacetic acid" *Int. J. Photoenergy*, **2008**, ID 280513.
110. Bahnemann, D.; Bockelmann, D.; Goslich, R. "Mechanistic studies of water detoxification in illuminated TiO₂ suspensions" *Sol. Energy Mater.*, **1991**, *24*, 564-583.
111. Nash, T. "The colorimetric estimation of formaldehyde by means of the hantzsch reaction" *Biochem. J.*, **1953**, *55*, 416-421.
112. Kormann, C.; Bahnemann, D. W.; Hoffmann, M. R. "Photocatalytic Production of H₂O₂ and organic peroxides in aqueous suspensions of TiO₂, ZnO, and desert sand" *Environ. Sci. Technol.*, **1988**, *22*, 798-806.
113. Hatchard, C. G.; Parker, C. A. "A new sensitive chemical actinometer II. Potassium ferrioxalate as a standard chemical actinometer" *Proc. R. Soc. Ser. A*, **1956**, *235*, 518-536.
114. Kirk, A. D.; Namasivayam, C. "Errors in ferrioxalate actinometry" *Anal. Chem.*, **1983**, *55*, 2428-2429.
115. Rabek, J. F. "Experimental methods in photochemistry and photophysics" Part 2, John Wiley & Sons: Chichester, New York, Brisbane, Toronto, Singapore, **1982**.
116. Nishijima, K.; Fujisawa, Y.; Murakami, N.; Tsubota, T.; Ohno, T. "Development of an S-doped titania nanotube (TNT) site-selectively loaded with iron(III) oxide and its photocatalytic activities" *Appl. Catal., B: Environ.*, **2008**, *84*, 584-590.

117. Zhao, M. Q.; Crooks, R. M. "Dendrimer-encapsulated Pt nanoparticles: synthesis, characterization, and applications to catalysis" *Adv. Mater.*, **1999**, *11*, 217-220.
118. Yang, H.; Lu, T. H.; Xue, K. H.; Sun, S. G.; Lu, G. Q.; Chen, S. P. "Electrocatalytic oxidation of methanol on polypyrrole film modified with platinum microparticles" *J. Electrochem. Soc.*, **1997**, *144*, 2302-2307.
119. Selvan, S. T.; Spatz, J. P.; Klok, H. A.; Moller, M. "Gold-polypyrrole core-shell particles in diblock copolymer micelles" *Adv. Mater.*, **1998**, *10*, 132-134.
120. Tian, B.; Zerbi, G. "Lattice dynamics and vibrational spectra of polypyrrole" *J. Chem. Phys.*, **1990**, *92*, 3886-3891.
121. Mendive, C. B.; Bredow, T.; Feldhoff, A.; Blesa, M.; Bahnemann, D. "Adsorption of oxalate on rutile particles in aqueous solutions: a spectroscopic, electron-microscopic and theoretical study" *Phys. Chem. Chem. Phys.*, **2008**, *10*, 1960-1974.
122. Huang, X. P.; Pan, C. X. "Large-scale synthesis of single-crystalline rutile TiO₂ nanorods via a one-step solution route" *J. Cryst. Growth*, **2007**, *306*, 117-122.
123. Buonsanti, R.; Grillo, V.; Carlino, E.; Giannini, C.; Kipp, T.; Cingolani, R.; Cozzoli, P. D. "Nonhydrolytic synthesis of high-quality anisotropically shaped brookite TiO₂ nanocrystals" *J. Am. Chem. Soc.*, **2008**, *130*, 11223-11233.
124. Li, J. G.; Ishigaki, T.; Sun, X. D. "Anatase, brookite, and rutile nanocrystals via redox reactions under mild hydrothermal conditions: phase-selective synthesis and physicochemical properties" *J. Phys. Chem. C*, **2007**, *111*, 4969-4976.
125. Tompsett, G. A.; Bowmaker, G. A.; Cooney, R. P.; Metson, J. B.; Rodgers, K. A.; Seakins, J. M. "The raman spectrum of brookite, TiO₂ (Pbca, Z=8)" *J. Raman Spectrosc.*, **1995**, *26*, 57-62.
126. Fox, M. A.; Worthen, K. L. "Comparison of the physical properties of polypyrrole produced by anodic oxidation and by photoelectrochemical activation of TiO₂" *Chem. Mater.*, **1991**, *3*, 253-257.
127. Lide, D. R. "Handbook of chemistry and physics" 70th ed., CRC Press: Boca Raton, Fla, USA, **1990**.
128. Tsai, C. C.; Teng, H. S. "Structural features of nanotubes synthesized from NaOH treatment on TiO₂ with different post-treatments" *Chem. Mater.*, **2006**, *18*, 367-373.
129. Zhu, H. Y.; Gao, X. P.; Lan, Y.; Song, D. Y.; Xi, Y. X.; Zhao, J. C. "Hydrogen titanate nanofibers covered with anatase nanocrystals: a delicate structure achieved by the wet chemistry reaction of the titanate nanofibers" *J. Am. Chem. Soc.*, **2004**, *126*, 8380-8381.
130. Zhu, H. Y.; Lan, Y.; Gao, X. P.; Ringer, S. P.; Zheng, Z. F.; Song, D. Y.; Zhao, J. C. "Phase transition between nanostructures of titanate and titanium dioxides via simple wet-chemical reactions" *J. Am. Chem. Soc.*, **2005**, *127*, 6730-6736.

131. Yang, J. J.; Jin, Z. S.; Wang, X. D.; Li, W.; Zhang, J. W.; Zhang, S. L.; Guo, X. Y.; Zhang, Z. J. "Study on composition, structure and formation process of nanotube $\text{Na}_2\text{Ti}_2\text{O}_4(\text{OH})_2$ " *Dalton Trans.*, **2003**, 3898-3901.
132. Li, Y. Z.; Fan, Y.; Chen, Y. "A novel method for preparation of nanocrystalline rutile TiO_2 powders by liquid hydrolysis of TiCl_4 " *J. Mater. Chem.*, **2002**, *12*, 1387-1390.
133. Oliver, P. M.; Watson, G. W.; Kelsey, E. T.; Parker, S. C. "Atomistic simulation of the surface structure of the TiO_2 polymorphs rutile and anatase" *J. Mater. Chem.*, **1997**, *7*, 563-568.
134. Diebold, U. "The surface science of titanium dioxide" *Surf. Sci. Rep.*, **2003**, *48*, 53-229.
135. Barnard, A. S.; Zapol, P. "Effects of particle morphology and surface hydrogenation on the phase stability of TiO_2 " *Phys. Rev. B*, **2004**, *70*, 235403.
136. Cozzoli, P. D.; Kornowski, A.; Weller, H. "Low-temperature synthesis of soluble and processable organic-capped anatase TiO_2 nanorods" *J. Am. Chem. Soc.*, **2003**, *125*, 14539-14548.
137. Ribeiro, C.; Vila, C.; Stroppa, D. B.; Mastelaro, V. R.; Bettini, J.; Longo, E.; Leite, E. R. "Anisotropic growth of oxide nanocrystals: insights into the rutile TiO_2 phase" *J. Phys. Chem. C*, **2007**, *111*, 5871-5875.
138. Wang, Y. W.; Zhang, L. Z.; Deng, K. J.; Chen, X. Y.; Zou, Z. G. "Low temperature synthesis and photocatalytic activity of rutile TiO_2 nanorod superstructures" *J. Phys. Chem. C*, **2007**, *111*, 2709-2714.
139. Jiang, Y. H.; Yin, H. B.; Sun, Y. M.; Liu, H.; Lei, L. X.; Chen, K. M.; Wada, Y. J. "Effects of organic acids on the size-controlled synthesis of rutile TiO_2 nanorods" *Appl. Surf. Sci.*, **2007**, *253*, 9277-9282.
140. Kormann, C.; Bahnemann, D. W.; Hoffmann, M. R. "Preparation and characterization of quantum-size titanium dioxide" *J. Phys. Chem.*, **1988**, *92*, 5196-5201.
141. Pena, M.; Meng, X. G.; Korfiatis, G. P.; Jing, C. Y. "Adsorption mechanism of arsenic on nanocrystalline titanium dioxide" *Environ. Sci. Technol.*, **2006**, *40*, 1257-1262.
142. Naicker, P. K.; Cummings, P. T.; Zhang, H. Z.; Banfield, J. F. "Characterization of titanium dioxide nanoparticles using molecular dynamics simulations" *J. Phys. Chem. B*, **2005**, *109*, 15243-15249.
143. Shaw, W. H. R.; Bordeaux, J. J. "The decomposition of urea in aqueous media" *J. Am. Chem. Soc.*, **1955**, *77*, 4729-4733.
144. Lakshminarasimhan, N.; Bae, E.; Choi, W. "Enhanced photocatalytic production of H_2 on mesoporous TiO_2 prepared by template-free method: role of interparticle charge transfer" *J. Phys. Chem. C*, **2007**, *111*, 15244-15250.
145. Lakshminarasimhan, N.; Kim, W.; Choi, W. "Effect of the agglomerated state on the photocatalytic hydrogen production with in situ agglomeration of colloidal TiO_2 nanoparticles" *J. Phys. Chem. C*, **2008**, *112*, 20451-20457.

146. Wang, C. Y.; Pagel, R.; Dohrmann, J. K.; Bahnemann, D. W. "Antenna mechanism and deaggregation concept: novel mechanistic principles for photocatalysis" *C. R. Chim.*, **2006**, *9*, 761-773.
147. Ismail, A. A.; Bahnemann, D. W.; Bannat, I.; Wark, M. "Gold nanoparticles on mesoporous interparticle networks of titanium dioxide nanocrystals for enhanced photonic efficiencies" *J. Phys. Chem. C*, **2009**, *113*, 7429-7435.
148. Ismail, A. A.; Bahnemann, D. W.; Robben, L.; Yarovy, V.; Wark, M. "Palladium doped porous titania photocatalysts: impact of mesoporous order and crystallinity" *Chem. Mater.*, **2010**, *22*, 108-116.
149. Rao, M. V.; Rajeshwar, K.; Paiverneker, V. R.; Dubow, J. "Photosynthetic production of H₂ and H₂O₂ on semiconducting oxide grains in aqueous solutions" *J. Phys. Chem.*, **1980**, *84*, 1987-1991.
150. Karakitsou, K. E.; Verykios, X. E. "Effects of altrivalent cation doping of TiO₂ on its performance as a photocatalyst for water cleavage" *J. Phys. Chem.*, **1993**, *97*, 1184-1189.
151. Kormann, C.; Bahnemann, D. W.; Hoffmann, M. R. "Photolysis of chloroform and other organic molecules in aqueous TiO₂ suspensions" *Environ. Sci. Technol.*, **1991**, *25*, 494-500.
152. Tschirch, J.; Dillert, R.; Bahnemann, D. "Photocatalytic degradation of methylene blue on fixed powder layers: which limitations are to be considered?" *J. Adv. Oxid. Technol.*, **2008**, *11*, 193-198.
153. Goldstein, S.; Behar, D.; Rabani, J. "Mechanism of visible light photocatalytic oxidation of methanol in aerated aqueous suspensions of carbon-doped TiO₂" *J. Phys. Chem. C*, **2008**, *112*, 15134-15139.
154. Goldstein, S.; Behar, D.; Rabani, J. "Nature of the oxidizing species formed upon UV photolysis of C-TiO₂ aqueous suspensions" *J. Phys. Chem. C*, **2009**, *113*, 12489-12494.
155. Gao, R. M.; Stark, J.; Bahnemann, D. W.; Rabani, J. "Quantum yields of hydroxyl radicals in illuminated TiO₂ nanocrystallite layers" *J. Photochem. Photobiol., A: Chem.*, **2002**, *148*, 387-391.
156. Marugan, J.; Hufschmidt, D.; Lopez-Munoz, M. J.; Selzer, V.; Bahnemann, D. "Photonic efficiency for methanol photooxidation and hydroxyl radical generation on silica-supported TiO₂ photocatalysts" *Appl. Catal., B: Environ.*, **2006**, *62*, 201-207.
157. Sonntag, C. V. "Free-radical-induced DNA damage and its repair. A chemical perspective" Springer-Verlag: Berlin, Heidelberg, New York, **2006**.
158. Nosaka, Y.; Sasaki, H.; Norimatsu, K.; Miyama, H. "Effect of surface compound formation on the photoinduced reaction at polycrystalline TiO₂ semiconductor electrodes" *Chem. Phys. Lett.*, **1984**, *105*, 456-458.

159. Burke, L. D.; Oleary, W. A. "Electro-oxidation of formaldehyde at silver anodes-Role of submonolayer hydroxy complexes in noble metal electrocatalysis" *J. Electrochem. Soc.*, **1988**, *135*, 1965-1970.
160. Teoh, W. Y.; Madler, L.; Amal, R. "Inter-relationship between Pt oxidation states on TiO₂ and the photocatalytic mineralisation of organic matters" *J. Catal.*, **2007**, *251*, 271-280.
161. Herrasti, P.; Peter, L. "Photocurrent doubling during the oxidation of formic acid at n-CdS: an investigation by intensity modulated photocurrent spectroscopy" *J. Electroanal. Chem.*, **1991**, *305*, 241-258.
162. Maeda, Y.; Fujishima, A.; Honda, K. "The investigation of current doubling reactions on semiconductor photoelectrodes by temperature change measurements" *J. Electrochem. Soc.*, **1981**, *128*, 1731-1734.
163. Kavan, L.; Grätzel, M.; Gilbert, S. E.; Klemenz, C.; Scheel, H. J. "Electrochemical and photoelectrochemical investigation of single-crystal anatase" *J. Am. Chem. Soc.*, **1996**, *118*, 6716-6723.
164. Wardman, P. "Reduction potentials of one-electron couples involving free radicals in aqueous solution" *J. Phys. Chem. Ref. Data*, **1989**, *18*, 1637-1755.
165. Tang, J. W.; Quan, H. D.; Ye, J. H. "Photocatalytic properties and photoinduced hydrophilicity of surface-fluorinated TiO₂" *Chem. Mater.*, **2007**, *19*, 116-122.
166. Ekamparam, S. "Photoproduction of clean H₂ or O₂ from water using oxide semiconductors in presence of sacrificial reagent" *J. Alloys Compd.*, **2008**, *448*, 238-245.
167. Jitputti, J.; Pavasupree, S.; Suzuki, Y.; Yoshikawa, S. "Synthesis and photocatalytic activity for water-splitting reaction of nanocrystalline mesoporous titania prepared by hydrothermal method" *J. Solid State Chem.*, **2007**, *180*, 1743-1749.
168. Rosseler, O.; Shankar, M. V.; Du, M. K. L.; Schmidlin, L.; Keller, N.; Keller, V. "Solar light photocatalytic hydrogen production from water over Pt and Au/TiO₂ (anatase/rutile) photocatalysts: influence of noble metal and porogen promotion" *J. Catal.*, **2010**, *269*, 179-190.
169. Highfield, J. G.; Chen, M. H.; Nguyen, P. T.; Chen, Z. "Mechanistic investigations of photo-driven processes over TiO₂ by in-situ DRIFTS-MS: part 1. Platinization and methanol reforming" *Energy Environ. Sci.*, **2009**, *2*, 991-1002.
170. Noufi, R. "The incorporation of ruthenium oxide in polypyrrole films and the subsequent photooxidation of water at n-GaP photoelectrode" *J. Electrochem. Soc.*, **1983**, *130*, 2126-2128.
171. Wu, G. P.; Chen, T.; Su, W. G.; Zhou, G. H.; Zong, X.; Lei, Z. B.; Li, C. "H₂ production with ultra-low CO selectivity via photocatalytic reforming of methanol on Au/TiO₂ catalyst" *Int. J. Hydrog. Energy*, **2008**, *33*, 1243-1251.

172. Murakami, N.; Kamai, T.; Tsubota, T.; Ohno, T. "Novel hydrothermal preparation of pure brookite-type titanium(IV) oxide nanocrystal under strong acidic conditions" *Catal. Commun.*, **2009**, *10*, 963-966.
173. Addamo, M.; Bellardita, M.; Di Paola, A.; Palmisano, L. "Preparation and photoactivity of nanostructured anatase, rutile and brookite TiO₂ thin films" *Chem. Commun.*, **2006**, 4943-4945.
174. Di Paola, A.; Addamo, M.; Bellardita, M.; Cazzanelli, E.; Palmisano, L. "Preparation of photocatalytic brookite thin films" *Thin Solid Films*, **2007**, *515*, 3527-3529.
175. Kominami, H.; Ishii, Y.; Kohno, M.; Konishi, S.; Kera, Y.; Ohtani, B. "Nanocrystalline brookite-type titanium(IV) oxide photocatalysts prepared by a solvothermal method: correlation between their physical properties and photocatalytic activities" *Catal. Lett.*, **2003**, *91*, 41-47.
176. Ohtani, B.; Handa, J.; Nishimoto, S.; Kagiya, T. "Highly active semiconductor photocatalyst: extra-fine crystallite of brookite TiO₂ for redox reaction in aqueous propan-2-ol and/or silver sulfate solution" *Chem. Phys. Lett.*, **1985**, *120*, 292-294.
177. Amano, F.; Prieto-Mahaney, O. O.; Terada, Y.; Yasumoto, T.; Shibayama, T.; Ohtani, B. "Decahedral single-crystalline particles of anatase titanium(IV) oxide with high photocatalytic activity" *Chem. Mater.*, **2009**, *21*, 2601-2603.
178. Prieto-Mahaney, O. O.; Murakami, N.; Abe, R.; Ohtani, B. "Correlation between photocatalytic activities and structural and physical properties of titanium(IV) oxide powders" *Chem. Lett.*, **2009**, *38*, 238-239.
179. Baumanis, C.; Bahnemann, D. W. "TiO₂ thin film electrodes: correlation between photocatalytic activity and electrochemical properties" *J. Phys. Chem. C*, **2008**, *112*, 19097-19101.
180. Zachariah, A.; Baiju, K. V.; Shukla, S.; Deepa, K. S.; James, J.; Warriar, K. G. K. "Synergistic effect in photocatalysis as observed for mixed-phase nanocrystalline titania processed via sol-gel solvent mixing and calcination" *J. Phys. Chem. C*, **2008**, *112*, 11345-11356.
181. Li, G. H.; Ciston, S.; Saponjic, Z. V.; Chen, L.; Dimitrijevic, N. M.; Rajh, T.; Gray, K. A. "Synthesizing mixed-phase TiO₂ nanocomposites using a hydrothermal method for photo-oxidation and photoreduction applications" *J. Catal.*, **2008**, *253*, 105-110.
182. Miyagi, T.; Kamei, M.; Mitsuhashi, T.; Ishigaki, T.; Yamazaki, A. "Charge separation at the rutile/anatase interface: a dominant factor of photocatalytic activity" *Chem. Phys. Lett.*, **2004**, *390*, 399-402.
183. Liu, Z. Y.; Zhang, X. T.; Nishimoto, S.; Jin, M.; Tryk, D. A.; Murakami, T.; Fujishima, A. "Anatase TiO₂ nanoparticles on rutile TiO₂ nanorods: a heterogeneous nanostructure via layer-by-layer assembly" *Langmuir*, **2007**, *23*, 10916-10919.
184. Nishimoto, S. I.; Ohtani, B.; Kagiya, T. "Photocatalytic dehydrogenation of aliphatic alcohols by aqueous suspensions of platinumized titanium dioxide" *J. Chem. Soc., Faraday Trans. I*, **1985**, *81*, 2467-2474.

185. Sopyan, I.; Watanabe, M.; Murasawa, S.; Hashimoto, K.; Fujishima, A. "An efficient TiO₂ thin-film photocatalyst: photocatalytic properties in gas-phase acetaldehyde degradation" *J. Photochem. Photobiol., A: Chem.*, **1996**, *98*, 79-86.
186. Ohko, Y.; Tryk, D. A.; Hashimoto, K.; Fujishima, A. "Autooxidation of acetaldehyde initiated by TiO₂ photocatalysis under weak UV illumination" *J. Phys. Chem. B*, **1998**, *102*, 2699-2704.
187. Kim, H.; Choi, W. "Effects of surface fluorination of TiO₂ on photocatalytic oxidation of gaseous acetaldehyde" *Appl. Catal., B: Environ.*, **2007**, *69*, 127-132.
188. Kawahara, T.; Konishi, Y.; Tada, H.; Tohge, N.; Nishii, J.; Ito, S. "A patterned TiO₂(anatase)/TiO₂(rutile) bilayer-type photocatalyst: effect of the anatase/rutile junction on the photocatalytic activity" *Angew. Chem., Int. Ed. Engl.*, **2002**, *41*, 2811-2813.

7. Appendix

7.1. List of abbreviations and symbols

A	Electron acceptor
A	Anatase
A	Illuminated area
a.u.	Arbitrary units
B	Brookite
BET	Brunauer-Emmett-Teller
c	Concentration
C	Space charge capacitance
CB	Conduction band
cf.	Latin: confer (English: compare)
cm	Centimeter
c_0	Initial concentration
D	Electron donor
DCA	Dichloroacetic acid
DF-STEM	Dark-field scanning transmission electron microscopy
E	Electron energy
E	Light energy
E	Applied voltage or potential
et al.	Latin: et alii (English: and others)
eV	Electron volt
E_{CB}	Conduction band potential
E_{FB}	Flatband potential
E_f	Fermi level energy
*E_f	Quasi Fermi level
E_g	Bandgap energy
E_{red}	Standard redox potential
e.g.	Latin: exempli gratia (English: for example)
e_{CB}^-	Conduction band electron
e_0	Elementary charge
FE-SEM	Field-emission scanning electron microscopy
FTO	Fluorine doped tin oxide
F(R)	Kubelka-Munk function

g	Gram
GC	Gas chromatograph
h	Planck constant
h	Hour
HR-TEM	High-resolution transmission electron microscopy
h_{VB}^+	Valence band hole
I	Light intensity
IR	Infrared spectra
i.e.	Latin: id est (English: that is)
I_0	Photon flux
k	Rate constant
k	Boltzmann constant
K	Equilibrium constant
K	Kelvin
kV	Kilovolt
l	Liter
M	Molar (moles per liter)
mM	Millimolar (millimoles per liter)
mg	Milligram
mol	Mole
mmol	Millimole
$M\Omega$	Megaohm
MPa	Megapascal
ml	Milliliter
mW	Milliwatt
NHE	Normal hydrogen electrode
nm	Nanometer
N_A	Avogadro's number
OD	Optical density
P	Pressure
R	Rutile
R_{H_2}	Rate of H_2 evolution
SE	Secondary electron
SMR	Steam methane reforming
T	Temperature

TALH	Titanium(IV) bis(ammoniumlactato) dihydroxide
TCD	Thermal conductivity detector
TEM	Transmission electron microscopy
TOC	Total organic carbon
V	Volt
V	Volume
VB	Valence band
UV	Ultraviolet light
UV(A)	Ultraviolet light in the range from 315 nm to 380 nm
UV-Vis	Ultraviolet and visible light
W	Watt
Wt%	Weight percentage
XPS	X-ray photoelectron spectroscopy
XRD	X-ray diffraction
$\Delta \dot{n}_{\text{acetaldehyde}}$	Difference between inlet and outlet flux of acetaldehyde
ϵ_0	Permittivity of free space
ϵ_{TiO_2}	Permittivity of TiO ₂ electrode
ζ	Photonic efficiency
λ	Wavelength
μmol	Micromole
ν	Frequency
Å	Ångström
°C	Degree celsius

7.2. List of tables

Table 1.1. Selected applications of photocatalysis.[14, 15]	2
Table 1.2. Crystal structure data of TiO ₂ . [47]	14
Table 1.3. Summary of titanium dioxide coatings and composites products prepared employing the titanium(IV) bis(ammoniumlactato) dihydroxide complex as a titanium source.	20
Table 2.1. Suppliers and denotation of the commercial titanium dioxide powders and precursors.	25
Table 2.2. Denotation of anatase nanoparticles, anatase/brookite mixtures, and brookite nanorods obtained by thermal hydrolysis of TALH complex employing different urea concentrations and different reaction times.	27
Table 3.1. Quantitative phase composition, crystallite sizes, and BET surface area of bare and Pt-loaded TiO ₂ nanomaterials.	39
Table 3.2. Quantitative phase composition, crystallite sizes, BET surface area, and yield of nanocrystalline TiO ₂ prepared by thermal hydrolysis of the TALH precursor at 200 °C and the pH at the end of the experimental run.	44
Table 3.3. Quantitative phase composition and crystallite sizes of nanocrystalline TiO ₂ prepared by thermal hydrolysis of the TALH precursor at 160 °C for 24 h in the presence of different concentrations of urea.	50
Table 3.4. Light intensities and photon flux values measured by UV-meter and ferrioxalate actinometry, respectively. Conditions: UG1 black filter, neutral density filters, 75 ml aqueous potassium ferrioxalate complex solution (0.15 M) in 0.05 M H ₂ SO ₄	56
Table 3.5. Quantitative analysis of methanol photocatalytic oxidation products over 0.5 wt% Pt-loaded TiO ₂ UV100 at different reaction times, pH values, and methanol concentrations.	58
Table 3.6. Rates (R _{H₂}) and photonic efficiencies (ζ) of the photocatalytic H ₂ evolution from aqueous methanol solutions (4.93 M, 370 mmol methanol) over Pt-loaded anatase nanoparticles, anatase/brookite mixtures, and brookite nanorods as well as the respective BET surface areas. Conditions: 0.5 wt% Pt (photochemical deposition method), photon flux I ₀ = 1944 μeinstein h ⁻¹	64
Table 3.7. Rates (R _{H₂}) and photonic efficiencies (ζ) of the photocatalytic H ₂ evolution from aqueous methanol solutions (4.93 M, 370 mmol methanol) over Pt-loaded anatase nanoparticles, anatase/brookite mixtures, and brookite nanorods as well as the respective BET surface areas. Conditions: 0.5 wt% Pt (colloidal Pt suspensions), photon flux I ₀ = 1300 μeinstein h ⁻¹	65
Table 3.8. Initial rates (R _i) and photonic efficiencies (ζ) of photocatalytic DCA degradation on anatase nanoparticles, anatase/brookite mixtures, and brookite nanorods as well as the respective BET surface areas. Conditions: 0.5 g l ⁻¹ catalysts, incident photon flux per volumetric unit = 3.31 x 10 ⁻² einstein l ⁻¹ h ⁻¹	67

Table 3.9. Rates ($\Delta\dot{n}_{\text{acetaldehyde}}$) and photonic efficiencies (ζ) of the photocatalytic decomposition of gaseous acetaldehyde on rutile nanorods decorated with anatase nanoparticles and on pure rutile nanorods as well as the respective BET surface areas. Conditions: 3.33 mg cm ⁻² photocatalysts, TiO ₂ films (30 cm ²), initial acetaldehyde concentration (1.0 ppm), 50 % relative humidity, gas flow (1006 ml min ⁻¹), UV(A) illumination (I = 1.0 mW cm ⁻² , I ₀ = 2.93×10 ⁻⁹ einstein s ⁻¹ cm ⁻²), ambient temperature (25 °C).	69
Table 3.10. Rates ($\Delta\dot{n}_{\text{acetaldehyde}}$) and photonic efficiencies (ζ) of the photocatalytic decomposition of gaseous acetaldehyde on anatase nanoparticles, on anatase/brookite mixtures, and on brookite nanorods as well as the respective BET surface areas. Conditions: 0.08 g cm ⁻² photocatalysts, TiO ₂ pellets (6.25 cm ²), initial acetaldehyde concentration (1.0 ppm), 50 % relative humidity, gas flow (1006 ml min ⁻¹), UV(A) illumination (I = 1.0 mW cm ⁻² , I ₀ = 2.93×10 ⁻⁹ einstein s ⁻¹ cm ⁻²), ambient temperature (25 °C).	70
Table 4.1. Quantitative phase composition and crystallite sizes of nanocrystalline TiO ₂ prepared by thermal hydrolysis of the TALH precursor at different reaction times and temperatures in the presence of 1.0 M of urea.	80
Table 4.2. Potentials of conduction band and valance band of TiO ₂ and reduction potentials of some radicals relevant for the mechanisms of methanol photocatalytic oxidation.....	91
Table 4.3. Flatband potentials (E _{FB}), quasi-Fermi levels (*E _f), and calculated conduction band potentials (E _{CB}) of anatase nanoparticles, anatase/brookite mixture (72 % anatase and 28 % brookite), and brookite nanorods.	103
Table 4.4. Rates of photocatalytic H ₂ evolution (R _{H₂}) from aqueous methanol solution (0.03 M, 2.25 mmol methanol) over different 0.5 wt% Pt-loaded TiO ₂ nanomaterials under UV(A)-Vis illumination. Light intensity I = 60 mW cm ⁻² , illuminated area A = 7 cm ² , calculated photon flux I ₀ = 4.42×10 ³ μeinstein h ⁻¹	106
Table 4.5. Photonic efficiencies (ζ) of photocatalytic H ₂ evolution from aqueous methanol solution (4.93 M, 370 mmol methanol) over different Pt-loaded TiO ₂ nanomaterials under UV(A) illumination.....	107
Table 4.6. Photonic efficiencies (ζ) of gaseous acetaldehyde decomposition under UV(A) illumination as well as the ratio between the photonic efficiency of TiO ₂ nanomaterials and that of TiO ₂ P25 ($\zeta_{\text{nanomaterials}} / \zeta_{\text{TiO}_2\text{P25}}$).	116

7.3. List of figures

Figure 1.1. Principle mechanism of photocatalysis and superposition of the energy band diagram with the geometrical image of a spherical TiO ₂ particle. Note: for simplicity, the indirect oxidation of electron donor (D) by trapped holes ($\equiv\text{Ti}^{\text{IV}}\text{OH}^{\bullet+}$) or by $\cdot\text{OH}$ radicals is represented by the hole oxidation step.	4
Figure 1.2. Basic principle of overall water splitting on a heterogeneous photocatalyst.[26] ...	7
Figure 1.3. Relationship between band structure of a semiconductor and redox potentials of water splitting.[19]	7

Figure 1.4. Processes involved in the overall photocatalytic water splitting on a heterogeneous photocatalyst.[26].....	9
Figure 1.5. Photoelectrochemical water splitting using a rutile TiO ₂ photoelectrode.[19].....	10
Figure 1.6. Processes involved in photocatalytic H ₂ evolution from aqueous methanol solution on (a) bare TiO ₂ and (b) on Pt-loaded TiO ₂ . (1) photogeneration of charge carriers, e ⁻ and h ⁺ ; (2) trapping of e ⁻ by Ti ⁴⁺ (a) or by Pt islands (b); (3) first oxidation step of CH ₃ OH; (4) formation of HCHO through e ⁻ injection into the conduction band of TiO ₂ (current-doubling); (5) formation of Ti ³⁺ (a) or reduction of H ⁺ (b); (6) recombination channel. Note: For simplicity, the formation of [•] CH ₂ OH radicals by trapped holes (≡Ti ^{IV} OH ^{•+}) or by [•] OH radicals is represented by the hole oxidation step.	13
Figure 1.7. Crystal structures of TiO ₂ (a) rutile, (b) anatase, and (c) brookite. [47].....	14
Figure 1.8. (a) Assumed molecular structure of the ionized form of TALH, (b) assumed molecular structure of the non-ionized form of TALH [85]. Arrows indicate donated electron pairs.	21
Figure 1.9. Principle mechanism of photocatalytic process occurring at Pt-loaded spherical TiO ₂ particles. (1) photogeneration of charge carriers, e ⁻ and h ⁺ ; (2) trapping of e ⁻ at Pt islands (b); (3) first oxidation step of electron donor; (4) reduction of electron acceptor; (5) recombination channel. Note: for simplicity, the first oxidation step by trapped holes (≡Ti ^{IV} OH ^{•+}) or by [•] OH radicals is represented by the hole oxidation step.	22
Figure 1.10. Conceptual model for the suppression of the photodegradation of a n-type semiconductor and the promotion of the water oxidation reaction.[98].....	23
Figure 2.1. Schematic presentation of the experimental setup employed for the quasi-Fermi level potential determination: 1- working electrode (Pt), 2- reference electrode (Ag/AgCl), 3- pH meter electrode, 4- N ₂ gas sparger, 5- catalyst suspension, 6- magnetic stirring bar, 7- multimeter.	32
Figure 2.2. Schematic presentation of the water cooled reactor used to assess the photocatalytic production of H ₂	33
Figure 2.3. Real image for the experimental setup used for the photocatalytic degradation of dichloroacetic acid (DCA).	34
Figure 2.4. Real image for the experimental setup used for the photocatalytic decomposition of acetaldehyde.	35
Figure 3.1. XRD diffraction patterns of (a) TiO ₂ P25, (b) TiO ₂ P25 after hydrothermal treatment without calcination (titanate), and (c) TiO ₂ P25 after hydrothermal treatment and calcination at 400 °C for 2 h (TiO ₂ P25HT). Labels A and R indicate Bragg positions for anatase and rutile, respectively.	38
Figure 3.2. XRD diffraction patterns of 0.5 wt% Pt-loaded TiO ₂ nanomaterials, (a) TiO ₂ P25HT, (b) TiO ₂ UV100, and (c) TiO ₂ P25. Labels A and R indicate Bragg positions for anatase and rutile, respectively.	39
Figure 3.3. FE-SEM micrographs of TiO ₂ P25 (a) before and (b) after hydrothermal treatment.	40
Figure 3.4. HR-TEM micrographs: (a) TiO ₂ P25 and (b) TiO ₂ P25HT.	41
Figure 3.5. XPS spectra of TiO ₂ modified with Pt-polypyrrole nanocomposites (1.0 wt% Pt and 1.0 wt% polypyrrole). The inset shows the Pt 4f peaks.	42

- Figure 3.6. DF-STEM image of TiO₂ modified with 0.5 wt% Pt and 1.0 wt% polypyrrole nanocomposites. Pt is seen as bright points with diameter of about 1.0 nm (see arrows). 43
- Figure 3.7. IR spectra of (a) TiO₂ modified with Pt-polypyrrole nanocomposites as prepared, (b) pyrrole monomers, (c) Pt-loaded TiO₂ prepared by a photochemical deposition method, (d) Pt-polypyrrole nanocomposites, (e) and (f) TiO₂ modified with Pt-polypyrrole nanocomposites following 20 and 100 h of illumination, respectively..... 43
- Figure 3.8. XRD patterns of as-synthesized nanocrystalline TiO₂ powders obtained by thermal hydrolysis of aqueous solutions of the TALH precursor at 200 °C for (a) 24 h, (b) 48 h, (c) 72 h, and (h) 96 h. Labels R and A indicate Bragg positions for rutile and anatase, respectively. 44
- Figure 3.9. FE-SEM micrographs of as-synthesized nanocrystalline TiO₂ powders obtained by thermal hydrolysis of aqueous solutions of the TALH precursor at 200 °C for (a) 24 h, (b) 48 h, (c) 72 h, and (d) 96 h. 45
- Figure 3.10. High-resolution transmission electron micrographs of as-synthesized nanocrystalline TiO₂ powder obtained by thermal hydrolysis of aqueous solutions of the TALH precursor for 48 h (a) TEM bright-field low magnification, (b) TEM bright-field high magnification, and (c) TEM dark-field. 46
- Figure 3.11. Shape analysis of as-synthesized nanocrystalline TiO₂ powder obtained by thermal hydrolysis of aqueous solutions of the TALH precursor for 48 h (a) TEM bright-field micrograph, (b, c) high-resolution TEM micrographs, (d) Fourier transform of c, and (e) sketch of the shape. 47
- Figure 3.12. (A) Diffuse reflectance spectra of as-synthesized nanocrystalline TiO₂ powders obtained by thermal hydrolysis of aqueous solutions of the TALH precursor at 200 °C for (a) 24 h, (b) 48 h, (c) 72 h, and (d) 96 h. (B) Plot of the modified Kubelka-Munk function versus the energy of light absorbed. 48
- Figure 3.13. XRD patterns of as-synthesized nanocrystalline TiO₂ powders obtained by thermal hydrolysis of aqueous solutions of the TALH precursor at 160 °C for 24 h in the presence of different concentrations of urea, (a) 0.1 M, (b) 0.5 M, (c) 1.0 M, (d) 1.5 M, (e) 2.0 M (f) 3.0 M, (g) 4.0 M, and (h) 6.0 M. Labels B, R, and A indicate Bragg positions for brookite, rutile, and anatase, respectively. 49
- Figure 3.14. Raman spectra of as-synthesized nanocrystalline TiO₂ powders obtained by thermal hydrolysis of aqueous solutions of the TALH precursor at 160 °C for 24 h in the presence of different concentrations of urea, (a) 0.1 M, (b) 1.5 M, and (c) 6.0 M. 50
- Figure 3.15. FE-SEM micrographs of as-synthesized nanocrystalline TiO₂ powders obtained by thermal hydrolysis of aqueous solutions of the TALH precursor at 160 °C for 24 h in the presence of different concentrations of urea, (a) 0.1 M, (b) 1.0 M, (c) 2.0 M, and (d) 6.0 M. 52
- Figure 3.16. High-resolution transmission electron micrograph of as-synthesized nanocrystalline TiO₂ powder obtained by thermal hydrolysis of aqueous solutions of the TALH precursor at 160 °C for 24 h in the presence of 1.0 M urea. The rod-like particle of ca. 25 nm in diameter is brookite imaged along the $[-12-1]_B$ zone axis (see inset). The smaller particle of ca. 15 nm in size is anatase imaged along $[1-11]_A$. The labels A and B refer to anatase and brookite, respectively. 52

- Figure 3.17. Time course of the photocatalytic H₂ evolution over different 0.5 wt% Pt-loaded TiO₂ nanomaterials (■) TiO₂ P25, (●) TiO₂ P25HT, and (▲) TiO₂ UV100 and over bare TiO₂ nanomaterials without Pt loadings (Δ) TiO₂ UV100 (shown as example). Conditions: 0.5 g l⁻¹ photocatalysts, 0.5 wt% Pt, 75 ml Ar-saturated aqueous methanol solution (0.03 M, 2.25 mmol methanol), UV(A)-Vis illumination (60 mW cm⁻²), temperature (25 °C), natural pH (pH ≈ 6.5). 53
- Figure 3.18. Effect of methanol concentration on the amount of H₂ evolved following 15 min of UV(A)-Vis illumination over Pt-loaded TiO₂ UV100. Conditions: 0.5 g l⁻¹ photocatalysts, 0.5 wt% Pt (photochemical deposition), 75 ml Ar-saturated aqueous methanol solutions, UV(A)-Vis illumination (60 mW cm⁻²), temperature (25 °C), natural pH (pH ≈ 6.5). 54
- Figure 3.19. Time course of the photocatalytic H₂ evolution over different 0.5 wt% Pt-loaded TiO₂ nanomaterials (■) TiO₂ P25, (●) TiO₂ P25HT, and (▲) TiO₂ UV100. Conditions: 0.5 g l⁻¹ photocatalysts, 0.5 wt% Pt, 75 ml Ar-saturated aqueous methanol solution (4.93 M, 370 mmol methanol), UG1 black filter, UV(A) illumination (44.87 μeinsteins min⁻¹), temperature (25 °C), natural pH (pH ≈ 6.5). 55
- Figure 3.20. Transmittance spectrum of UG1 black filter. 55
- Figure 3.21. Effect of the light intensity on (a) the rate and on (b) the photonic efficiency of the photocatalytic H₂ evolution over different 0.5 wt% Pt-loaded TiO₂ nanomaterials (■) TiO₂ P25, (●) TiO₂ P25HT, and (▲) TiO₂ UV100. Conditions: 0.5 g l⁻¹ photocatalysts, 0.5 wt% Pt, 75 ml Ar-saturated aqueous methanol solution (370 mmol methanol), UG1 black filter, UV(A) illumination (up to ≈ 45 μeinsteins min⁻¹), temperature (25 °C), natural pH (pH ≈ 6.5). 57
- Figure 3.22. (a) Time course of the photocatalytic H₂ evolution as a function of the amount of polypyrrole loaded on TiO₂ P25 surface. (■) 0.0 (photodeposition method), (●) 0.5, (▶) 1.0, (◆) 2.0, (□) 3.0, (○) 5.0 wt% polypyrrole. (b) Effect of polypyrrole loading on the amount of H₂ evolved following 5 h of illumination. Conditions: 0.5 g l⁻¹ photocatalysts, 0.5 and 1.0 wt% Pt and polypyrrole, respectively, 75 ml Ar-saturated aqueous methanol solution (0.03 M, 2.25 mmol methanol), UV(A)-Vis illumination (60 mW cm⁻²), temperature (25 °C), natural pH (pH ≈ 6.5). 59
- Figure 3.23. (a) Time course of the photocatalytic H₂ evolution as a function of the amount of Pt loaded on TiO₂ surface. (■) 0.1, (●) 0.3, (▶) 0.5, (◆) 0.75, (□) 1.0, (○) 2.0 wt% Pt. (b) Effect of Pt loading on the amount of H₂ evolved following 5 h of illumination. Conditions: 0.5 g l⁻¹ photocatalysts, 0.5 and 1.0 wt% Pt and polypyrrole, respectively, 75 ml Ar-saturated aqueous methanol solution (0.03 M, 2.25 mmol methanol), UV(A)-Vis illumination (60 mW cm⁻²), temperature (25 °C), natural pH (pH ≈ 6.5). 60
- Figure 3.24. Effect of four consecutive runs on the photocatalytic H₂ production. Conditions: 0.5 g l⁻¹ photocatalysts, 0.5 and 1.0 wt% Pt and polypyrrole, respectively, 75 ml Ar-saturated aqueous methanol solution (0.03 M, 2.25 mmol methanol), UV(A)-Vis illumination (60 mW cm⁻²), temperature (25 °C), natural pH (pH ≈ 6.5). First run without methanol addition. 60
- Figure 3.25. Effect of methanol concentration on the amount of H₂ evolved following 1 h of UV(A)-Vis illumination. Conditions: 0.5 g l⁻¹ photocatalysts, 0.5 and 1.0 wt% Pt and polypyrrole, respectively, 75 ml Ar-saturated aqueous methanol solutions, UV(A)-Vis illumination (60 mW cm⁻²), temperature (25 °C), natural pH (pH ≈ 6.5). 61

- Figure 3.26. Time course of the photocatalytic H₂ evolution over 0.5 wt% Pt-loaded TiO₂ nanomaterials (■) TiO₂ P25, (●) TiO₂ anatase nanoparticles (TiO₂A_{0.1,24}), (◆) TiO₂ anatase/brookite mixture (TiO₂AB_{1.0,24}), and (▲) TiO₂ brookite nanorods (TiO₂B_{6.0,24}) and over bare TiO₂ nanomaterials without Pt loadings (◇) TiO₂ anatase/brookite mixture (TiO₂AB_{1.0,24}, shown as example). Conditions: 0.5 g l⁻¹ photocatalysts, 0.5 wt% Pt (photochemical deposition method), 75 ml Ar-saturated aqueous methanol solution (0.03 M, 2.25 mmol methanol), UV(A)-Vis illumination (60 mW cm⁻²), temperature (25 °C), natural pH (pH ≈ 6.5)..... 62
- Figure 3.27. Time course of the photocatalytic H₂ evolution over Pt-loaded TiO₂ nanomaterials (●) TiO₂ anatase nanoparticles (TiO₂A_{0.1,24}), (◆) TiO₂ anatase/brookite mixture (TiO₂AB_{1.0,24}), and (▲) TiO₂ brookite nanorods (TiO₂B_{6.0,24}). Conditions: 0.5 g l⁻¹ photocatalysts, 0.5 wt% Pt (photochemical deposition method), 75 ml Ar-saturated aqueous methanol solution (4.93 M, 370 mmol methanol), UG1 black filter, UV(A) illumination (32.4 μeinsteins min⁻¹), temperature (25 °C), natural pH (pH ≈ 6.5)..... 64
- Figure 3.28. Time course of the photocatalytic H₂ evolution over Pt-loaded TiO₂ nanomaterials (●) TiO₂ anatase nanoparticles (TiO₂A_{0.1,24}), (◆) TiO₂ anatase/brookite mixture (TiO₂AB_{1.0,24}), (▲) TiO₂ brookite nanorods (TiO₂B_{6.0,24}), and (■) TiO₂ P25. Conditions: 0.5 g l⁻¹ photocatalysts, 0.5 wt% Pt (colloidal Pt suspensions), 75 ml Ar-saturated aqueous methanol solution (4.93 M, 370 mmol methanol), UG1 black filter, UV(A) illumination (21.66 μeinsteins min⁻¹), temperature (25 °C), natural pH (pH ≈ 6.5). 65
- Figure 3.29. Time course of photocatalytic DCA degradation using anatase nanoparticles, anatase/brookite mixtures, and brookite nanorods as photocatalysts. Conditions: 0.5 g l⁻¹ photocatalysts, 60 ml O₂-saturated aqueous solution (1 mM, 0.06 mmol DCA), a cut-off filter (WG 320) which eliminates UV-radiation below λ = 320 nm, UV(A)-Vis illumination (60 mW cm⁻²), temperature (25 °C), pH = 3.0. 67
- Figure 4.1. XRD diffraction patterns of (a) TiO₂ P25, (b) titanate structure obtained after washing with 0.1 M HCl and deionized water, respectively. Labels A and R indicate Bragg positions for anatase and rutile, respectively. Label ● indicates Bragg positions for titanate structure. 71
- Figure 4.2. XRD diffraction patterns of (a) titanate structure obtained after washing with 0.1 M HCl and deionized water, respectively and (b) titanate structure obtained after washing with 0.1 M HCl and deionized water, respectively, and then followed by treatment in 0.5 M HCl overnight. Labels A and R indicate Bragg positions for anatase and rutile, respectively. 72
- Figure 4.3. Schematic model for the preparation of anatase nanoparticles by transformation of titanate structures induced by the NaOH treatment and the post-treatment washing. 74
- Figure 4.4. XRD patterns of as-synthesized nanocrystalline TiO₂ powders obtained by thermal hydrolysis of aqueous solutions of the TALH precursor at 160 °C for 48 h employing sealed glass ampoules. Labels R and A indicate Bragg positions for rutile and anatase, respectively. 75
- Figure 4.5. Proposed steps for the formation and the anisotropic growth of TiO₂ rutile nanorods. 78

- Figure 4.6. XRD patterns of as-synthesized nanocrystalline TiO_2 powders obtained by thermal hydrolysis of aqueous solutions of the TALH precursor at 160°C for (a) 3 h, (b) 6 h, (c) 12 h, (d) 48 h, and (e) 72 h in the presence of 0.1 M of urea. Labels B, R, and A indicate Bragg positions for brookite, rutile, and anatase, respectively. 79
- Figure 4.7. XRD patterns of as-synthesized nanocrystalline TiO_2 powders obtained by thermal hydrolysis of aqueous solutions of the TALH precursor at (a) 120°C , (b) 160°C , and (c) 200°C for 24 h in the presence of 0.1 M of urea. Labels B, R, and A indicate Bragg positions for brookite, rutile, and anatase, respectively. 81
- Figure 4.8. XRD patterns of as-synthesized nanocrystalline TiO_2 powders obtained by thermal hydrolysis of aqueous solutions of the TALH precursor at 160°C for 24 h in the presence of NH_4OH (pH = 9.9). Labels B, R, and A indicate Bragg positions for brookite, rutile, and anatase, respectively. 81
- Figure 4.9. Proposed routes for the formation of anatase nanoparticles and brookite nanorods. 83
- Figure 4.10. N_2 adsorption-desorption BET isotherms of Pt-loaded TiO_2 UV100 (A), of Pt-loaded TiO_2 P25HT (B), and of Pt-loaded TiO_2 P25 (C). The insets show the pore size distribution. 85
- Figure 4.11. Schematic illustration showing the agglomerated TiO_2 nanoparticles with an interparticle charge carrier transport leading to enhanced electron/hole pair separation and with mesoporous structure facilitating the CH_3OH diffusion through the pores. 86
- Figure 4.12. DF-TEM micrograph of TiO_2 P25HT modified with 0.5 wt% Pt (photochemical deposition method). Pt is seen as bright points with diameter of about 3.0 nm. 87
- Figure 4.13. Plot of \log (photonic efficiency) vs. \log (photon flux) for the photocatalytic H_2 evolution over 0.5 wt% Pt-loaded photocatalysts (■) TiO_2 P25, (●) TiO_2 P25HT, and (▲) TiO_2 UV100. Conditions: 0.5 g l^{-1} photocatalysts, 75 ml aqueous methanol solutions (370 mmol methanol), UG1 black filter, neutral density filter, UV(A) illumination. 89
- Figure 4.14. Schematic representing the proposed steps for the photocatalytic molecular hydrogen production from aqueous methanol solution, (1) photogeneration of charge carriers, e^- and h^+ ; (2) trapping of e^- by Pt islands; (3) first oxidation step of CH_3OH either by trapped hole or by hydroxyl radical, $\cdot\text{OH}$; (4) reduction of H^+ ; (5) formation of HCHO through e^- injection into the conduction band of TiO_2 or to the Pt islands (current-doubling); (6) recombination channel. 92
- Figure 4.15. Scheme representing the enhanced charge carrier separation and the photocatalytic activity of TiO_2 modified with Pt-polypyrrole nanocomposites, (1) photogeneration of charge carriers, e^- and h^+ ; (2) trapping of e^- by Pt islands; (3) photogenerated holes channelling by polypyrrole to the polymer/solution interface; (4) first oxidation step of CH_3OH ; (5) reduction of H^+ ; (6) formation of HCHO through e^- injection into the conduction band of TiO_2 (current-doubling); (7) recombination channel. 95

- Figure 4.16. Time course of photocatalytic H₂ evolution over modified TiO₂ photocatalysts (■, □) TiO₂ P25, (●, ○) TiO₂ P25HT, and (▲, △) TiO₂ UV100. Solid symbols denote the modification with 0.5 wt% Pt via a photochemical deposition method, whereas open symbols denote the modification with Pt-polypyrrole nanocomposites (0.5 wt% Pt and 1.0 wt% polypyrrole). Conditions: 0.5 g l⁻¹ photocatalysts, 75 ml Ar-saturated aqueous methanol solution (0.03 M, 2.25 mmol methanol), UV-Vis illumination (60 mW cm⁻²). 96
- Figure 4.17. Relation between the photonic efficiency, the surface area, and the content of brookite; (●, a) photonic efficiency and (■, b) BET surface area. Conditions: 0.5 g l⁻¹ catalyst, 0.5 wt% Pt (colloidal Pt suspension), 75 ml Ar-saturated aqueous methanol solution (4.93 M, 370 mmol methanol), UG1 Black filter, UV(A) illumination (21.66 μeinstein min⁻¹). 99
- Figure 4.18. Mott-Schottky plots obtained at different frequencies for the TiO₂ film electrodes prepared with (a) anatase nanoparticles and (b) brookite nanorods 101
- Figure 4.19. Photovoltage vs. suspension pH values measured for (a) anatase nanoparticles and (b) brookite nanorods in 0.1 M KNO₃ in the presence of MV²⁺ 102
- Figure 4.20. Plot of the modified Kubelka-Munk function versus the energy of light absorbed for (a) anatase nanoparticles and (b) brookite nanorods. 104
- Figure 4.21. Electrochemical potentials (vs. NHE) of band edges of anatase and brookite phases and expected charge carrier transfer events. The recombination channels are not shown. 105
- Figure 4.22. Relation between the photonic efficiency, the BET surface area, and the content of brookite; (●, a) photonic efficiency and (■, b) surface area. Conditions: 0.5 g l⁻¹ catalyst, 60 ml aqueous DCA solution (1.0 mM), pH 3 110
- Figure 4.23. Photonic efficiencies of gaseous acetaldehyde decomposition for rutile nanorods embedded in anatase nanoparticles (RA24), rutile nanorods decorated with anatase nanoparticles (RA48), pure rutile nanorods (R72 and R96), TiO₂ P25 (P25), and for commercial rutile nanoparticles (R25 and R34). Conditions: 3.33 mg cm⁻² photocatalysts, TiO₂ films (30 cm²), initial acetaldehyde concentration (1.0 ppm), 50 % relative humidity, gas flow (1006 ml min⁻¹), UV(A) illumination (1.0 mW cm⁻²), ambient temperature (25 °C). 112
- Figure 4.24. Relation between the photonic efficiency of gaseous acetaldehyde decomposition, the BET surface area, and the content of brookite; (●, a) photonic efficiency and (■, b) BET surface area. Conditions: 0.08 g cm⁻² photocatalysts, TiO₂ pellets (6.25 cm²), initial acetaldehyde concentration (1.0 ppm), 50 % relative humidity, gas flow (1006 ml min⁻¹), UV(A) illumination (1.0 mW cm⁻²), ambient temperature (25 °C). 114
- Figure 4.25. Photonic efficiencies of gaseous acetaldehyde decomposition for anatase nanoparticles (A_{0.1,24}), anatase/brookite mixtures (AB_{1.0,24}, AB_{1.5,24}, and AB_{2.0,24}), brookite nanorods (B_{6.0,24}), TiO₂ P25 (P25), TiO₂ UV100 (UV100), and for TiO₂ P25HT (P25HT). Conditions: 0.08 g cm⁻² photocatalysts, TiO₂ pellets (6.25 cm²), initial acetaldehyde concentration (1.0 ppm), 50 % relative humidity, gas flow (1006 ml min⁻¹), UV(A) illumination (1.0 mW cm⁻²), ambient temperature (25 °C) 115

7.4. Publications

1- Tarek A. Kandiel, Ralf Dillert, and Detlef W. Bahnemann "Enhanced photocatalytic production of molecular hydrogen on TiO₂ modified with Pt-polypyrrole nanocomposites" *Photochemical & Photobiological Sciences*, **2009**, 8, 683-690.

2- Tarek A. Kandiel, Armin Feldhoff, Lars Robben, Ralf Dillert, and Detlef W. Bahnemann "Tailored titanium dioxide nanomaterials: anatase nanoparticles and brookite nanorods as highly active photocatalysts" *Chemistry of Materials*, **2010**, 22, 2050-2060.

3- Tarek A. Kandiel, Ralf Dillert, Armin Feldhoff, and Detlef W. Bahnemann "Direct synthesis of photocatalytically active rutile TiO₂ nanorods partly decorated with anatase nanoparticles" *The Journal of Physical Chemistry C*, **2010**, 114, 4909-4915.

4- Adel A. Ismail, Tarek A. Kandiel, and Detlef W. Bahnemann "Novel (and better?) titania-based photocatalysts: brookite nanorods and mesoporous structures" *Journal of Photochemistry and Photobiology A: Chemistry*, **2010**, in press.

5- Tarek A. Kandiel, Ralf Dillert, Lars Robben, and Detlef W. Bahnemann "Photonic efficiencies and mechanism of photocatalytic molecular hydrogen production over platinized titanium dioxide from aqueous methanol solutions" *Catalysis Today*, **2010**, submitted.

7.5. Presentations

7.5.1. Oral presentations

1- Tarek A. Kandiel, Ralf Dillert, and Detlef W. Bahnemann "Photonic efficiencies and mechanism of photocatalytic molecular hydrogen production over platinized titanium dioxide from aqueous methanol solutions" *XXIV International Conference on Photochemistry (ICP2009)*, 19-24 July **2009**, Toledo, Spain.

2- Tarek A. Kandiel, Ralf Dillert, and Detlef W. Bahnemann "Photocatalytic hydrogen production over platinized biphasial nanocrystalline anatase/brookite titanium dioxide" *SolarPACES 2009*, 15-18 September **2009**, Berlin, Germany.

3- Tarek A. Kandiel, Ralf Dillert, and Detlef W. Bahnemann "Tailored titanium dioxide nanomaterials: anatase nanoparticles and brookite nanorods as highly active photocatalysts" *239th ACS National Meeting & Exposition*, 21-25 March **2010**, San Francisco, California, USA.

4- Adel A. Ismail, Tarek A. Kandiel, and Detlef W. Bahnemann "Novel (and better?) titania-based photocatalysts: brookite nanorods and mesoporous structures" *Third International Conference on Semiconductor Photochemistry (SP3)*, 12-14 April **2010**, Glasgow, UK.

7.5.2. Poster presentations

- 1- Tarek A. Kandiel, Ralf Dillert, and Detlef W. Bahnemann "One-step hydrothermal synthesis of rutile titanium dioxide nanorods" *NanoDay 2007*, Laboratorium für Nano- und Quantenengineering (LNQE), Leibniz Universität Hannover, Hauptgebäude (1101), Donnerstag 27.09.2007, Hannover, Germany.
- 2- Tarek A. Kandiel, Ralf Dillert, and Detlef W. Bahnemann "Enhanced photocatalytic production of molecular hydrogen on TiO₂ modified with Pt-polypyrrole nanocomposites" *NanoDay 2008*, Laboratorium für Nano- und Quantenengineering (LNQE), Leibniz Universität Hannover, Hauptgebäude (1101), Donnerstag 25.09.2008, Hannover, Germany.
- 3- Tarek A. Kandiel, Ralf Dillert, and Detlef W. Bahnemann "Enhanced photocatalytic production of molecular hydrogen on TiO₂ modified with Pt-polypyrrole nanocomposites" *5th European Meeting on Solar Chemistry and Photocatalysis: Environmental Applications (SPEA5)*, 4-8 October 2008, Palermo, Italy.
- 4- Tarek A. Kandiel, Ralf Dillert, Armin Feldhoff, and Detlef W. Bahnemann "One-step hydrothermal synthesis of rutile titanium dioxide nanorods" *Photocatalytic Products and Technologies Conference-PPTC'09*, 11-13 May 2009, University of Minho, Guimaraes, Portugal.
- 5- Tarek A. Kandiel, Armin Feldhoff, Lars Robben, Ralf Dillert, and Detlef W. Bahnemann "Tailored titanium dioxide nanomaterials: anatase nanoparticles and brookite nanorods" *NanoDay 2009*, Laboratorium für Nano- und Quantenengineering (LNQE), Leibniz Universität Hannover, Hauptgebäude (1101), Mittwoch 30.09.2009, Hannover, Germany.
- 6- Tarek A. Kandiel, Ralf Dillert, and Detlef W. Bahnemann "Tailored titanium dioxide materials: Brookite nanorods and anatase nanoparticles" *The 14th International Conference on TiO₂ Photocatalysis: Fundamentals and Applications (TiO₂-14)*, 5-8 October 2009, Niagara Falls, New York, USA.
- 7- Tarek A. Kandiel, Ralf Dillert, and Detlef W. Bahnemann "Photonic efficiencies and mechanism of photocatalytic molecular hydrogen production over platinized titanium dioxide from aqueous methanol solutions" *6th European Meeting on Solar Chemistry and Photocatalysis: Environmental Applications (SPEA6)*, 13-16 June 2010, Prague, Czech Republic.

7.6. Curriculum vitae

Personal data:

Name	Tarek Abdel-Samad Abdel-Rahman Kandiel
Date of Birth	10.09.1978
Gender	Male
Nationality	Egyptian
Marital Status	Married

Academic qualifications:

1999: Bachelor of Science in Chemistry, Chemistry Department, Faculty of Science (Sohag), South Valley University (Sohag Branch).

2001: Preliminary of Master of Science in Chemistry (Inorganic and Analytical Chemistry), Chemistry Department, Faculty of Science (Sohag), South Valley University (Sohag Branch).

2005: Master of Science in Chemistry, Chemistry Department, Faculty of Science (Sohag), South Valley University (Sohag Branch).

Work experience:

21.03.2000–03.12.2006: Teaching Assistant and Assistant Lecturer at the Chemistry Department, Faculty of Science (Sohag), South Valley University (Sohag Branch), Egypt.

04.12.2006–20.07.2010: PhD work at Institute of Technical Chemistry (Photocatalysis and Nanotechnology Group), Gottfried Wilhelm Leibniz University Hannover under the supervision of Prof. Dr. Detlef W. Bahnemann.